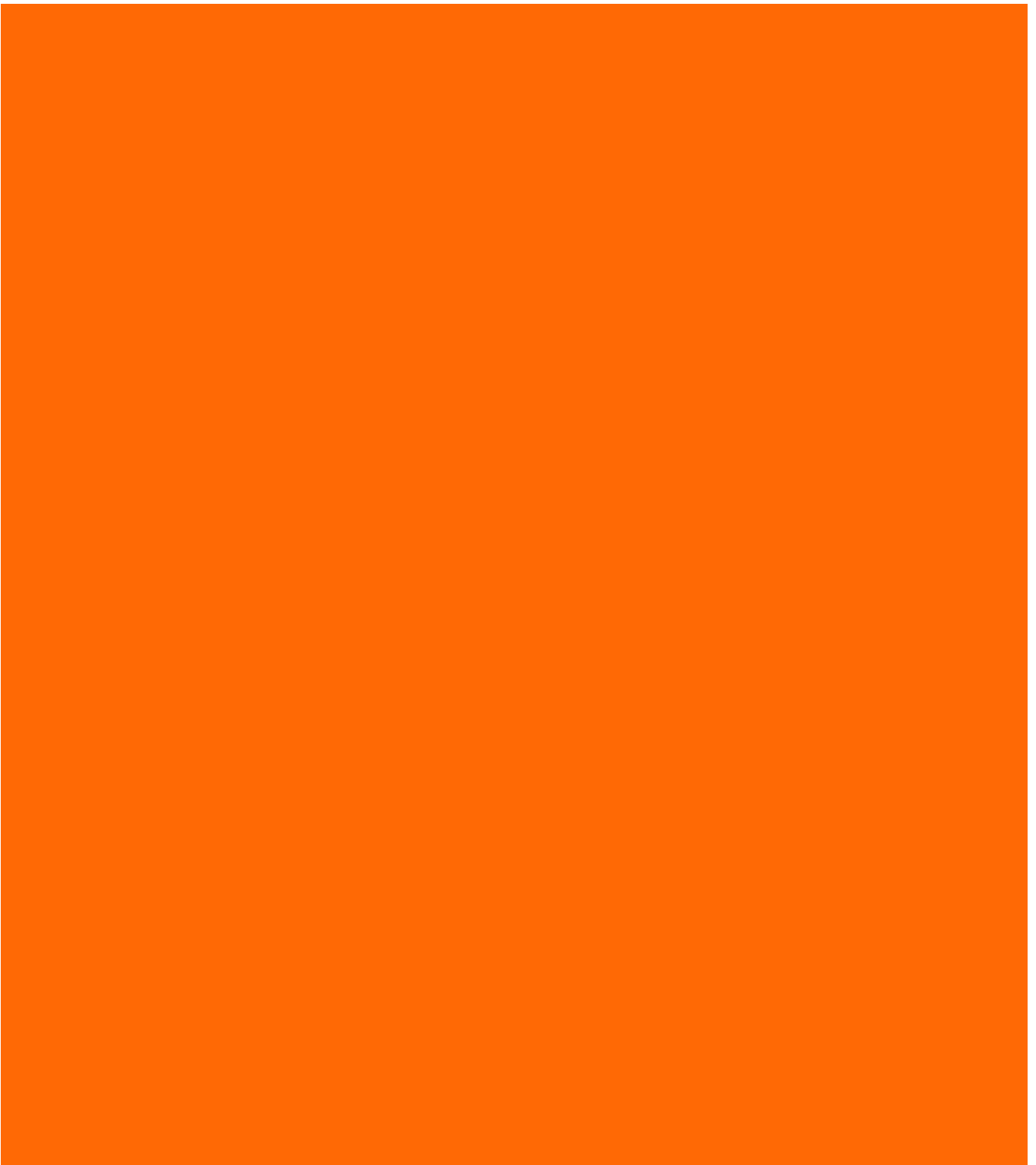WorldAutoSteel

AHSS IMPLEMENTATION SOLUTIONS:

LIQUID METAL EMBRITTLEMENT COMPONENT STUDY

October 2024

AHSS Implementation Solutions:

LME Component Study

Phase 2

October 2024

Prof. Dr.-Ing. Gerson Meschut

Keke Yang, M.Sc.
Laboratory for Material and Joining
Technology
University of Paderborn
Germany

Prof. Dr.-Ing. Michael Rethmeier

Dr.-Ing. Max Biegler
Fraunhofer IPK
Berlin
Germany

This Liquid Metal Embrittlement Component Study was commissioned by WorldAutoSteel, the automotive group of the World Steel Association, with its 18 member companies providing the required materials to conduct the study and a core team of member subject matter experts to provide feedback to the research. The reports following are supplied by the contractors who conducted the study, as follows:

LME Study commissioned by:

WorldAutoSteel

And conducted by:

Fraunhofer
IPK

IWF

Contents

1   Executive Summary

During resistance spot welding (RSW) of zinc-coated advanced high strength steels (AHSS), it is possible to observe liquid metal embrittlement (LME). Since LME is often associated with a reduction of mechanical properties, it is critical to gain a broader understanding of the phenomenon and its possible impacts. The goal of this study is to understand the influence of process and welding set-up related parameters behind LME, acquire the knowledge to prevent and be able to judge possible consequences of residual LME.

This is the second phase of a study on LME conducted by WorldAutoSteel, a global research consortium driving the future of sustainable mobility through steel innovation. While first study investigated LME occurrence, mitigation and impact mostly on academic single-spot specimen. The second study investigates LME on an industrial scale, i.e. a deep drawn component with multiple spot welds as well as manufacturing-related imperfections. The objective of the study is to demonstrate that LME mitigation measures developed on academic samples are applicable to industrial geometries and to answer the question whether there are any additional characteristic features regarding LME on a part-scale.

Researchers conducted investigations for crack susceptibility experimentally using a so-called S-Rail geometry and completed simulations in conjunction with the experimental investigations in order to offer deeper analyses for crack formation and for mitigation measures.

Researchers observed an overall greatly reduced LME susceptibility in the steels in 2023 in comparison to the first phase in 2017. Using extreme welding conditions, especially longer-than-normal weld-times, LME could still be forced in some material stack-ups. These stack-ups were then investigated on a part-scale. It could be shown that springback on a part-scale generally exacerbates LME formation but at the same time no location-dependent LME formation could be observed. This leads to the conclusion that it is possible but not necessary to test for LME on a component-scale

level. Furthermore, process-imperfections such as electrode tilt would also cause increased LME. This shows that it is possible to reduce LME formation by using precise component and weld gun alignments.

Even for the worst cracks caused by extreme parametrization, LME could be completely avoided using mitigation measures. By increasing electrode hold time after the weld and using larger electrode caps reduced the formation of LME significantly, in most cases even outright avoiding any crack formation.

The accompanying simulation investigations demonstrated that crack formation can be predicted by analyzing the surface temperature history as well as the material stresses. Researchers developed and tested a criterion that allows comparisons of welding parameters and different stack-ups with the same AHSS. With this criterion, potential at-risk resistance spot welds can already be optimized during the planning phase of a new automotive car body, giving another tool to reduce and even altogether avoid LME formation.

Finally, researchers conducted crash tests of the component-scale S-Rail to evaluate the impact of residual LME cracks on crash performance. It was found that the new generation of third-generation high-strength steels exhibits generally low sensitivity to LME. Even under conditions that promote LME cracks, they mainly manifest as light cracks, primarily A-type and B-type, with very rare C-type cracks. This level of crack severity does not affect the load-bearing capacity of the joints under crash loading.

2   Summary of LME Component Study Findings

Following is a summary of the findings from this study. All statements are given based on the investigated boundary conditions, which include the use of extreme welding parameters (e.g. use of excessive weld times), being necessary in order to enforce significant amounts of LME.

- ✓ New generation AHSS have greatly reduced crack sensitivity.

- ✓ The creation of cracks is not possible even under extreme welding conditions for most material thickness combinations.

- ✓ Springback and electrode misalignment increase crack risk.

- ✓ The study found no systematic influence of local geometric features (i.e. local stiffness) on LME.

- ✓ LME tests can be completed on academic samples and the results are valid in a production environment

- ✓ Mitigation measures of elongated hold times and larger electrode working planes are also applicable on component-scale welds.

- ✓ LME can be controlled in a large process window.

- ✓ Simulation tools are available to determine safe process windows using LME occurrence criteria.

- ✓ Third-generation high-strength steels show generally low sensitivity to LME, with only light crack severity observed. This level of severity does not affect the load-bearing capacity of the joints in crash tests.

3   Introduction

A fundamental objective of vehicle manufacturers is to lower vehicle fuel consumption and emissions while simultaneously enhancing passive safety for occupants. One effective approach to meet these goals is incorporating advanced high-strength steel (AHSS) grades into vehicle structures. These innovative steels are preferred over other materials due to their excellent balance of strength and ductility.

To safeguard these steels against corrosion, it is common to apply a zinc coating. Resistance spot welding (RSW) is the most prevalent method for joining steels in automotive body construction due to its cost-effectiveness and high process reliability. However, during the RSW of AHSS grades, the detection of surface cracks can appear within the weld zone. These cracks can develop from molten zinc, infiltrating the steel's grain boundaries, which can cause a brittle fracture. This issue is commonly known as Liquid Metal Embrittlement (LME).

Lab specimen   **Scaling up**   **S-rail component**
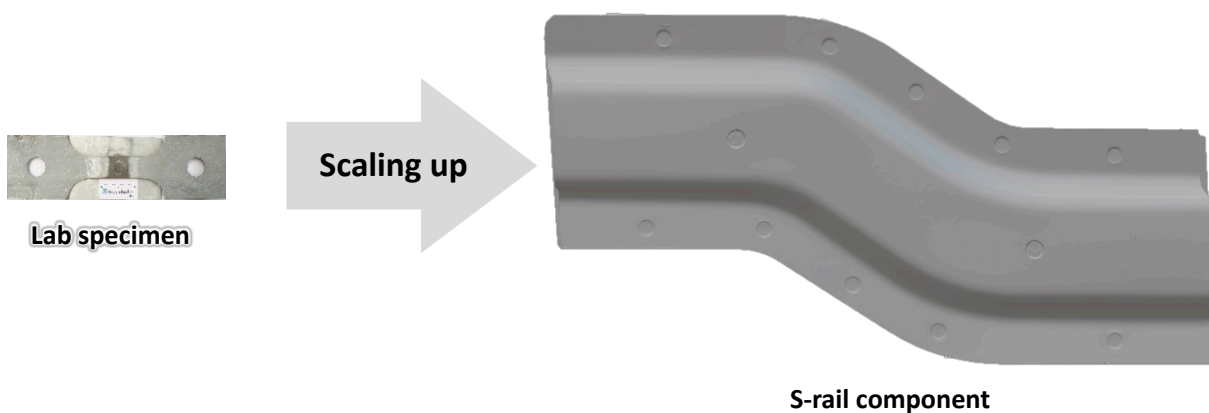
Figure 3-1:   Investigation of the Effects of Scaling Up from Laboratory Specimens to Industrial Components

Adding to a previous study that explored the mechanisms of LME cracking, crack avoidance and crack influence on mechanical properties of a joint, this study investigates the LME phenomenon on a part-scale. Initiated by the question whether developed LME mitigation measures are useable in industrial practice, researchers selected a deep-drawn component with multiple resistance spot welds for this work.

This component has springback and tolerances from the production process and is directly comparable to stamped components used commonly in automotive car body construction. The main questions for the project are whether there is an influence of the part geometry and local manufacturing tolerances on LME formation and whether the previously developed measures for LME avoidance are effective on a part scale. Lastly, the evaluation of the mechanical performance of the component under crash loading was necessary in order to assess a possible influence of LME on mechanical performance of a resistance spot-welded assembly.

It should be noted that in order to reliably cause LME cracking, unrealistically energy-intensive resistance spot welding parameters were used throughout the project. Under standard industrial process conditions, no cracks with significant size could be produced for all investigated material thickness combinations.

4 Experimental Setup and Boundary Conditions

4.1 Testing Materials, Material Properties and Stack-ups

Within the research framework, we investigated eight different steel types. These steels were anonymously provided and characterized by WorldAutoSteel. (WAS). Each type of steel will be identified by its primary WAS-ID (e.g., the 1.5mm thick RA980 is designated as ID 1661). Representative steel types that could be sensitive to LME were selected, hence not all available steel types or coatings were included. Among these steels, six are AHSS, and the remaining two are conventional steels used to create different stack-ups. Table 4-1 provides an overview of all material thickness combinations (MTC) used in this project.

Table 4-1: Material thickness combinations (Overview)

MTC#	Grade	ID	Coating	Thickness in mm
1	RA980	1661	GI	1.5
	MS270	1657	HDG	2.0
2	RA1180	1655	EG	1.4
	RA1180	1655	EG	1.4
3	DP790	1653	GA	1.6
	RA980	1659	GA	1.2
4	RA980	1659	GA	1.2
	RA980	1659	GA	1.2
	MS270	1656	GI	1.0
5	RA1180	1660	GI	1.2
	DP1180	1658	GI	1.4
	MS270	1656	HDG	1.0

4.2 Specimen Geometries

4.2.1 Laboratory Flat Specimen

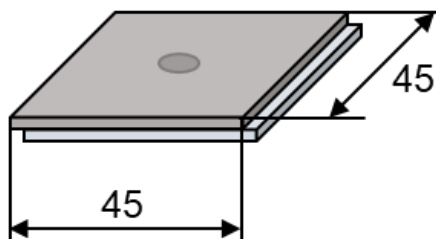For the determination of weldability 45 x 45 mm² specimen were welded as specified in SEP1220-2 (see Figure 4-1).

Figure 4-1:   Geometry of the laboratory flat specimen

4.2.2 LWF-KSII Specimen

To determine the effective load for the S-Rail component crash tests, LWF-KSII samples with an inner width (IW) of 34 mm according to [15] were used. The LWF-KSII samples consist of two symmetrical U-shaped profiles connected at the base. This sample geometry, shown in Figure 4-2, has the advantage of increased stiffness, allowing higher loads to be concentrated on the actual joint rather than on the surrounding sheet metal.
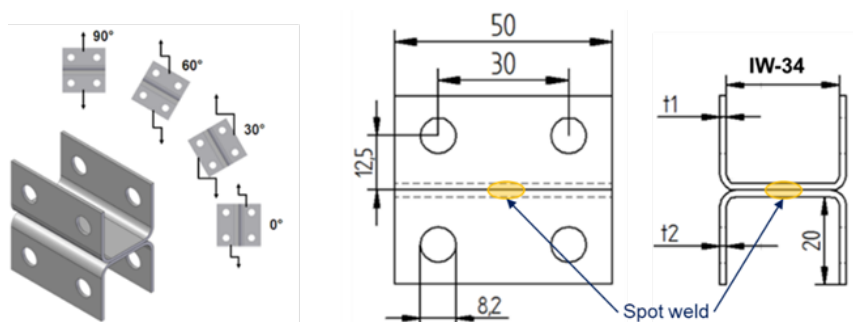

Figure 4-2:   Load bearings (left) and (right) geometry of the used LWF-KSII specimen

This is especially important when studying cross-tensile loads, which typically cause greater material deformation than planar isotropic samples. Another major advantage of the LWF-KSII samples (also illustrated in this figure) is the ability to switch between

shear-tensile testing (0° load angle) and cross-tensile testing (90° load angle) using the same sample geometry.

4.2.3   S-Rail Component

In this project, sample sizes approximating real component levels are used, specifically S-Rail components. The S-Rail forming process is completed in a single-stage deep drawing process with a defined drawing depth. As a result, a flange remains on the part after forming, and trimmed using laser cutting. The setup for the deep drawing process, carried out at the LFT of the FAU in Erlangen, is shown in Figure 4-3.
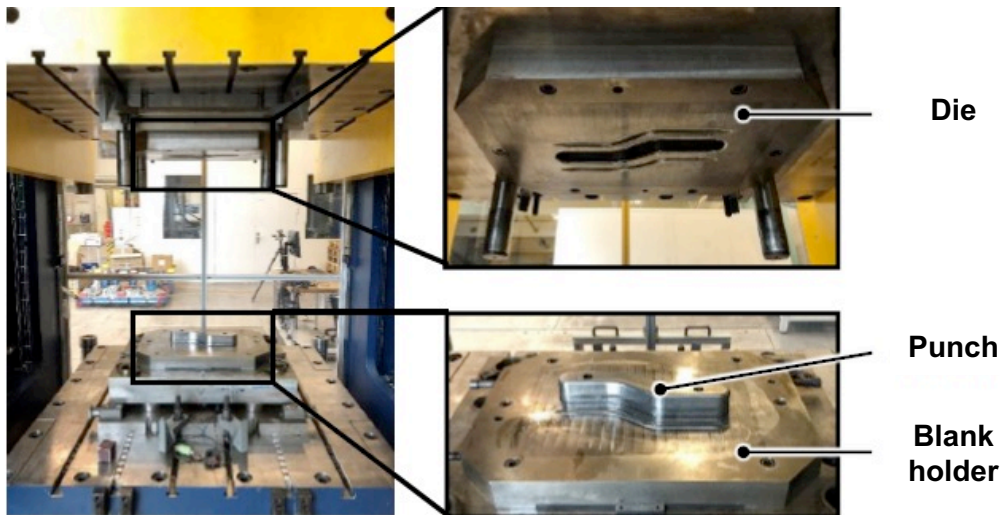

Figure 4-3:   Tool (with draw beads) and setup for deep drawing of the S-Rail component from LFT

The tool consists of a punch, a blank holder, and a die. The blank holder and die are available in two versions: with and without draw beads. Located in the blank holder, draw beads are set on spacer plates that define the height of the draw beads. This tool is installed on a Lasco TZP 400 hydraulic deep drawing press, capable of applying a maximum punch force of 4,000 kN and a maximum blank holder force of 1,600 kN. The deep drawing punch is fixed to a base plate mounted on the workbench, and the die is fixed to the punch. The dimensions of the S-Rail components are shown in Figure 4-4.
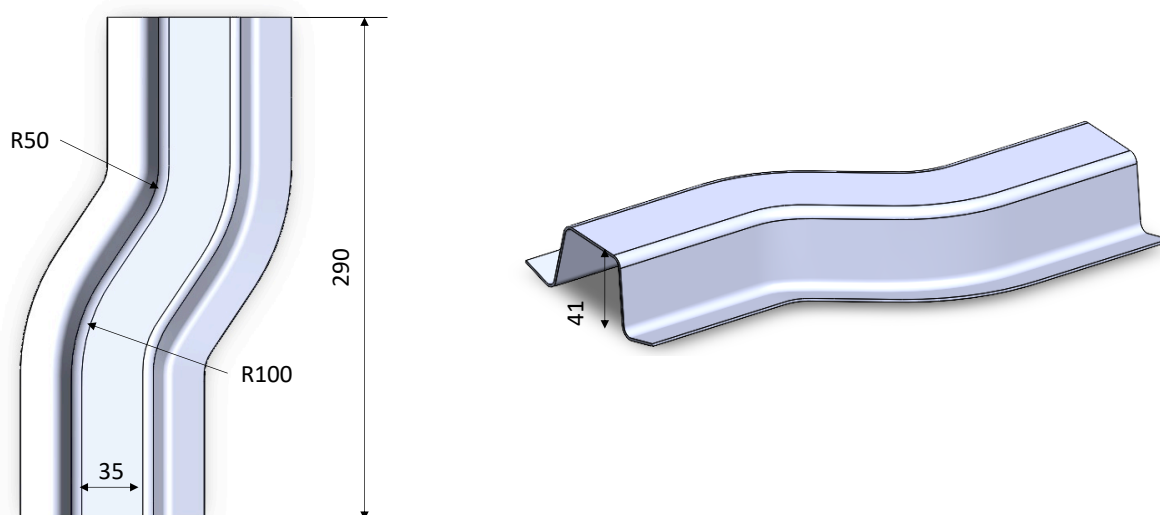
Figure 4-4:   S-Rail component geometry (standard component with laser trimming)

4.3   Resistance Spot Welding Equipment

4.3.1   Resistance Spot Welding Machine

A resistance spot welding machine from Harms & Wende GmbH & Co. KG produced the welded joints, equipped with an electromotively guided C welding gun with a maximum electrode force of 8 kN from Nimak GmbH. The current source provides a constant current controlled medium frequency direct current with 1000 Hz and a maximum current strength of 50 kA. The measured variables force, current and voltage can be documented both internally via the system and externally. Figure 4-5 shows the welding system with the most important technical data. A SK71LA/4 tip dressing machine from SVS Schweißtechnik GmbH is used to tip-dress the electrode caps.

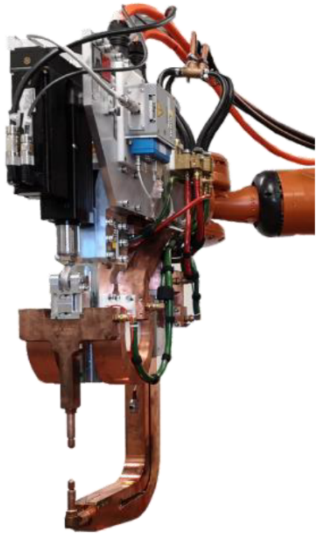| Technical Data:	
Manufacturer:	NIMAK GmbH
Type	powerGUN 2-C
Welding Current Control	
Manufacturer:	Harms & Wende Welding Control
Operating Mode:	Constant Current Regulation
Transformer	2 x 180 kVA

Figure 4-5: Resistance spot welding equipment and its most important technical features.

4.3.2 Spot Welding Electrode Geometries

Researchers utilized different electrode cap types during the investigations. Figure 4-6 shows schematics of the relevant electrode geometries. As a general basis for all of the investigations the electrode caps F1-16-20-50-5.5 (F1-5.5) were used. During the research on process optimization for the avoidance of LME, the additional electrode geometries F1-16-20-50-8.0 (F1-8.0) and A0-16-20-100 (A0-100) were investigated on their impact on the welding process and on crack formation. These electrode geometries were chosen, because their outer dimensions are identical to the F1-5.5 electrode geometry. As a consequence, they do not influence the accessibility when welding typical automotive flanges and can directly replace the F1-5.5 electrode geometry. By using appropriate tip dressing equipment F1-5.5 electrode caps were also successfully tip dressed to F1-8.0 tip shape, during the experiments of this project.
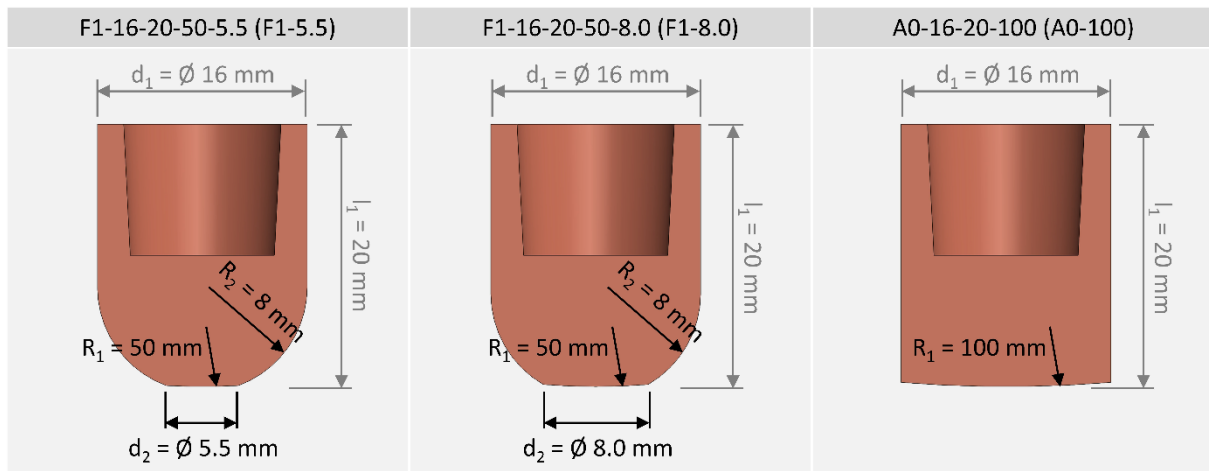
F1-16-20-50-5.5 (F1-5.5)	F1-16-20-50-8.0 (F1-8.0)	A0-16-20-100 (A0-100)
$d_1 = \varnothing$ 16 mm	$d_1 = \varnothing$ 16 mm	$d_1 = \varnothing$ 16 mm
$l_1 = 20$ mm	$l_1 = 20$ mm	$l_1 = 20$ mm
$R_2 = 8$ mm	$R_2 = 8$ mm	
$R_1 = 50$ mm	$R_1 = 50$ mm	$R_1 = 100$ mm
$d_2 = \varnothing$ 5.5 mm	$d_2 = \varnothing$ 8.0 mm	

Figure 4-6: Dimensions of investigated resistance spot welding electrodes.

4.4 Clamping Device and Experimental Setup

The demonstration parts (comprising the S-Rail and opposing components) were manufactured at LWF using a clamping system developed for the S-Rail components (Figure 3-16 a)). This clamping system features a base plate with two pre-set positioning pins for repeatable positioning of the S-Rail components. Additionally, four conventional manual clamps are arranged at the four corners of the S-Rail on the base plate. The arrangement of the clamps provides sufficient space (approximately 30 - 60 mm) between the clamping elements for joining points or tools. In total, ten joining points are arranged on the flange. Subsequently, this clamping device is fixed to a KUKA robotic arm for welding, as shown in Figure 4-7. Hence, the weld gun is kept stationary and the sample is moved on the robotic arm for multi-spot welding.
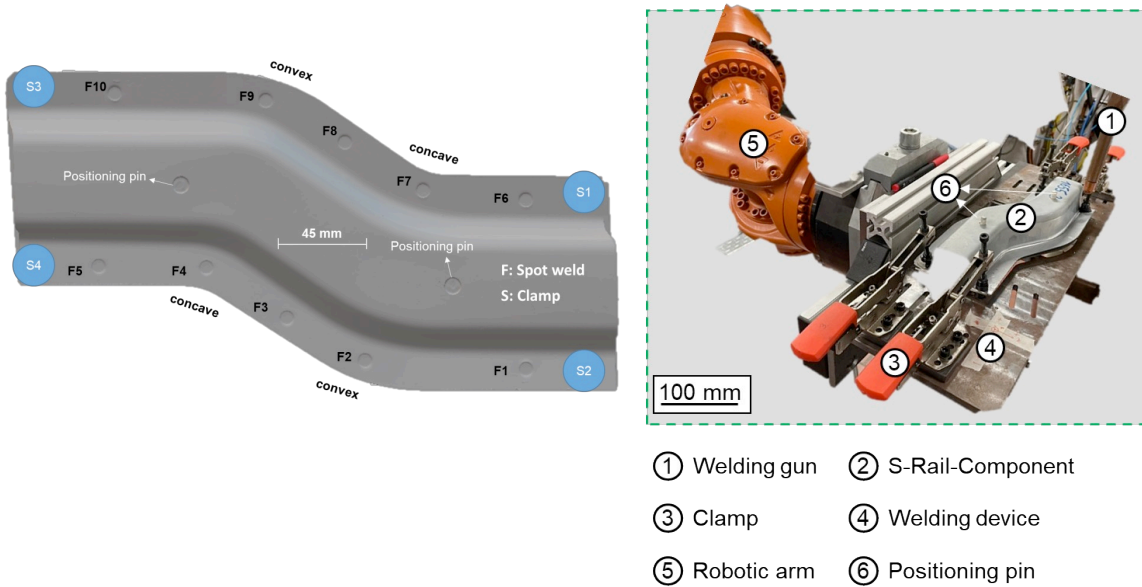
① Welding gun ② S-Rail-Component

③ Clamp ④ Welding device

⑤ Robotic arm ⑥ Positioning pin

Figure 4-7:   Experimental fixture for positioning the S-Rail component

4.5   Characterization of LME Cracks

Based on the experience from Phase 1 of the LME project, researchers used a 20% hydrochloric acid solution to remove the zinc coating after welding. Visual inspection of the sheet metal took place using an optical microscope, and results documented with photographs. To allow for a determination of local crack depth additional metallographic examinations were carried out. Figure 4-8 shows an exemplary macroscopic image of a crack afflicted spot weld next to the correlating cross-section. Consistent with phase 1, cracks with a depth of less than 100μm were not considered LME cracks.
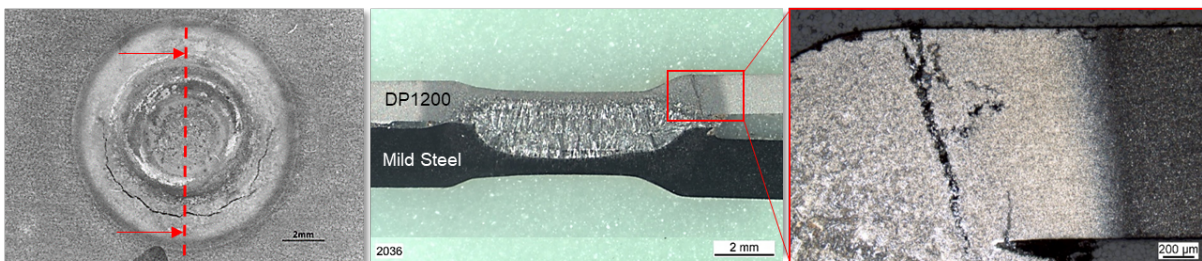

Figure 4-8:   Exemplary results of visual inspection and metallographic cross-sections: Left: Macroscopic surface view of cracked spot weld; Middle: Metallographic cross-section of same spot weld in lower magnification; right: Detail from same metallographic cross-section in higher resolution and magnification

Additionally, to evaluate the severity of LME cracks, researchers adopted the grading system from Phase 1 of the LME project. The grades are Light, Medium, and Intensive. Refer to Figure 4-9 for the corresponding legend.
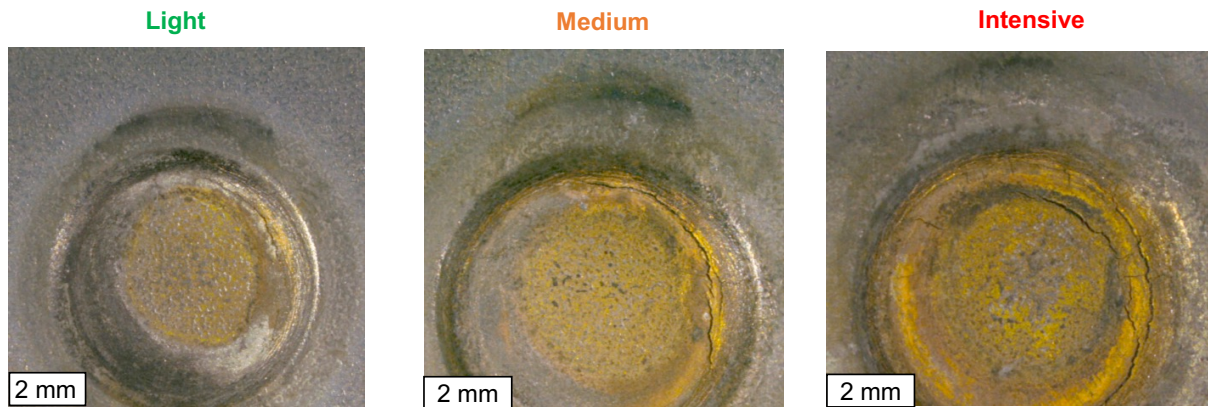

Figure 4-9:   Determining the severity of LME cracks

5   Simulation Model S

5.1   Academic Sample Simulation Model

The following requirements were imposed on a resistance spot welding simulation model for liquid metal embrittlement investigations:

- Fully coupled calculation of electrical current flow, heat generation, temperature flow, mechanical forces and stress development

- Adjustable boundaries for electrical contact and thermal cooling

- Modelling of phase transformations, considerations of associated material properties and volume changes

- 3-dimensionality to model crack influence on part-scale

The commercial finite element tool 'Simufact Welding' was chosen, and all calculations conducted in this software using a 3d electro-thermomechanical finite element model. The cross-section of a simple model for welding of a single spot on a 50 x 50 mm² sheet is shown in Figure 5-1. The model is described in detail in a previous publication [1].
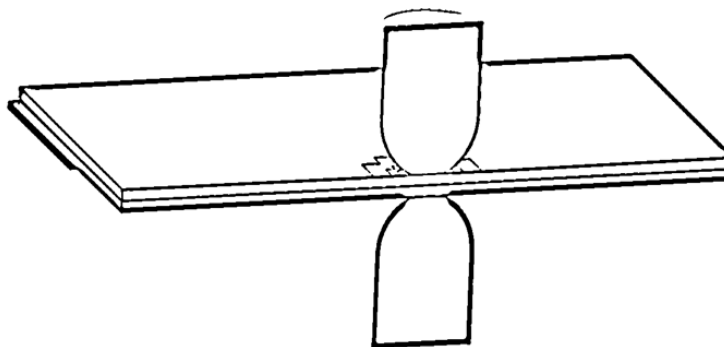
Figure 5-1:   Cross-section of the 3-dimensional model comprising two sheets, two electrodes and the clamping at the rear

5.2   Material Modelling

The AHSS material data used in the project was taken from a published data set for a DP1200HD by Prabitz et al [2]. Within the welding simulation software, the temperature-dependent thermo-mechanical and thermo-physical material properties are used to model the material behavior. The modeling of plastic deformation is utilizing an elasto-plastic approach with measured temperature-dependent flow-curves. Thermal softening for the flow- and yield-stress is plotted in Figure 5-2, showing the reduction in material strength with rising temperatures.

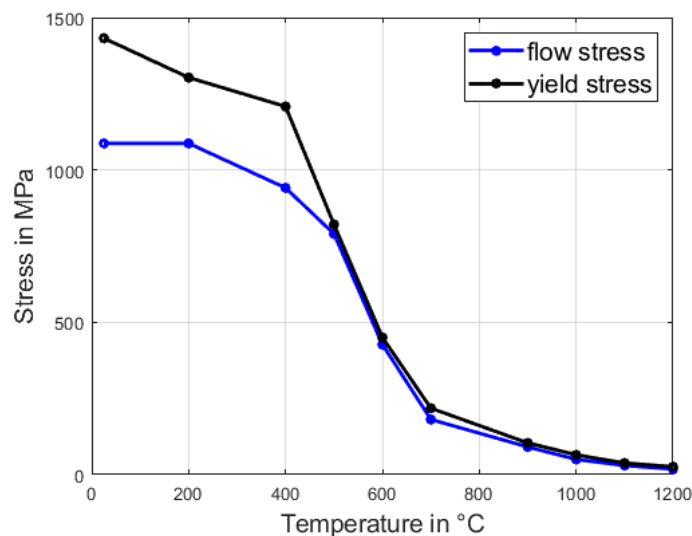Figure 5-2:   Thermal softening behavior of the CP1200 as published by Prabitz et al.

The electrical contact resistance was determined experimentally for room temperature according to the ISO18594 standard. Values for simulation input were:

- Resistance electrode – upper sheet: 0.033 mOhm

- Resistance sheet-sheet: 0.006 mOhm

- Resistance electrode – lower sheet: 0.014 mOhm

5.3 Simulation Model Validation

As the electro-thermo-mechanical resistance spot welding simulation models were extensively used and validated by the authors in previous work, this study only contains a check of the model results against experimental cross-sections. Figure 5-3 depicts the comparison between experimental and simulated nugget shapes for MTC2 and MTC3. The experimentally observed nuggets are outlined in black and overlayed onto the simulation results (right side of the Figure). It is clearly visible, that the experimental and simulated nugget shapes match very well. With this result as well as prior experience, the simulation models were considered valid and were used throughout the project.
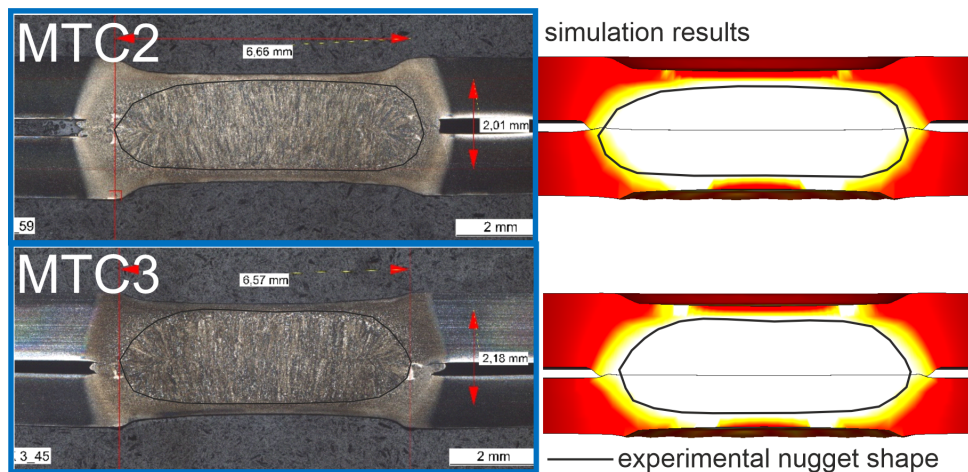

Figure 5-3:   Comparison of experimental and simulated nugget shapes for MTC2 and MTC3. The bright white area in the simulated results depicts temperatures over the melting point and corresponds to the weld nugget

5.4 S-Rail Simulation Model

The S-Rail simulation model was set up based on 3d-scans from as-delivered S-Rail components. In the workflow, a 3d-scan was conducted using a patterned light 3d-scanner (GOM ATOS). The resulting file was cleaned up (see Figure 5-4) and transferred to a finite element mesher (MSC APEX). In accordance with the academic model and previous studies, the joining areas were meshed using hexahedral elements in a circular pattern to account for the axi-symmetrical nature of the RSW process. All other areas of the component were meshed using progressively larger

elements the further away they were located from the weld zones. Two elements were used over the thickness of the part, with an additional local refinement step in a diameter of 6 mm around the weld zones, resulting in a total of four elements over the thickness for the weld areas. In total, 17,628 elements were used for the S-Rail, 11,894 elements for the base plate. For the temporal resolution, a constant time-stepping of 0.009 s was chosen both for the welding and cooling periods.
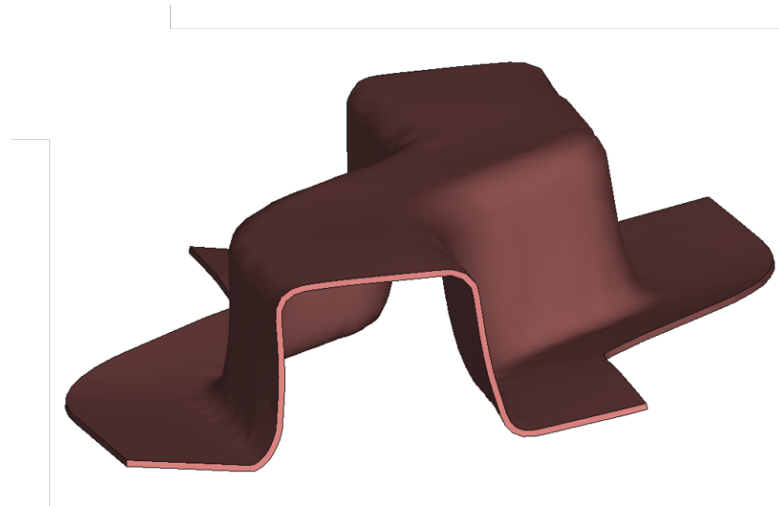

Figure 5-4: 3d-scanned S-Rail after model clean up

Figure 5-5 shows the assembled simulation model prior to starting a calculation. The bottom sheet was supported using a bearing in the central areas and at the edge to model the table in the experiments. Clamps were set-up at the four edges of the S-Rail. They were assigned a clamping force of 2 kN and a stiffness of 1 kN/m to push the springback-afflicted geometry downwards. The clamps were de-activated 5 s after the last weld to capture the residual deformations and stresses after the process. The S-Rail model was calculated on a workstation using an Intel XEON 2295 CPU and 64 GB RAM in 15.9 hours.
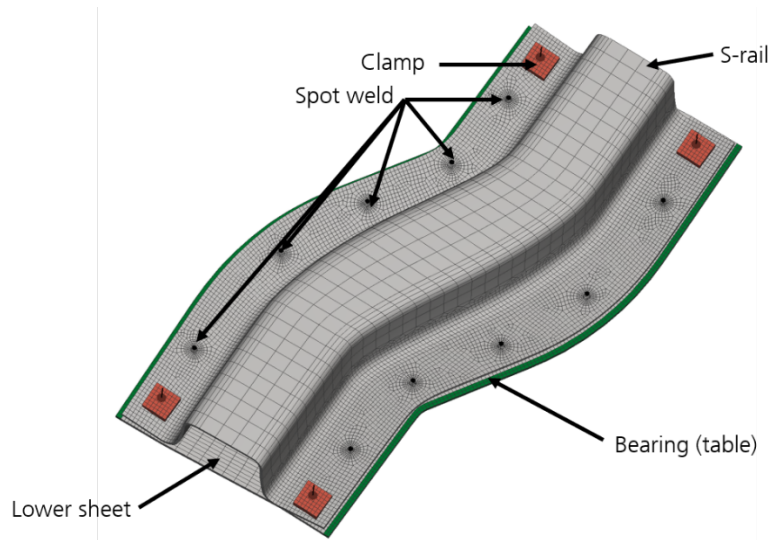
Figure 5-5: Depiction of the simulation model before the calculation

In order to classify the effects arising from springback, a finite element model with straight flanges was constructed. The flanges were straightened by projecting the elements in the flange onto a parallel plane aligned to the lowest coordinates of the scanned geometry. No other geometrical alterations were carried out. A depiction of the straightened part is shown in Figure 5-6. The springback-afflicted geometry will be referred to as 'actual geometry', the straightened part as 'idealized geometry' throughout this work.

Figure 5-6: Straightened (green) and springback-afflicted (blue) geometries.

5.5   LME Occurrence Criteria

The goal of LME occurrence criteria is to create a simple formula to assess LME risk in a certain joint and to compare the risks between process parameters and – possibly even – materials. Ideally, the criterion takes process factors on LME into account and results in a single value determined both by experiment and simulation.

An LME criterion that was published by the authors in a prior work [3] is shown in Equation (1). This criterion calculates an average sink-in velocity v_{Elec} of the electrode into the LME sensitive material by dividing the 70% of the maximum electrode sink in $d_{ElecMax}$ by the time it takes to reach this value $t_{weld}\{0.7 * d_{elec}\underset{Max}{}\}$.

$$v_{elec} = \frac{0.7 * d_{elecMax}}{t_{weld}\{0.7 * \underset{Max}{d_{elec}}\}} \tag{1}$$

The second LME criterion evaluated during this project was first published by [4]. It evaluates the LME risk by dividing the local maximum principal stress by the temperature dependent yield stress. As the material temperature changes rapidly, this normalization of the current stress by the maximum stress from thermal softening becomes necessary. The thermal softening used for this study can be found in Figure 5-2. The criterion is only activated once surface temperatures of 420°C are exceeded, i.e. liquid Zinc is available on the surface. In the original work, the LME criterion was cut off above a surface temperature of 900°C because Zinc evaporates from the surface at this temperature. Throughout this project, even when exceeding surface temperatures of 900°C. LME could still form. Possible explanations are that Zinc has already diffused into grain boundaries during heating or that the evaporation is not instantaneous, and Zinc remains on the surface for a certain time even when exceeding 900°C surface temperature.

$$IF\ Temperature > 420°C \quad\quad THEN$$

$$LME_{Risk} = \frac{maximum\ principal\ stress}{temperature\ dedependent\ yield\ stress} \tag{2}$$

During the course of the project, the stress-based criterion was regarded both over the weld time and compared using the maximum value reached. An experimental change to the criterion from Equation (2) was tested towards the end of the project. It involves integrating the equation over time and is shown in Equation 3.

$$IF\ Temperature > 420°C \quad THEN$$

$$LME_{Risk} = \int_{t}^{\Box} \frac{maximum\ principal\ stress}{temperature\ dedependent\ yield\ stress}\ dt \tag{3}$$

The idea behind this change is that the maximum value of the stress-based criterion is usually only reached in a single simulation time step and might not be the best value to compare different setups. The plot of the criterion over time contains more information but is difficult to interpret. With the integrated criterion, a single value is derived that encompasses both the stress history at a single location as well as the temperature exposure duration. The temperature exposure duration is considered because the criterion is set to 0 if the surface cools below 420°C.

6   Results and Discussion

6.1 LME Evaluation on Academic Samples

6.1.1   Experimental LME Sensitivity Studies on Academic Samples

Initially, to analyze the weldability of all MTCs and select the welding parameters required for subsequent LME sensitivity assessment, the weldable current range (WCR) of all planned MTCs in this project was investigated according to SEP1220-2 [5]. The results, shown in Table 6-1, indicate that all MTCs have a weldable current range greater than 0.5 kA. In the subsequent LME sensitivity assessment experiments, to ensure sufficient heat input while avoiding welding expulsion, the welding current was set to I_{max}-0.2kA for each MTC.

Table 6-1: Overview of the weldable current range (WCR) of all the investigated MTCs.

MTC	I_{min} in kA	I_{max} in kA	WCR in kA
1	8.6	9.5	0.9
2	6.2	8.7	2.5
3	6.4	8.5	2.1
4	7.0	8.3	1.3
5	7.6	8.2	1.6

Since the welding current remained constant, to achieve varying heat inputs in the LME sensitivity assessment, were employed the same method used in phase 1 of the LME project. This involved increasing the welding duration to 2, 3, and 4 times the standard welding time. Figure 6-1 presents the results of the LME sensitivity evaluation for MTC1 academic samples. After observing more than 20 repeated experiments, we found that with increased welding time, the proportion of samples with LME cracks gradually increased, as did the severity of the cracks. Evaluating the classification of LME cracks, the types were primarily A and B, with only a few C-type cracks observed in samples with welding times 2 and 3 times the standard duration. Compared to MTC1, the other four MTCs did not exhibit LME sensitivity in academic samples, even with welding

times extended to four times the standard duration. This highlights the low LME sensitivity of the latest third-generation AHSS.
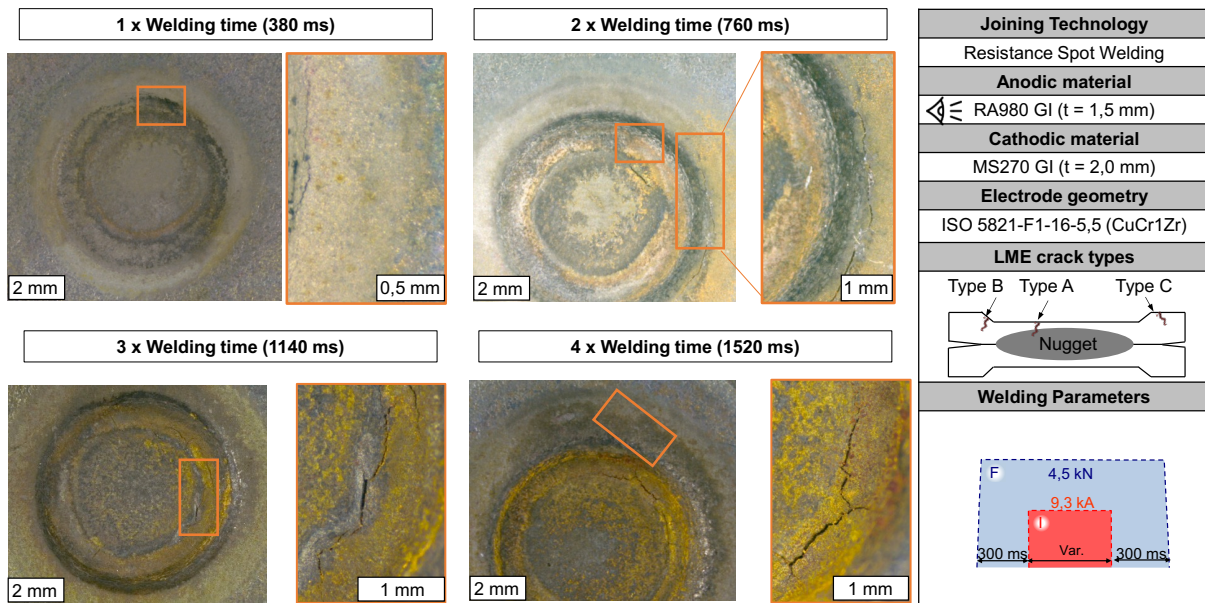

Figure 6-1: Evaluation of the LME-susceptibility of MTC 1

Subsequently, to further assess the LME crack sensitivity of third-generation AHSS in academic samples, a 3° electrode misalignment was introduced. The results are shown in Figure 6-2. Under these conditions, MTC2, MTC3, and MTC4 did not exhibit any LME cracks. MTC5 exhibited minor LME cracks, primarily of type B. Compared to these four MTCs, MTC1 showed a significant increase in both the intensity and number of LME cracks, primarily of type A. These cracks were mainly concentrated at the inner edge of the indentation.
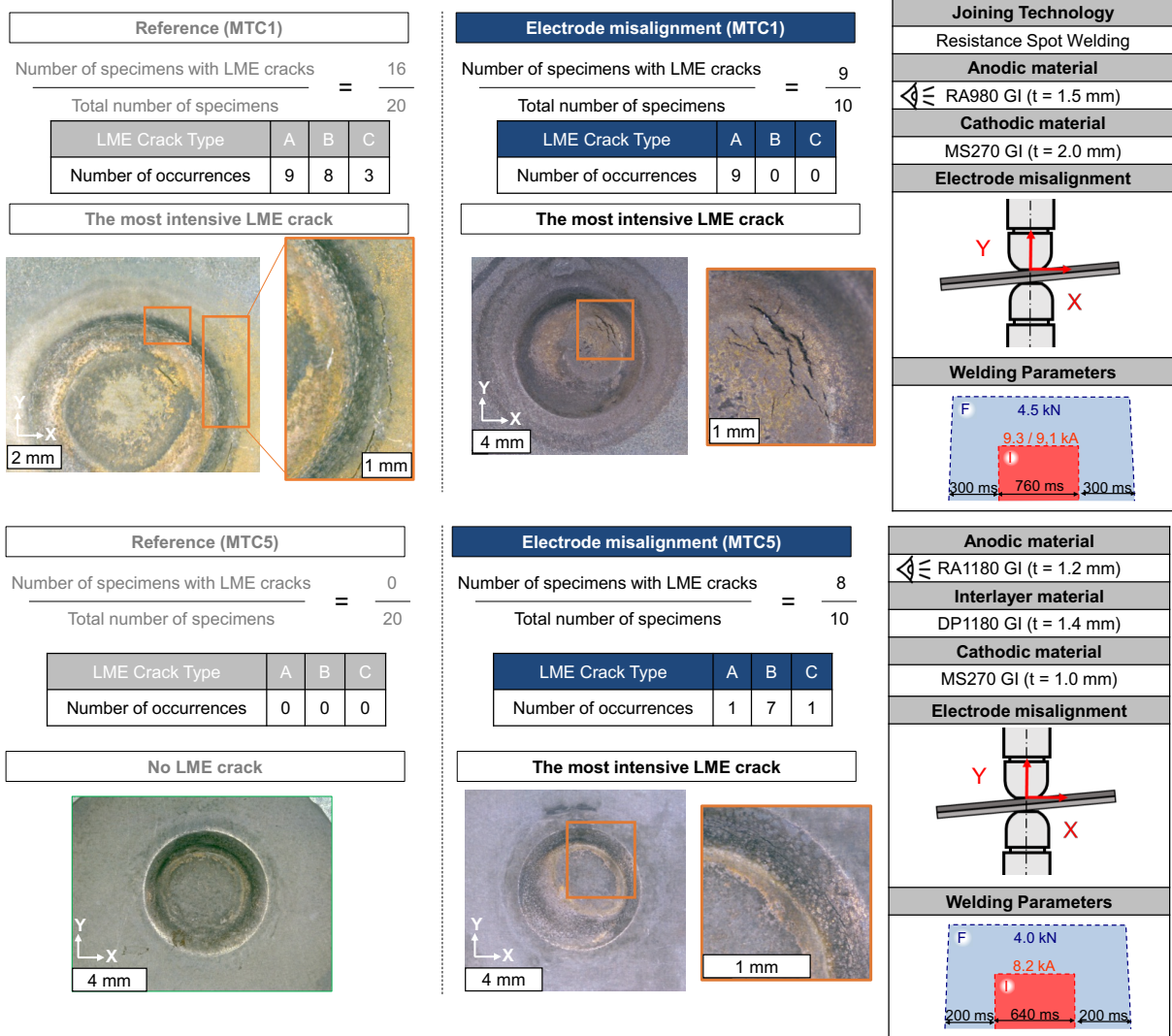
Reference (MTC1)			
Number of specimens with LME cracks		=	16
Total number of specimens			20

LME Crack Type	A	B	C
Number of occurrences	9	8	3

The most intensive LME crack

Electrode misalignment (MTC1)			
Number of specimens with LME cracks		=	9
Total number of specimens			10

LME Crack Type	A	B	C
Number of occurrences	9	0	0

The most intensive LME crack

Joining Technology
Resistance Spot Welding
Anodic material
RA980 GI (t = 1.5 mm)
Cathodic material
MS270 GI (t = 2.0 mm)
Electrode misalignment
Welding Parameters

F 4.5 kN
9.3 / 9.1 kA
300 ms 760 ms 300 ms

Reference (MTC5)			
Number of specimens with LME cracks		=	0
Total number of specimens			20

LME Crack Type	A	B	C
Number of occurrences	0	0	0

No LME crack

Electrode misalignment (MTC5)			
Number of specimens with LME cracks		=	8
Total number of specimens			10

LME Crack Type	A	B	C
Number of occurrences	1	7	1

The most intensive LME crack

Anodic material
RA1180 GI (t = 1.2 mm)
Interlayer material
DP1180 GI (t = 1.4 mm)
Cathodic material
MS270 GI (t = 1.0 mm)
Electrode misalignment
Welding Parameters

F 4.0 kN
8.2 kA
200 ms 640 ms 200 ms

Figure 6-2: *Evaluation of the LME susceptibility of MTC 1 (upper) and 5 (lower) with disturbance due to a 3° electrode misalignment (right) in comparison to reference (left)*

6.1.2   Generation and Testing of Additional MTC6

Given the generally low or non-existent LME crack sensitivity of the planned MTCs, a new MTC, named MTC6, was created using available materials. It consists of 1.4 mm thick RA1180 EG on the anode side and 2 mm thick mild steel on the cathode side. This stack-up ensures that the AHSS on the anode side generates more heat during welding, subjecting the material to greater thermal load and thus creating favorable conditions for LME crack formation. Generally speaking, this MTC utilizes a very thick mild-steel joining partner, which would not necessarily be employed in such a manner

in automotive manufacturing. MTC6 can be considered more as an academic exercise in forcing LME occurrence for the sake of this study.

Following the same LME sensitivity evaluation steps as in section 6.1.1, Figure 6-3 shows the test results for the newly formed MTC6. It was observed that, compared to MTC1, MTC6 samples developed LME cracks - even at standard welding time. With further extension to two times welding time, MTC6 displayed LME crack intensity far exceeding that of MTC1 at 4x welding time, particularly showing longer B-type cracks (nearly one-third of a circle). As the welding time extended to four times the standard duration, not only did the crack width increase, but the number of LME cracks in each sample also rose. This conclusion validates the aforementioned selection criteria.
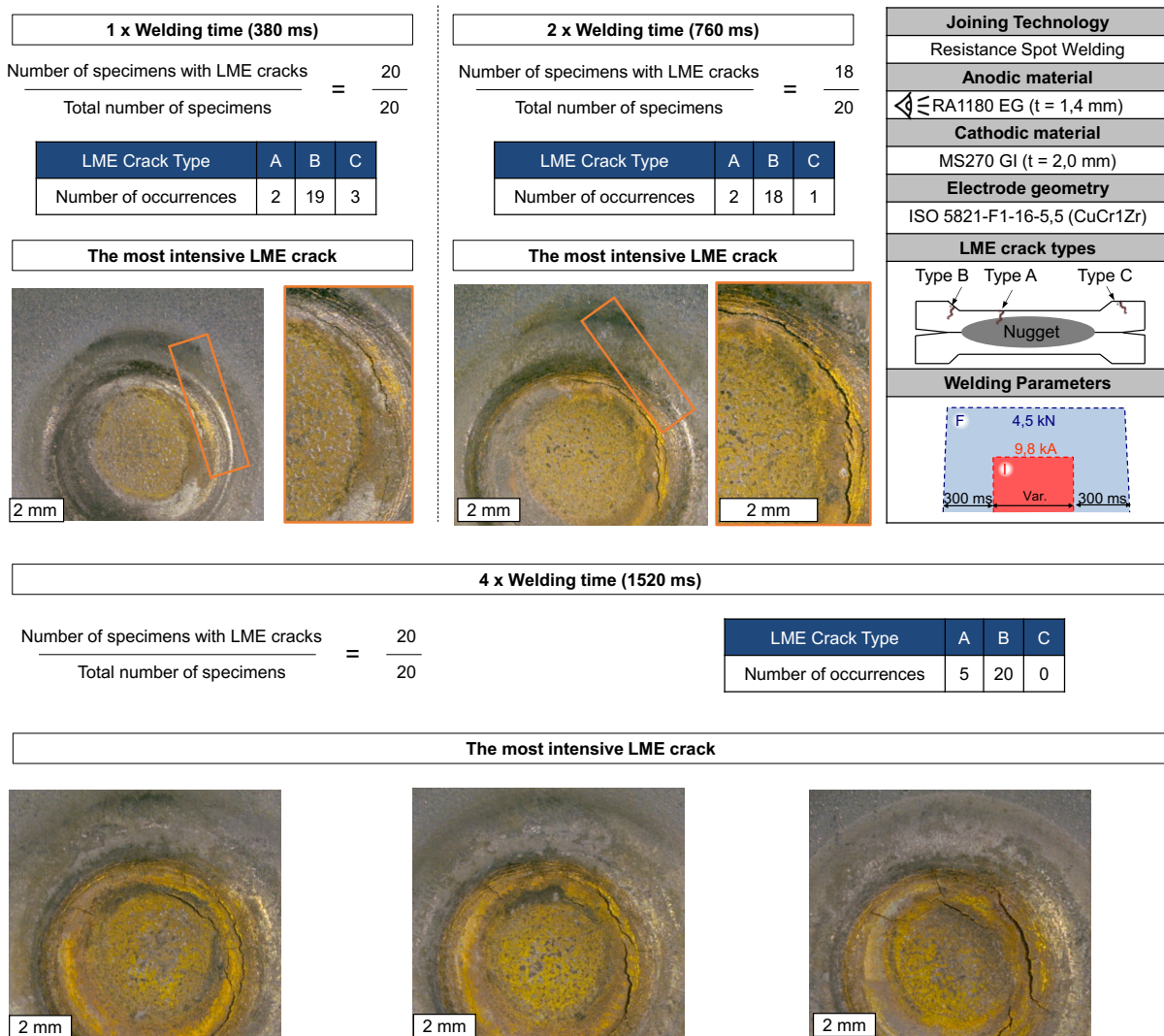
Figure 6-3: Evaluation of the LME-susceptibility (MTC 6)

Subsequently, as in section 6.1.1, the LME crack sensitivity of MTC6 was further evaluated under a 3° electrode misalignment, as shown in Figure X. Here, it can be observed that MTC6 is extremely sensitive to this disturbance, exhibiting severe LME cracks that penetrate the weld surface. This result further validates the high LME sensitivity of MTC6.
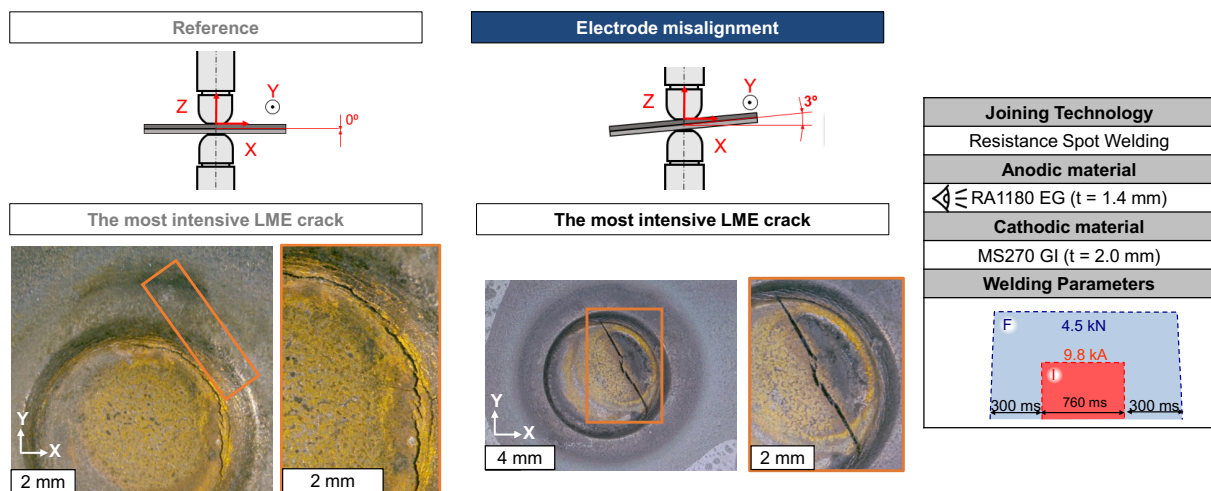
Figure 6-4:   Evaluate the LME susceptibility of MTC 6 with disturbance due to a 3° electrode misalignment *(right)* in comparison to reference *(left)*

6.1.3   LME Simulation of Academic Samples

During the pre-trials, several MTCs were tested for their LME sensitivity. Especially MTC2 and MTC6 were chosen for further analysis as they both use the same top sheet (1.4 mm RA1180EG) but different bottom sheets (1.4 mm RA1180EG for MTC2 and 2.0 mm MS270GI for MTC6). During preliminary trials, LME was observed on MTC6 but never on MTC2.

Using the simulation, conditions during welding are compared. Figure 6-5 depicts the temperature evolution on the surface for single (black), double (blue) and quadruple (pink) weld times in MTC2. With increasing weld times, the surface temperatures rise and the durations of sustained temperatures above 420°C (notable for the melting point of Zinc) and 700°C (notably for the beginning of the formation of brittle Fe-Zn intermetallic phases) rises. This behavior is to be expected as more heat is added to the weld with increased weld time. A longer exposure to high temperatures is a known

influence factor on LME formation and serves for comparison of the two different MTCs in this case.
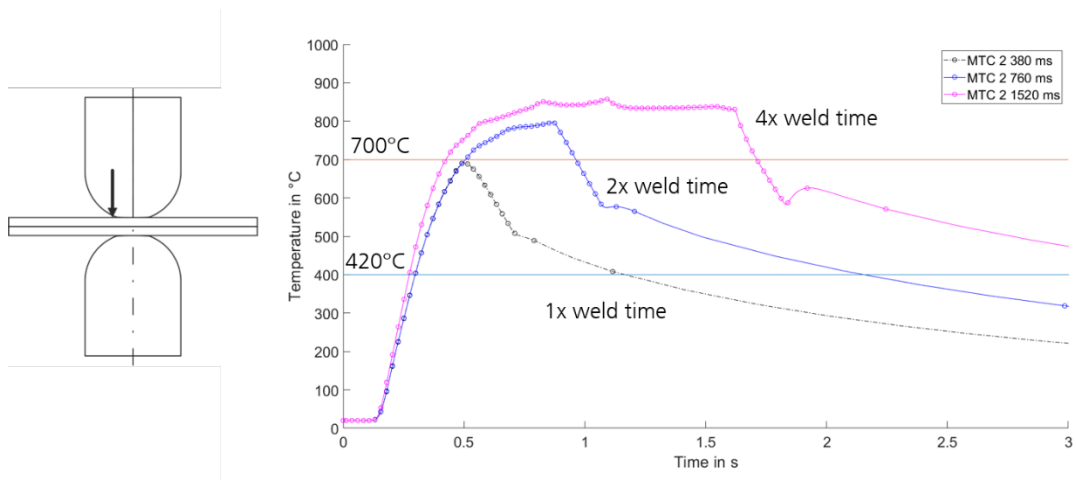

Figure 6-5:   Evaluation of surface temperatures in regard to weld time at a measuring point 1 mm from the edge of the indentation for MTC2

In Figure 6-6 the surface temperatures for MTC2 and MTC6 are compared with doubled (760 ms) weld time. It can be observed that MTC6 is subjected to 46% prolonged duration above 420°C and a 41% prolonged duration above 700°C. The increased temperature exposure likely stems from the 12% higher welding current (9.5 kA for MTC6 in comparison to 8.5 kA for MTC2) and the increased resistivity of the relatively thick mild steel joining partner.
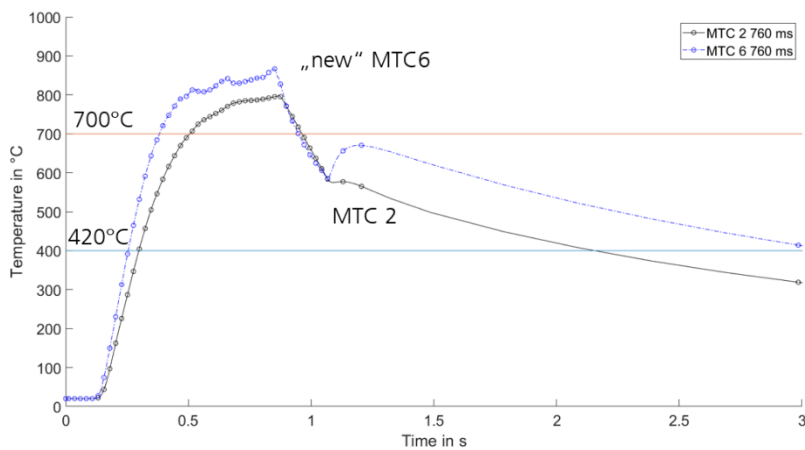
Figure 6-6:   Comparison of surface temperature evolution for MTC2 and MTC 6 with 760 ms weld time.

In addition to the temperature, the mechanical loading of the steel during welding is another known factor for LME formation. There are multiple ways to quantify the mechanical influence on LME. This chapter uses strain and indentation; a stress-based method is applied in the subsequent chapters.

Figure 6-7 depicts the surface strain rate at the location of observed cracks 1 mm from the edge of the indentation. MTC6 is exposed to significantly larger strain rates at the location of observed cracking. This leads to larger mechanical straining of the steel and is assumed to facilitate LME formation together with temperature exposure.
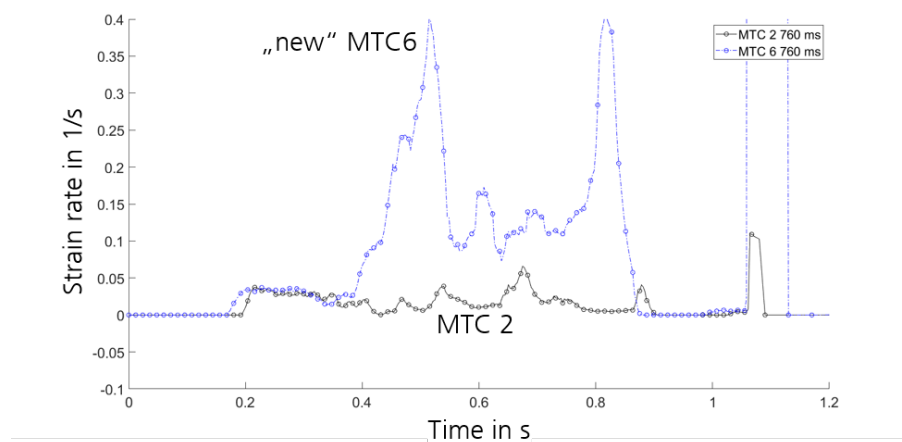
Figure 6-7: Surface strain rate comparison for MTC2 (black) and MTC6 (blue)

One goal of this work is to qualify easy-to-use LME evaluation methods and while the strain rate is suspected to be a driving influence factor on LME formation, it fluctuates strongly over a welding process. In addition, experimental determination of the strain rate this close to the weld zone is extremely difficult and not feasible in an industrial context. Therefore, a simplified method was developed, using the electrode position to derive an average sink-in velocity (according to Equation 1). Figure 6-8 depicts the position of the electrode sinking into the LME afflicted AHSS. For MTC2, the indentation is significantly slower than for MTC6. The straight lines overlayed on the graphs indicate the average electrode indentation velocity, which is 80% larger for MTC6 with 0.72 mm/s in comparison to 0.4 mm/s.
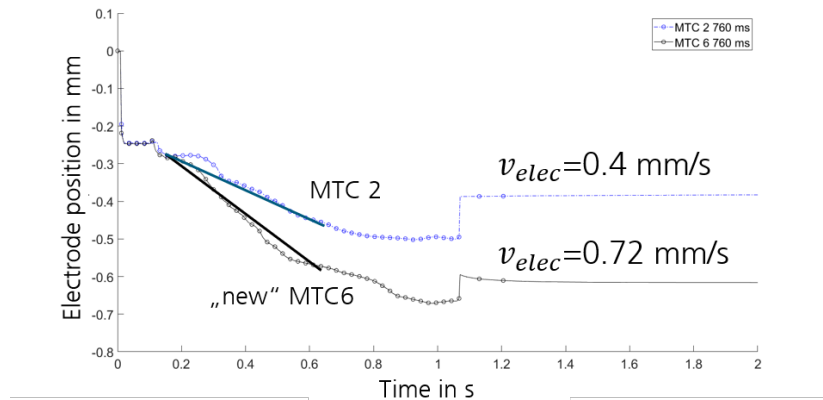
Figure 6-8: Electrode position comparison for MTC2 and MTC6

In summary, MTC6 shows a significantly higher LME susceptibility because the same AHSS is subjected to higher surface temperatures as well as larger mechanical forces from the resistance spot weld. This is caused by the higher welding current as well as the higher resistivity of the thicker mild-steel joining partner.

6.1.4   Evaluation of Stress-based LME Criterion for MTC2 and MTC6

Using the stress state during and after welding is another method to assess LME susceptibility. Following Equation (2), a stress-based criterion is defined by dividing the current maximum principal stress by the temperature-dependent yield stress of the material. A graphical evaluation of MTC2 with increasing weld times is shown in Figure 6-9. It is visible that the maximum observed LME risk factor rises with increasing welding time, following the experimentally observed behavior and the simulation results in the previous chapter.
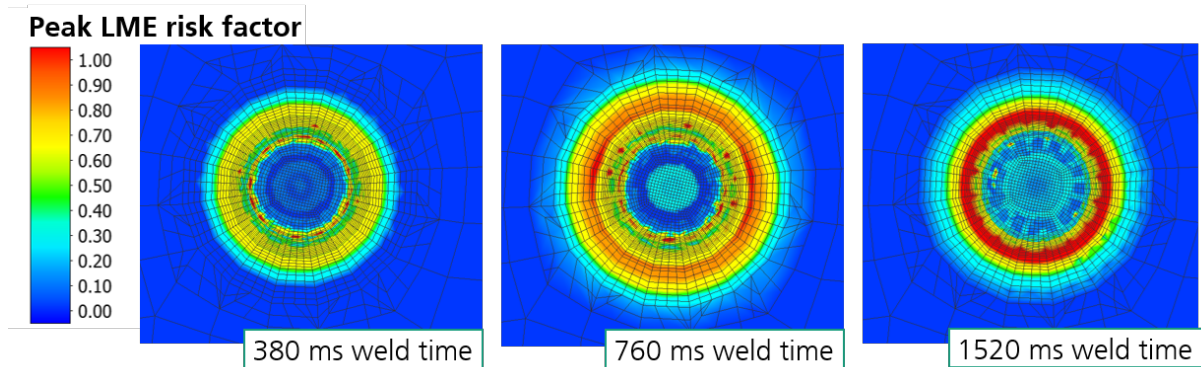
Figure 6-9: Peak stress-based LME criterion for different weld times in MTC2

Figure 6-10 shows a plot of the stress-based criterion over time for two different measurement locations. The criterion is only defined when the surface temperature at the location is above 420°C, otherwise it is set to Zero as no LME formation is expected, when Zinc is not liquefied on the surface. The formation of principal stress is strongly location dependent. The measuring point at the shoulder is the most highly loaded area in most cases.
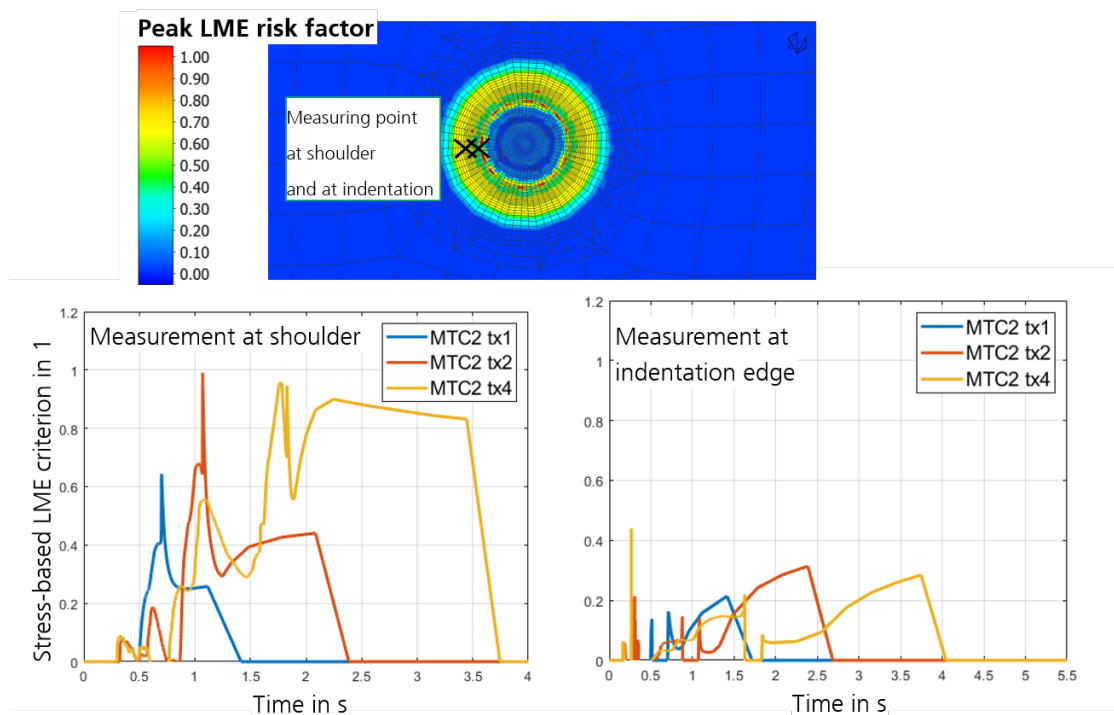
Figure 6-10: Stress-based LME criterion over time at two different locations. The "indentation edge" is located directly outside of the contact area with the electrode and the "shoulder" point corresponds to the previously evaluated location 1 mm from the edge of the indentation

A comparison between MTCs 2 and 6 is shown for the shoulder location in Figure 6-11. Consistent with experimental observations, MTC6 shows a far higher and more lengthy stress-based criterion response.
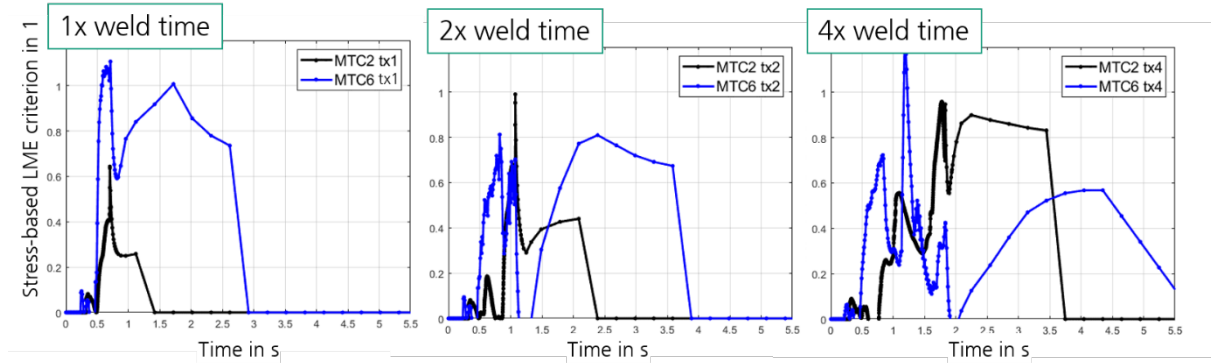
Figure 6-11:   Comparison of the stress-based LME criterion for MTC2 and MTC6 with different welding times

6.1.5   Tilted Electrodes Simulation

In order to evaluate manufacturing-based imperfections such as tilted electrode caps, the stress-based criterion is more suitable as the average electrode sink-in velocity is not well defined for electrodes with tilt. Figure 6-12 shows the simulated cross section and the peak stress-based LME criterion for 5° tilted electrodes. It can be observed that the deeper side, where the electrode sinks in strongly, and the angle point, around which the electrode "tilts" show a stronger criterion response than the higher side.
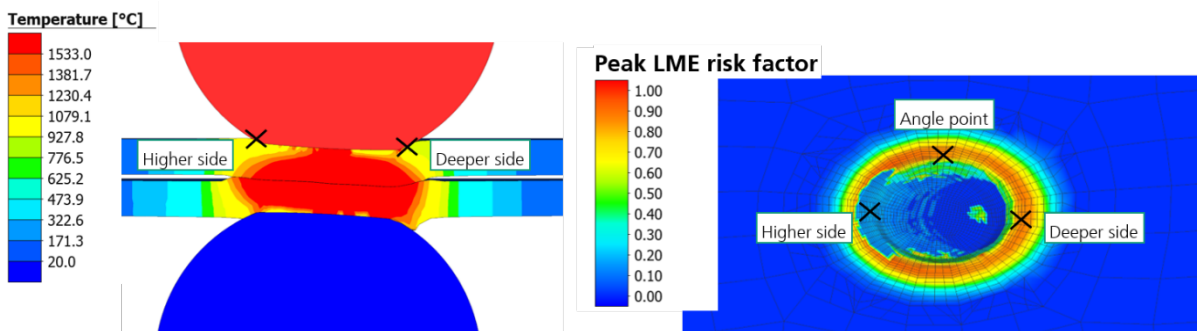
Figure 6-12: Cross section and peak LME risk factor for 5° tilted electrodes

The criterion is plotted over the welding and cooling time in Figure 6-13. In comparison with the reference case welded without tilt, only the angle point shows a markedly higher criterion response over time.
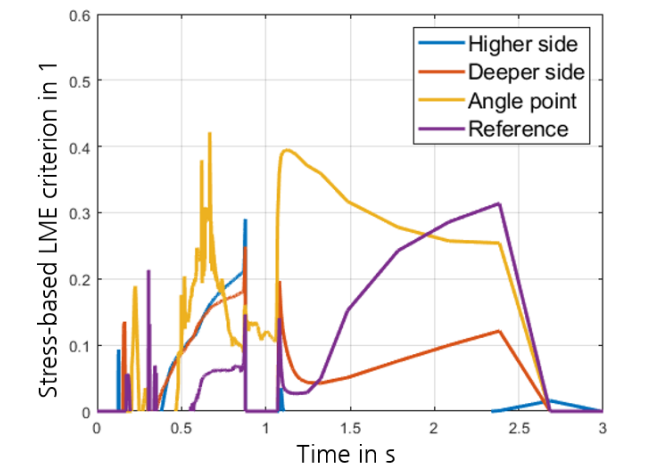

Figure 6-13: Stress-based LME criterion over time for tilted electrodes

The simulated behavior of largest criterion values for the angle point could be validated with experimental data: As shown in Figure 6-14, experimentally observed cracks occur also around the angle point and not on the higher side (H) or deeper side (D).
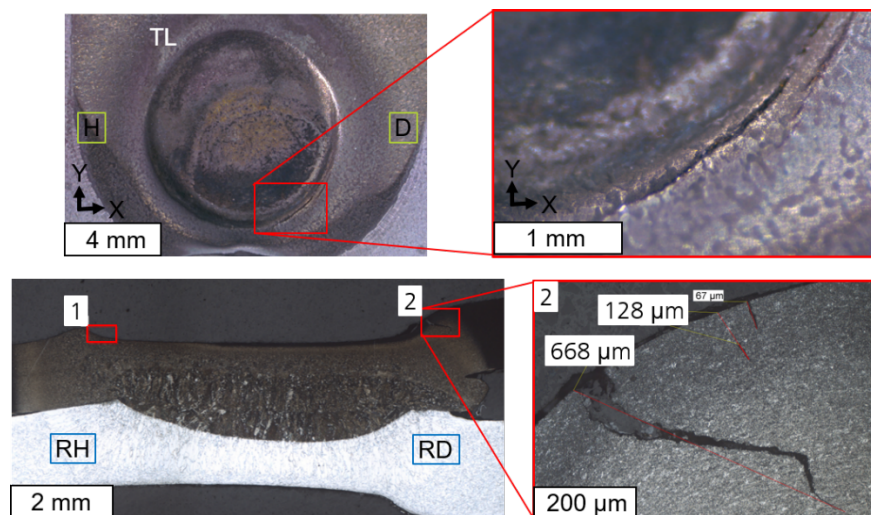
Figure 6-14: Crack evaluation of a 5° tilted electrode weld on an academic sample of MTC6

6.2   S-Rail LME Tests

6.2.1   Experimental Investigation of S-Rail LME
Susceptibility

In the S-Rail experiments, the principle of controlled variables was followed, selecting MTC1, MTC2, and MTC6 for LME sensitivity testing under S-Rail dimensions. The difference between MTC1 and MTC6 is the AHSS material used, while MTC2 and MTC6 differ in that MTC2 uses two identical RA1180 EG sheets. The AHSS always positioned on the anode side during welding (RA980GI in MTC1 and RA1180EG in MTC2 and MTC6) was formed into S-Rails by stamping, while the cathode side sheet was laser-cut to match the S-Rail contour.

Before starting the welding experiments, the stamped S-Rail components were characterized, focusing on the coating thickness in the flange area. Literature indicates that this is a crucial factor affecting LME sensitivity; a reduction in coating thickness decreases LME crack sensitivity. Figure 6-15 compares the coating thickness before and after stamping in the flange area. No significant change in coating thickness was observed, eliminating the possibility of stamping-induced thickness reduction affecting the accuracy of the experimental results.
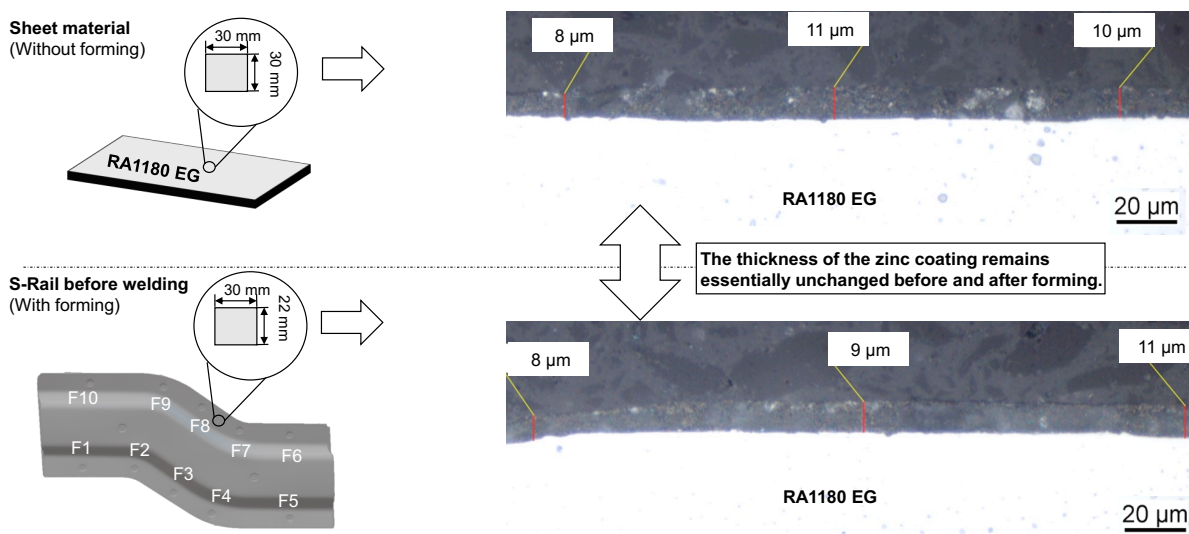

Figure 6-15:   Influence of forming process on coating thickness

Subsequently, the geometric dimensions of the S-Rail components were characterized (see Figure 6-16 (a) and (b), and after clamping Figure 6-16 (c)), with a 1.4mm thick RA1180 (1655) used as an example.
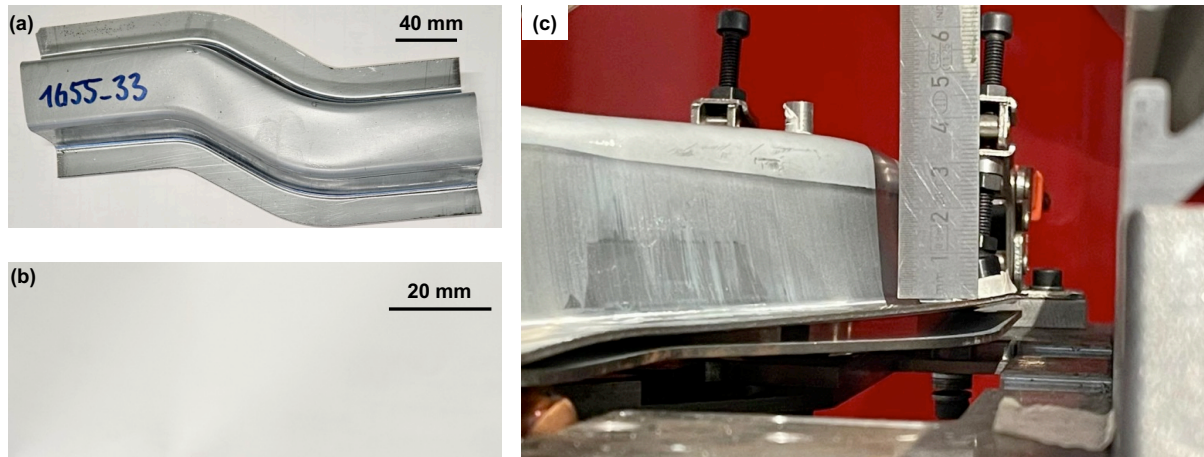

Figure 6-16:   Geometric characterization of the S-Rail component (a) and (b), and after clamping with the fixture (c) using RA1180 (1655) with a thickness of 1.4mm as an example

It was observed that due to the high strength of this material, unavoidable springback occurred after stamping. Additionally, when clamped, the gap between the S-Rail and the base plate could reach up to 4.5 mm. Although this introduced a new variable into the experiment, it further approximated the real-world characteristics of the components. Based on the aforementioned characterization, the unwelded semi-component, clamped semi-component, and subsequently welded component were 3D scanned using GOM ATOS (see Figure 6-17). The data was then sent to Fraunhofer IPK to develop a numerical simulation model.
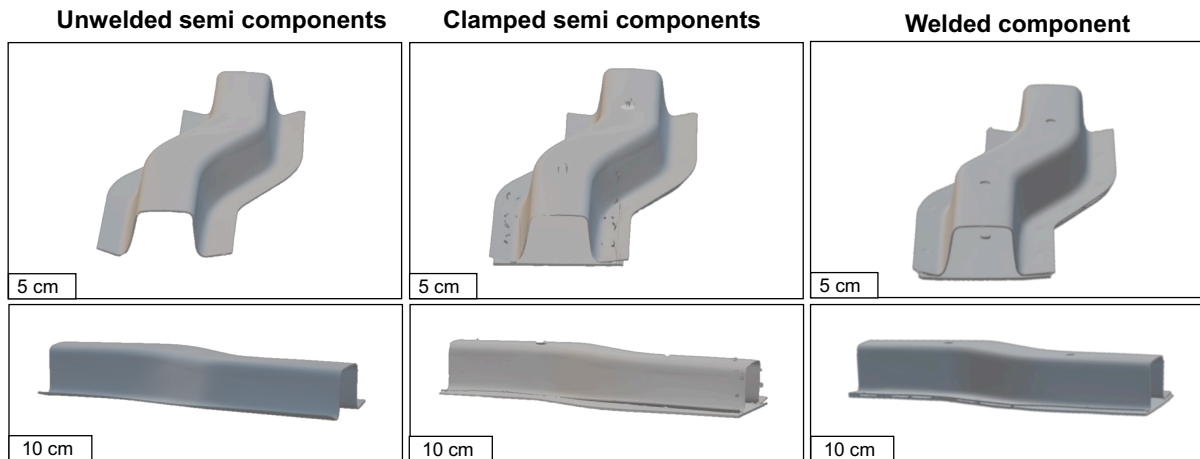
Unwelded semi components	Clamped semi components	Welded component
5 cm	5 cm	5 cm
10 cm	10 cm	10 cm

Figure 6-17: 3D scans of the S-Rail component before and after clamping.

Based on the observed springback phenomenon and its potential impact on LME crack sensitivity, this project conducted a preliminary investigation using MTC6 to determine the effect of springback at the flange of stamped S-Rail components on LME sensitivity. The purpose of this preliminary investigation was to establish the standard component.
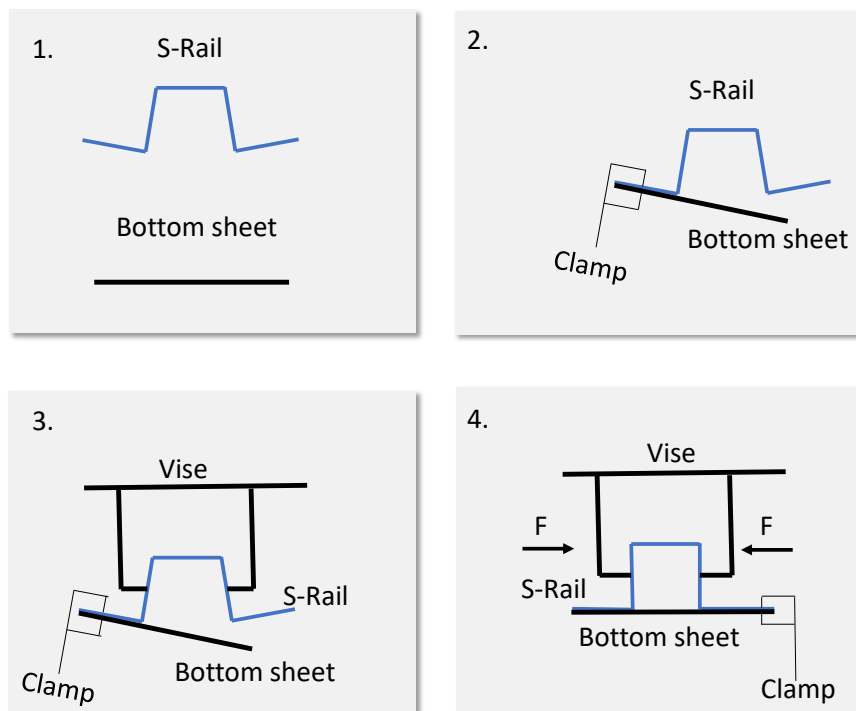
Figure 6-18: Procedure for manufacturing non-rebounding S-Rail components

The samples without springback were achieved by additionally clamping the flange area of the springback samples, as shown in Figure 6-18. After positioning the S-Rail component and the bottom sheet, one side was clamped using a clamp. Then, a vise was used to compress the side wall of the S-Rail component. Once the other side was aligned with the base plate, another clamp was used to secure the other side. The S-Rail components without springback, achieved using this method, are shown in Figure 6-19.
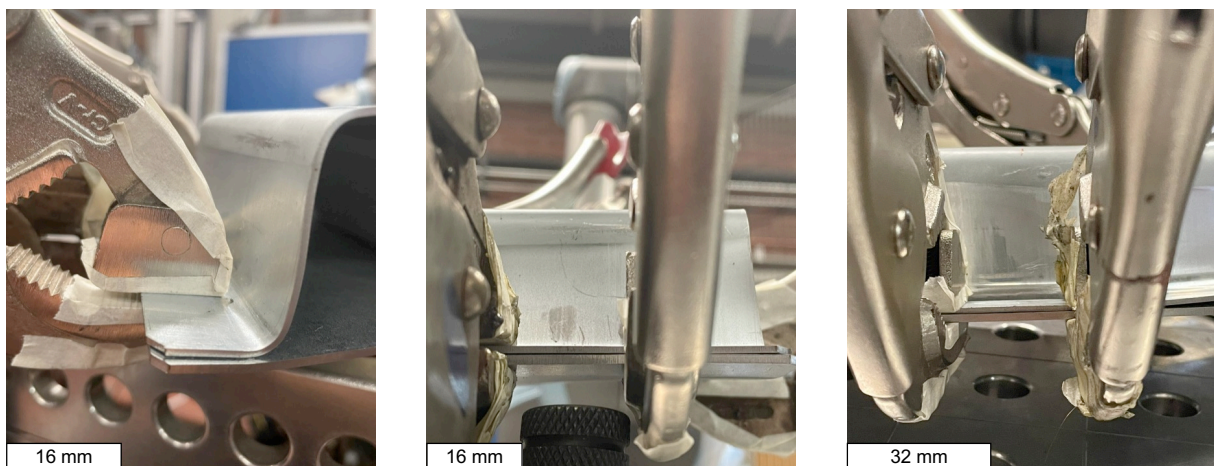
Figure 6-19:   Sampling of springback-free reference component

Comparison in Figure 6-20 showed no LME cracks in the samples without springback at twice the standard welding time. In samples with springback, the occurrence of C-type cracks increased and displayed an oval shape at the weld spot, likely due to more contact between the flange and electrode cap. Given the unavoidable springback in stamping for this steel grade, S-Rail samples with springback were defined as the standard component for this project.
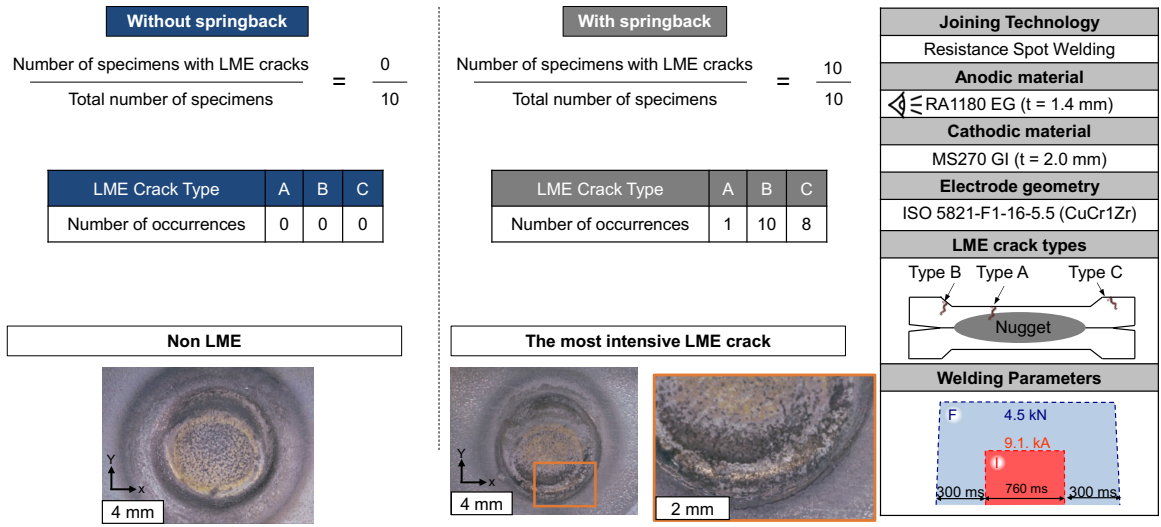
Figure 6-20: Influence of component springback on the LME-formation

Standard welding condition

Next, LME sensitivity in different MTCs was investigated under standard welding conditions with twice the standard welding time (see Figure 6-21). Firstly, in S-Rail dimensions, MTC2 exhibited moderate A-type and B-type LME cracks with depths of 949µm and 266µm, respectively. This contrasts with the low LME sensitivity observed in MTC2 during the coupon test, indicating a significant impact of sample size on LME sensitivity in joints made of the same AHSS. In comparison, MTC1 and MTC6 showed moderate lateral A-type cracks, notably near the springback side. MTC6 exhibited the most severe C-type cracks with a depth of 563 µm, consistent with its high LME sensitivity.
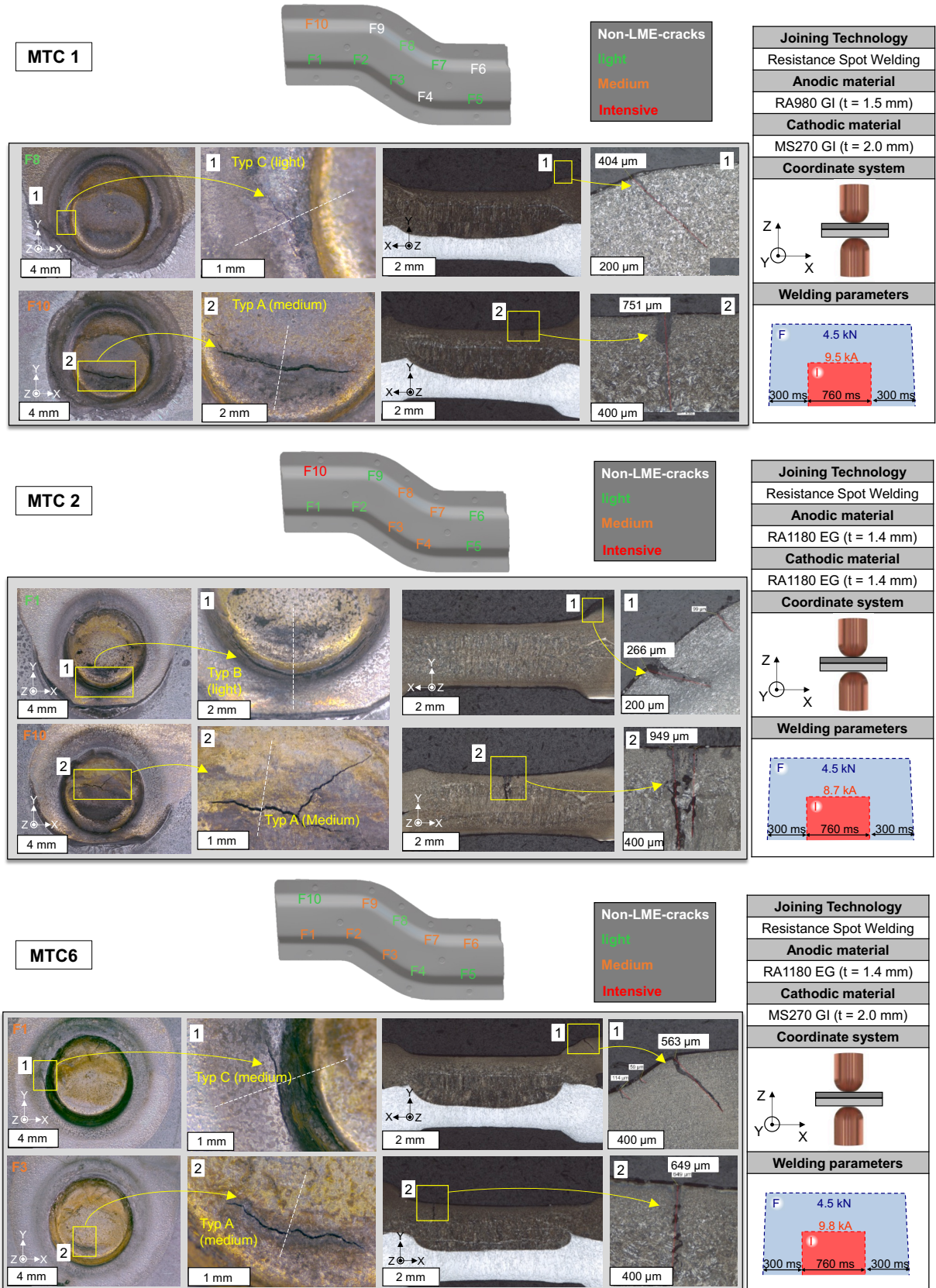
Figure 6-21:   Characterization of LME formation under standard welding conditions

Components with electrode misalignment

To further approximate real-world conditions, the introduction of electrode misalignment, a common disturbance in actual production, took place under standard conditions. The electrode cap was set at a 5° angle to the sheet surface (see Figure 6-22). Compared to standard conditions, electrode misalignment caused the LME cracks in MTC2 to extend outward, primarily presenting as C-type cracks in the heat-affected zone, with depths reaching up to 1000 µm, about 71% of the sheet thickness. In contrast, MTC1 and MTC6 did not show changes in crack location, still mainly exhibiting A-type LME cracks. However, the crack depth increased significantly with electrode misalignment, with A-type LME cracks in MTC6 reaching depths of up to 1000µm.
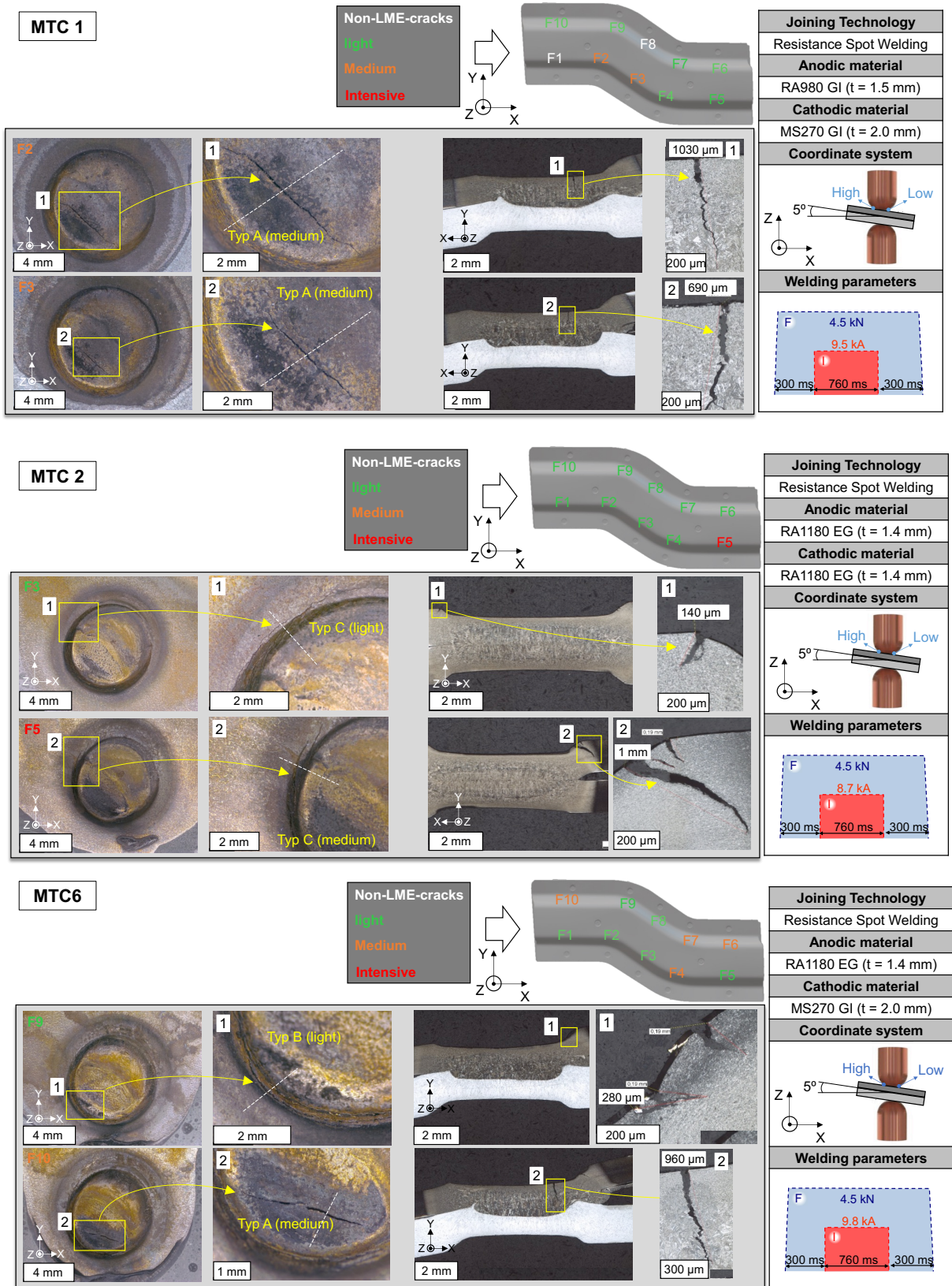
Figure 6-22: Characterization of LME formation under electrode misalignment.

Worst-case component

Finally, evaluation of LME crack intensity in S-Rail under worst-case conditions took place. In the worst-case scenario, in addition to electrode misalignment, the welding time was extended to four times the standard duration. The results are shown in Figure 6-23. It was observed that the LME intensity in all MTCs decreased, evidenced by reduced crack depth. This phenomenon might be due to the slowed growth of the weld nugget in the later welding stages, enhancing the cooling effect of the electrode cap and ultimately reducing the risk of LME crack formation.
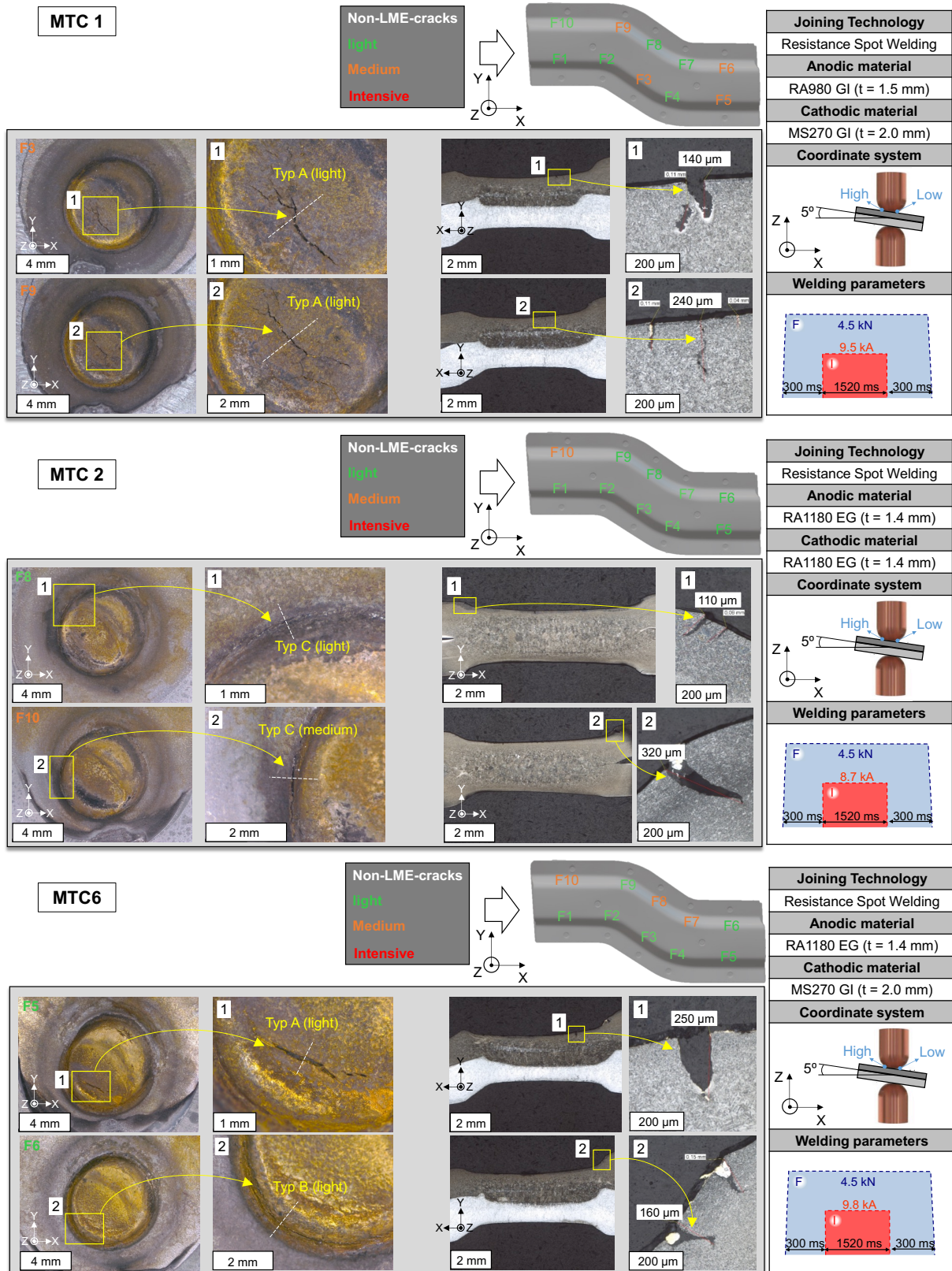
Figure 6-23: Characterization of LME formation under worst-case conditions (electrode misalignment 4x with elongated weld times).

6.2.2 Simulation Investigation of S-Rail LME Susceptibility

The S-Rail simulations were conducted using either an "idealized" geometry with a straightened flange or the "actual" geometry with a springback-afflicted flange derived from 3d-scans. MTC6 is used for all following evaluations unless noted otherwise. The resulting spot weld cross sections for both cases are shown in Figure 6-24. For the idealized geometry, the flange remains straight during and after welding. In the actual geometry, the flange is first pushed down by the electrode squeeze force and then relaxes back up on the side of the free end as the steel is softened by the heat input. The nugget diameter measures 7.2 mm for both cases, ensuring their comparability. The indentation depth is very different due to the springback: For the idealized geometry, it amounts to 0.45 mm from all sides, whereas it is 0.38 mm on the "left" side towards the rest of the geometry and 0.93 mm towards the free end, where the sheet bends upward. The measuring point is chosen, as before, 1 mm next to the edge of the indentation. The side facing the geometry is chosen for the measuring point as this location would conduct forces during the use-phase and cracking in this location is therefore of the highest interest.
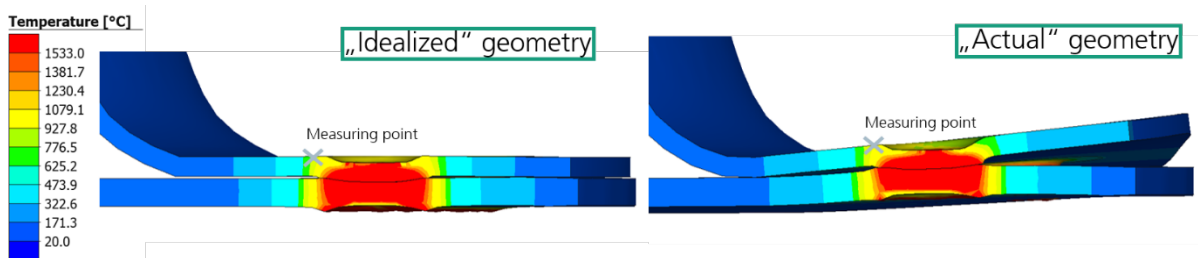

Figure 6-24:   Cross section after welding at spot number 2 for the idealized and actual geometry

In order to compare the results on the S-Rail with the academic sample, the temperature evolution is analyzed at first. Figure 6-25 compares the temperature exposure at all 10 welds on the S-Rail. As the RSW parameters were not changed, it is expected that the temperature exposure remains similar between academic sample, idealized and actual geometries. All spots show values that are very close to the 2.8 s of temperature exposure above 420°C determined on the academic samples. There

are slight differences between the idealized and the actual geometry, which are probably caused by the different contact conditions due to the slanted surface from springback. For spots 5 – 9 a slightly lower temperature exposure is visible. This may be due to positioning errors of the measuring point in the simulation. As the temperatures are very sensitive to the distance from the weld and the measurement data can only be extracted at node points on a large scale, slightly uneven mesh, small deviations are to be expected.
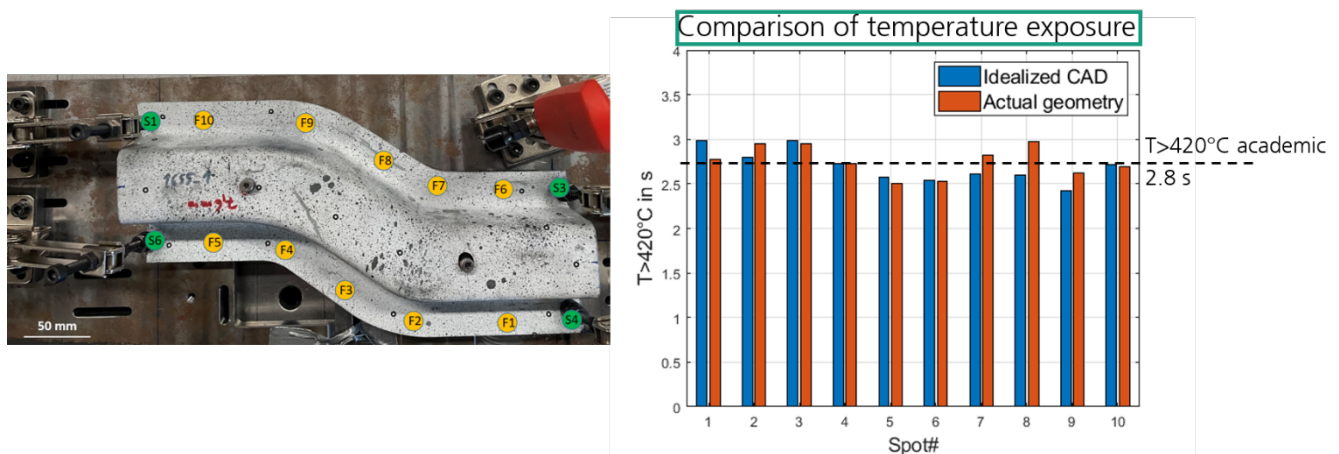

Figure 6-25:   Left: S-Rail photo and spot weld nomenclature; Right: comparison of duration of exposure above 420°C for the measuring point.

The next evaluation of the S-Rail LME susceptibility is conducted via the electrode indentation rate. At first, the electrode position is extracted at all 10 welds by subtracting the z-coordinate at the center of the weld by the z-coordinate at the measuring point. Then the data is shifted to start at the same time by subtracting the start time of a specific spot weld. The resulting electrode position curves are shown in Figure 6-26 for the actual geometry. There are no significant outliers for all 10 spots and the same behavior of sink in during welding and then constant depth during cooling is visible.
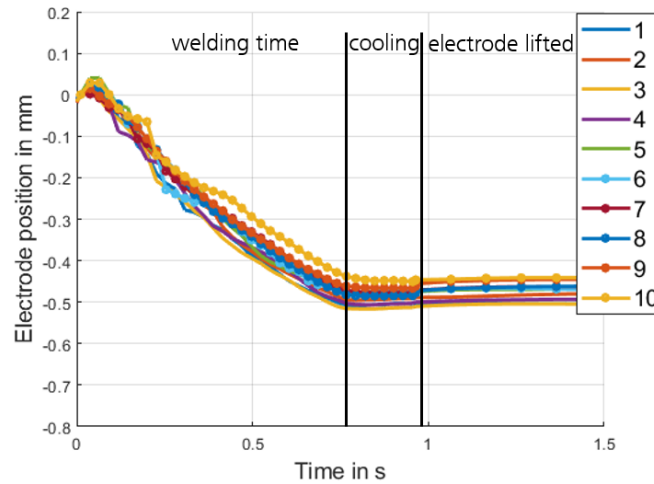
Figure 6-26: Electrode position over weld time for all 10 spots in the actual geometry

Figure 6-27 shows the comparison of the average electrode sink-in velocity (according to Equation 1) for all spots. A small increase in the sink-in velocity of under 10% is visible for the actual geometry for almost all spots. This behavior is to be expected considering that the springback afflicted flange pushes upwards during the welding process. Spots 7-10 show slightly smaller values. It could not be confirmed experimentally that these spots have a lowered LME sensitivity, so it is assumed that the results arise from the modelling of the slightly asymmetrical 3d-scanned S-Rail.

The results for the S-Rail show very close adherence to the academic sample result, especially for the idealized geometry. Overall, a very small increase in the LME susceptibility between a flat, academic sample and a springback-afflicted industrial geometry is expected according to the simulation results. As this difference appears to be similar for all locations, a geometric effect from the topology of the part could not be found at this point.
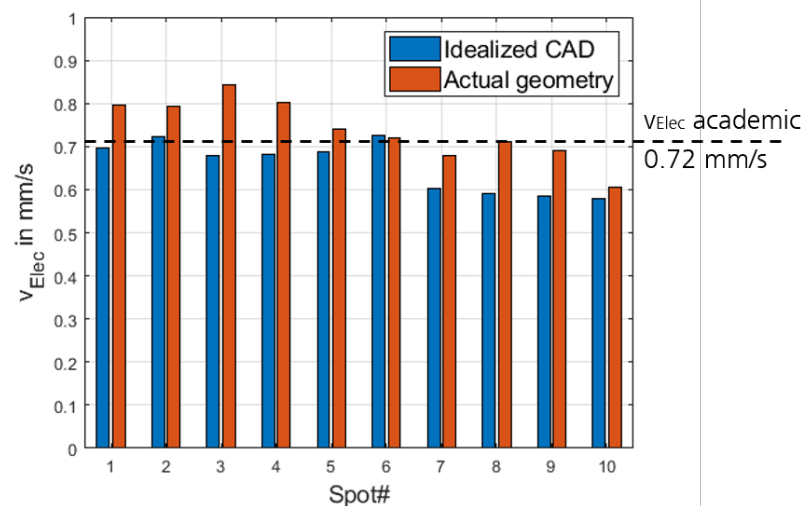
Figure 6-27:   Average electrode sink-in velocity for all 10 spots and the actual and idealized geometry

The next LME occurrence criterion to be evaluated is the stress-based criterion created by dividing the maximum principal stress by the temperature dependent material yield stress Equation (2). The peak value over the process time is shown for each spot in Figure 6-28.

The idealized geometry shows consistently lower criterion response than the actual geometry. It is notable though that the value for the idealized CAD is also significantly lower compared to the value derived on the academic sample. This is likely due to the different stiffness conditions around the idealized CAD: Whereas the academic sample is a flat sheet, the idealized S-Rail geometry is flat at the location of the weld but has significantly higher local stiffness due to the formed geometry. Even the actual geometry, for which a slightly elevated criterion response is expected, only barely reaches the value observed for the small academic sample. For the stress-based criterion, it can therefore be stated that a direct comparability to the academic flat specimen is not possible. However, the comparison between idealized and actual geometries are valid and the same trend albeit with a higher spread is observed as with the electrode indentation velocity in Figure 6-27. In general, a slightly increased LME susceptibility can be expected for the springback-afflicted geometry but no systematic effect of the topology of the part is observed.
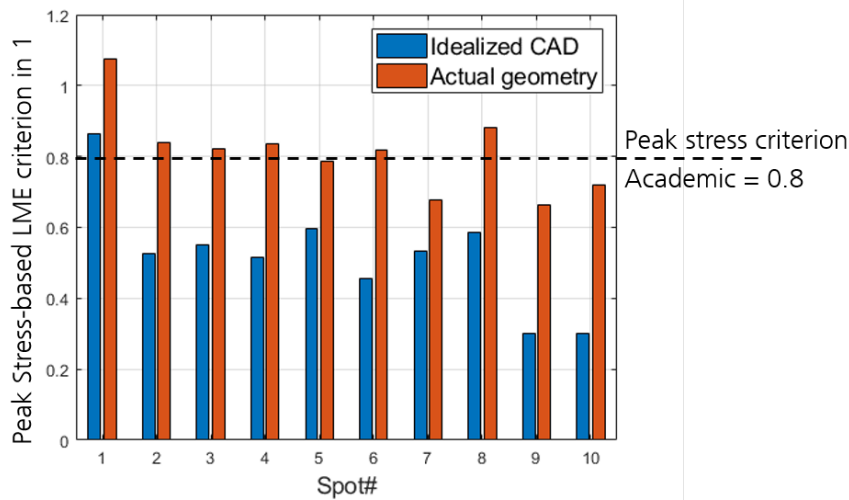
Figure 6-28: Comparison of peak stress-based LME criterion for all 10 spots between idealized and actual geometries

Figure 6-29 shows the stress-based LME criterion plotted over time for spots 1, 5 and 10. The comparison between the actual and idealized geometries show a similar qualitative behavior but consistently higher values for the actual geometry.
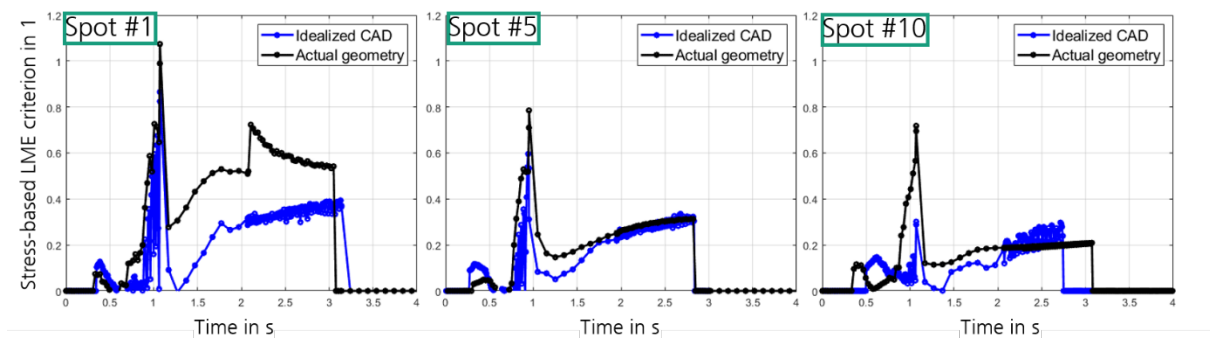

Figure 6-29: Stress based criterion over time for selected spots

6.2.3   S-Rail Simulation for Tilted Electrodes

As a common process deviation in industrial car body assembly, tilted electrodes were investigated. A very high tilt angle of 5° was chosen, because it is the maximum acceptable value in the production environment of several OEMs. Following the procedure depicted in Figure 6-30, the electrodes were tilted in the z-x-plane, orthogonally to the springback which was mostly oriented along the z-y-plane.
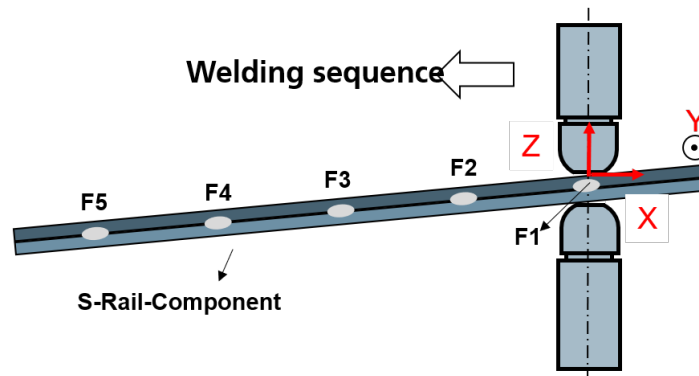
Figure 6-30: Setup for experiments and simulations with tilted electrodes

As with the academic samples, the peak stress-based criterion was extracted for the angle-point of each spot weld. The results are plotted in Figure 6-31. A similar behavior to the academic samples is observed, with a slightly elevated peak LME criterion value, describing the experimentally observed slight rise in the LME susceptibility with tilted electrodes.
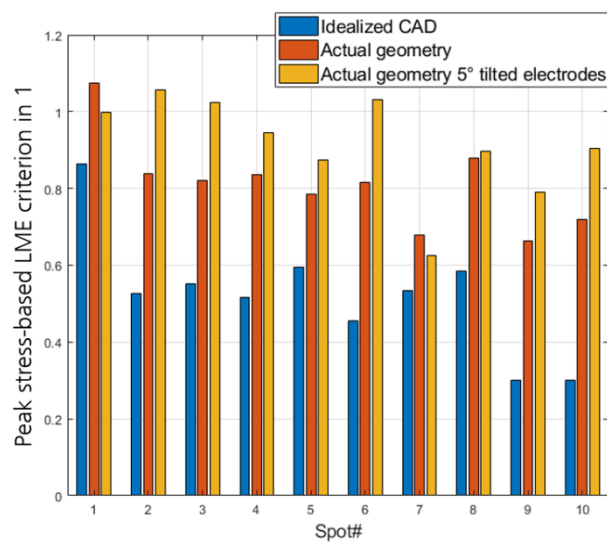

Figure 6-31: Results of the peak stress-based LME criterion for tilted electrodes on the S-Rail

6.3　LME Mitigation Measure Evaluation

6.3.1　Experimental LME Mitigation Investigation

To prevent LME cracks, this project validated the LME avoidance strategies developed with WorldAutoSteel in a prior project. The first strategy involves extending the hold time after the welding phase to prevent the electrode cap from leaving the material surface too early, which can cause the weld nugget's internal temperature to transfer to the surface, resulting in additional surface tensile stress and giving Zinc additional time to infiltrate grain boundaries. This avoidance strategy was first validated on an academic sheet metal sample and under worst-case conditions and in the most LME-sensitive MTC6. The results shown in Figure 6-32 indicate that, with all other conditions constant, increasing the hold time from 300ms to 800ms significantly reduced the number of LME cracks and their severity, which now only exhibited minor intensity levels.
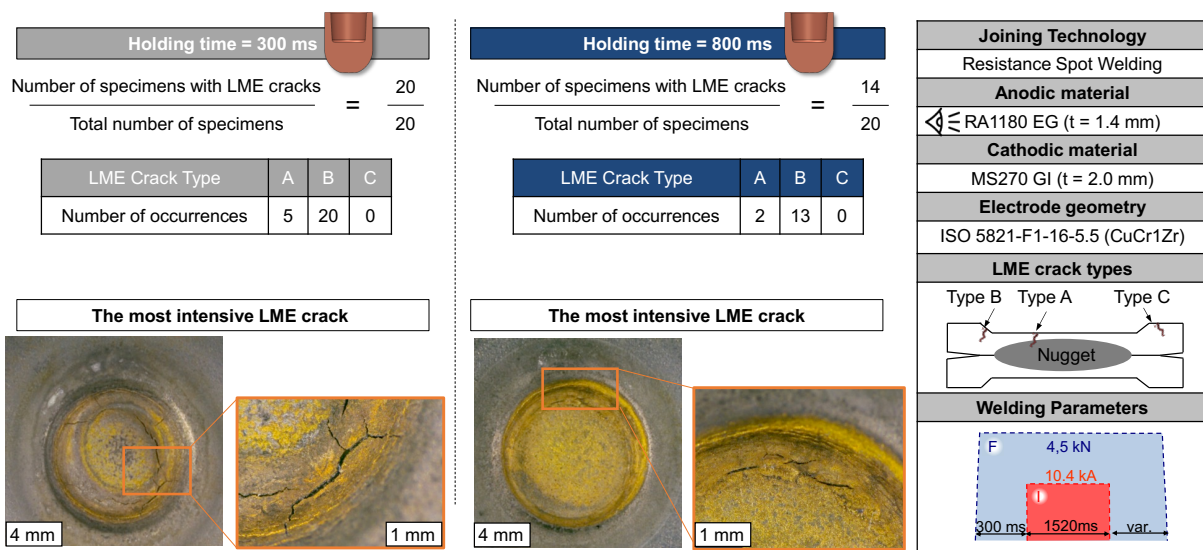

Figure 6-32: Validation of the LME avoidance strategy by extending the hold time

The second avoidance strategy involves increasing the working area of the electrode cap to reduce tensile stress caused by the electrode pressing into the sheet surface. The electrode cap used here was A0-100. To avoid reducing current density, which would decrease the weld nugget size, the welding current was adjusted to achieve a

nugget diameter similar to that obtained with F1-5.5. The results of this validation experiment, shown in Figure 6-33, indicate that increasing the electrode cap's working area completely prevents LME crack formation.
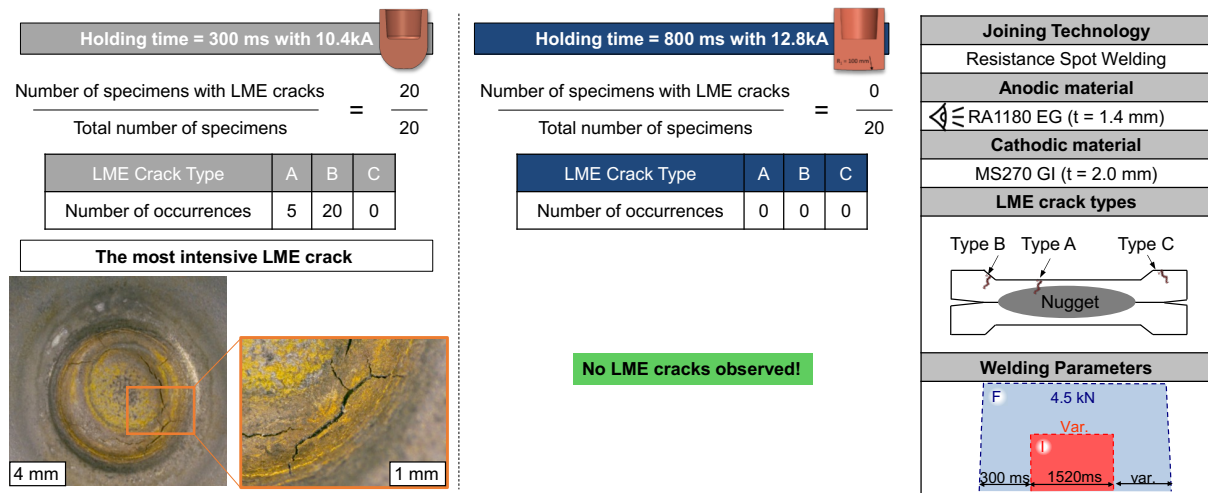

Figure 6-33: Validation of the LME avoidance strategy by increasing the working surface area of the electrode cap

The experimental results indicate that the LME avoidance strategies developed in phase 1 of the LME project remain effective. Next, these strategies will be further validated under worst-case conditions in welding experiments on S-Rail components. Following the recommendations of the WorldAutoSteel LME working group, the electrode cap was changed from A0-100 to F1-8 for the experiments validating the LME (liquid metal embrittlement) crack avoidance strategy. This was combined with an extended hold time strategy. To ensure the effectiveness of this avoidance strategy, the welding conditions were set to the worst-case scenario: a 5° electrode misalignment and a welding time four times the standard duration. Additionally, due to the presence of springback, there were significant gaps between the sheets. These stringent conditions aimed to thoroughly test the new strategy under extreme situations that might be encountered in actual production, ensuring its reliability and stability in various scenarios.
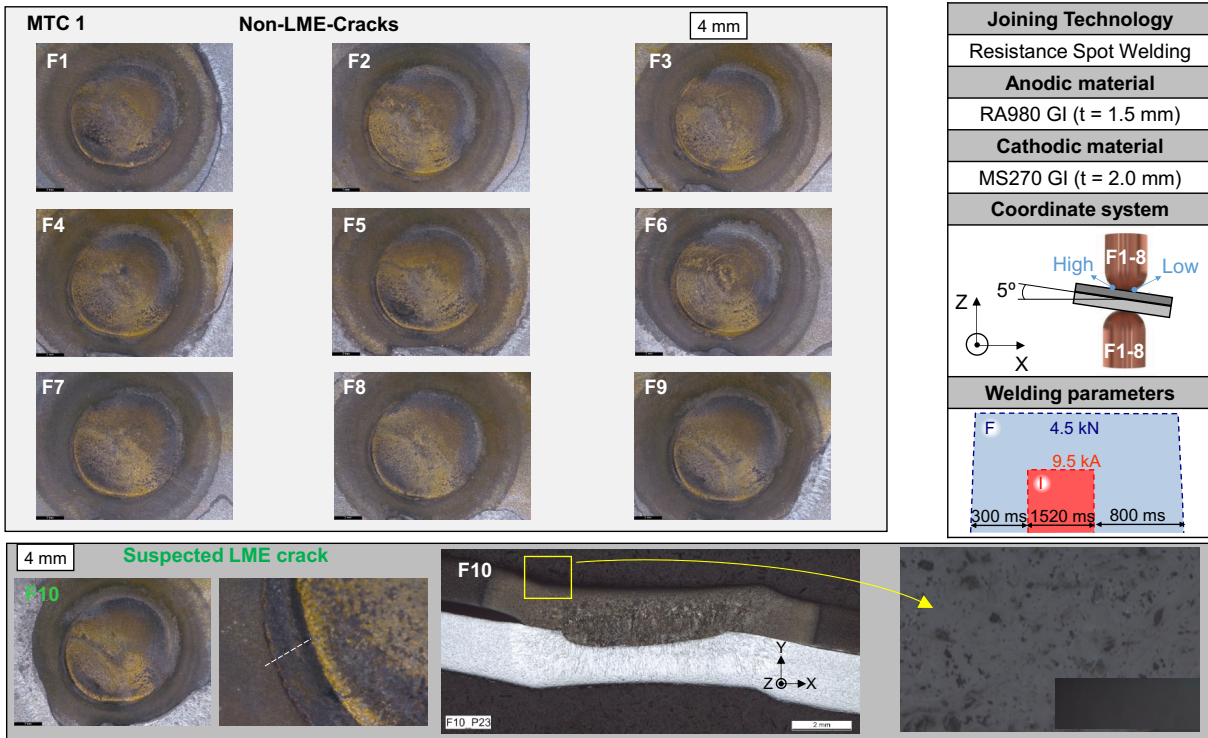
Figure 6-34: validation of LME mitigation strategy on S-Rail component (MTC1)

First, in MTC 1, all spot welds were examined under a microscope for the presence of LME cracks. The results showed no LME cracks in spot welds F1 to F9 (see Figure 6-34). This indicates that the avoidance strategy was successfully applied to these spot welds. However, a suspected C-type LME crack appeared in the heat-affected zone of weld spot F10. To confirm whether this was indeed an LME crack, microsections were prepared along the vertical direction of the suspected crack and closely examined its cross-section. The results showed that the crack depth did not exceed 100 µm, confirming that it was not an LME crack but possibly another form of microcrack or surface defect.

MTC 2	Non-LME-Cracks			
F1	F2	F3	F4	F5
F6	F7	F8	F9	F10

Joining Technology
Resistance Spot Welding
Anodic material
RA1180 EG (t = 1.4 mm)
Cathodic material
RA1180 EG (t = 1.4 mm)
Welding parameters
F 4.5 kN
8.7 kA
300 ms 1520 ms 800 ms

MTC 6	Non-LME-Cracks			
F1	F2	F3	F4	F5
F6	F7	F8	F9	F10

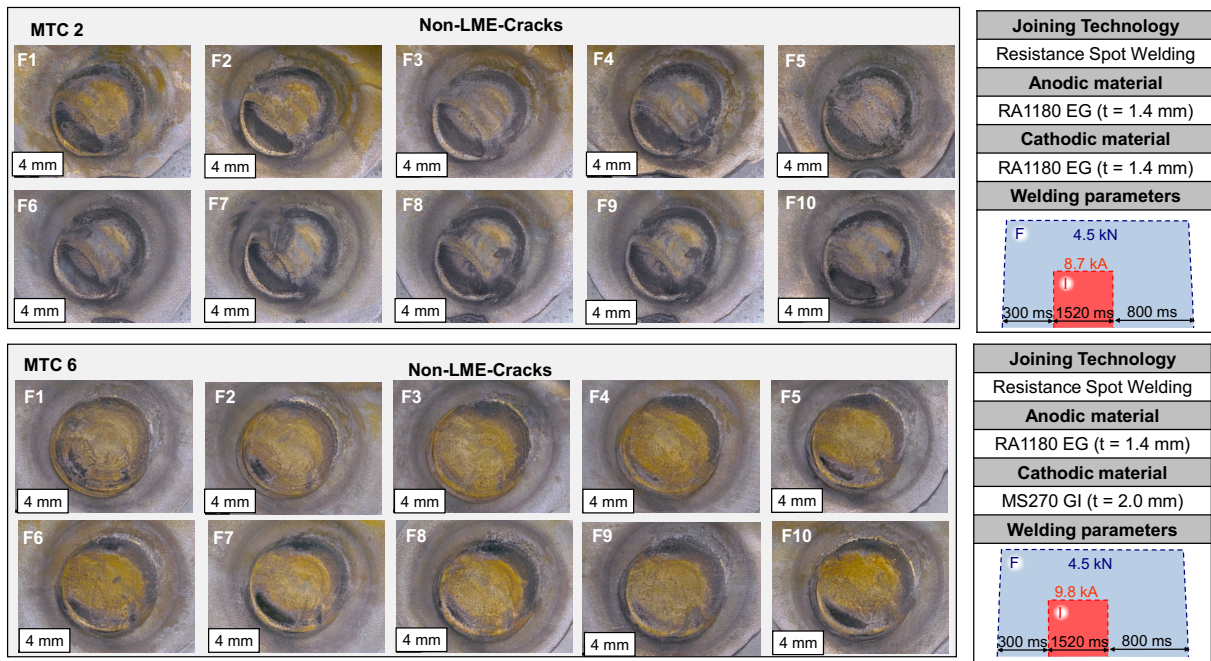| Joining Technology |
|---|
| Resistance Spot Welding |
| **Anodic material** |
| RA1180 EG (t = 1.4 mm) |
| **Cathodic material** |
| MS270 GI (t = 2.0 mm) |
| **Welding parameters** |
| F 4.5 kN |
| 9.8 kA |
| 300 ms 1520 ms 800 ms |

Figure 6-35: LME mitigation method evaluation on the S-Rail geometry (MTC2 and MTC6)

Figure 6-35 further demonstrates the successful application of the new method. In MTC 2, microscopic examination revealed no LME cracks in spot welds F1 to F10. This result further validates the effectiveness and reliability of the new electrode cap and extended hold time strategy under different materials and welding parameters.

Finally, the validation experiments conducted in MTC 6 further support these findings. All spot welds (F1 to F10) showed no occurrence of LME cracks when using the avoidance strategy. This further illustrates the universality and stability of the new strategy, indicating that it can effectively prevent LME cracks under any condition. The conclusion drawn from these experimental results is that this avoidance strategy successfully prevents LME cracks under various material test conditions, even in the worst-case scenarios.

6.3.2   Simulation of Extended Hold Times

Increased hold times, i.e. an increase in the time the electrodes are in contact with the workpiece after welding, generally decrease LME susceptibility [6]. This is attributed to the additional cooling effects of the water-cooled copper electrodes, which, in turn, leads to shortened availability of liquid Zinc on the surface. In order to evaluate the

applicability of this LME mitigation measure, welds were conducted on the S-Rail with increased hold times.

Figure 6-36 shows plots of the stress-based LME criterion over time for spots 3 and 8 in comparison with 200 ms (blue) and 800 ms (black) hold time. It is clearly visible, that for increased hold times, the criterion drops to Zero much faster because the surface cools below 420°C more quickly and all surface temperatures below 420°C led to no criterion value as per Equation (2). Therefore, the criterion yields a lowered response for a process parametrization that causes far reduced LME susceptibility. It can also be observed, however, that the maximum value of the criterion remains nearly the same for 200 ms and 800 ms hold times. For this parameter set, the maximum value of the criterion occurs while the electrode is still in contact even for the 200 ms case. Hence, the weld has not changed yet, and the maximum value is similar for both parameter sets.
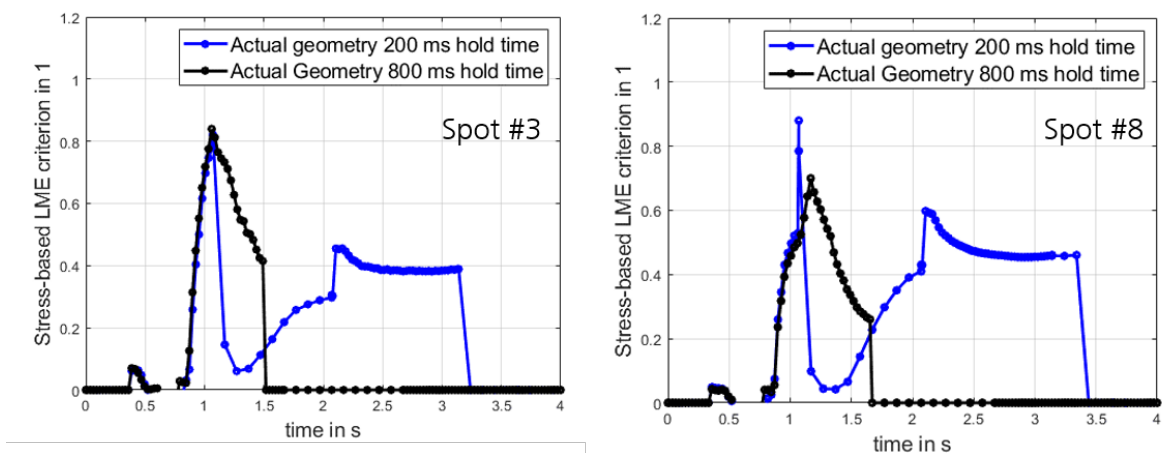

Figure 6-36: Stress-based LME criterion over time plot for 200 ms and 800 ms hold time

In Figure 6-37, the peak stress-based LME criterion is plotted for all 10 spots in comparison between 200 ms and 800 ms hold times. Even though the experimentally observed crack occurrence is much lower, the peak criterion responses are similar for extended hold times, leading to the question of the suitability of this evaluation method.
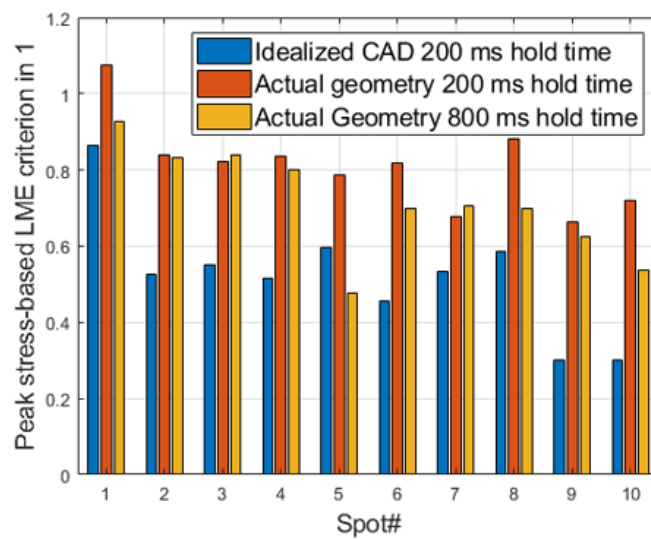
Figure 6-37: Peak stress-based LME criterion in comparison for elongated hold times

Figure 6-36 shows a significantly shortened criterion response for an increase in hold time. Following this investigation, the area underneath the curve is used for comparison rather than the maximum value. This is formalized in Equation (3) and plotted in Figure 6-38. In this graph, a markedly lowered "integrated criterion response" is visible for the extended hold time parametrization. In fact, the criterion suggests that the LME risk is even lower as compared to the idealized CAD case and therefore fully mitigates the additional LME risk stemming from welding on a springback-afflicted part. With this approach, process-parameter-specific hold times can be derived by comparing the criterion response and determining the hold time where no additional reduction of the LME criterion occurs.
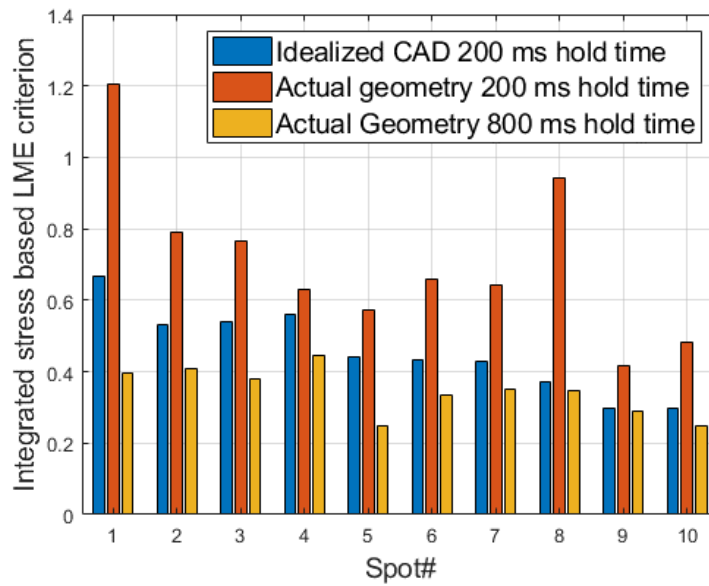
Figure 6-38: Integrated stress-based LME criterion for elongated hold times

Integrating the LME criterion is identified as a promising way to use the criterion for comparison of different parameters. It is therefore explored further in the remainder of the work.

6.3.3   Simulation of Larger Electrode Caps

A second mitigation measure for LME occurrence is the use of electrode caps with larger working planes. It was found that increased electrode cap working diameters decrease the electrode sink-in and cause less LME formation [3]. Figure 6-39 shows a comparison of the average electrode sink-in velocity according to Equation (1) for 5.5 mm and 8 mm diameter electrode caps. As noted in previous work, the electrode sink-in velocity is significantly reduced by increasing the electrode cap diameter. This criterion gives a good estimation of reduced LME sensitivity of the welds, it is, however, not well-defined for springback-afflicted geometries or tilted weld-guns.
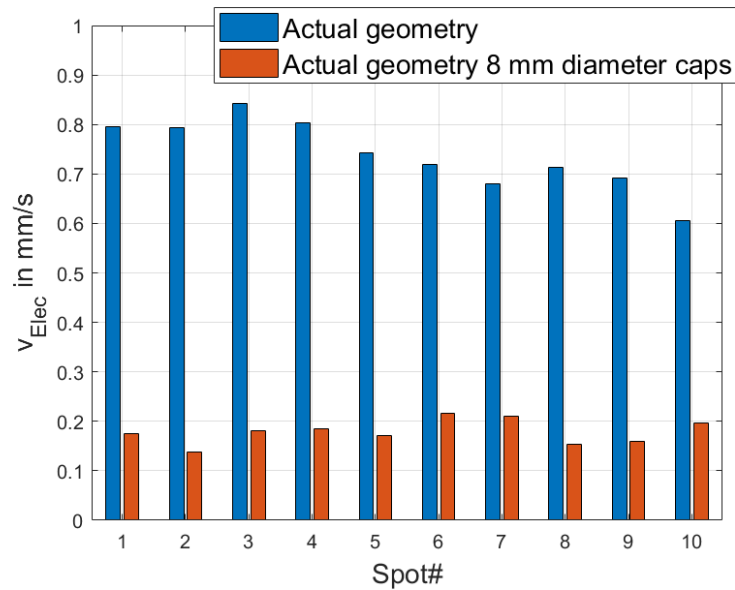
Figure 6-39:   Average electrode sink in velocity for all 10 spots in comparison with 5.5 mm and 8 mm working plane diameter electrode caps

The integrated stress-based LME criterion according to equation (3) has a broader definition and is fully applicable for process- and geometric deviations. The results of this criterion are shown for all 10 spots in Figure 6-40. The increased electrode cap diameter lowers the criterion response in comparison to the original diameter but does not reach the same level of effectiveness as the increased hold time.

This may be different with different material thickness combinations as well as different welding parameters. The criterion allows for comparisons in the efficiency of mitigation measures as well as the LME-risk of parameter sets.
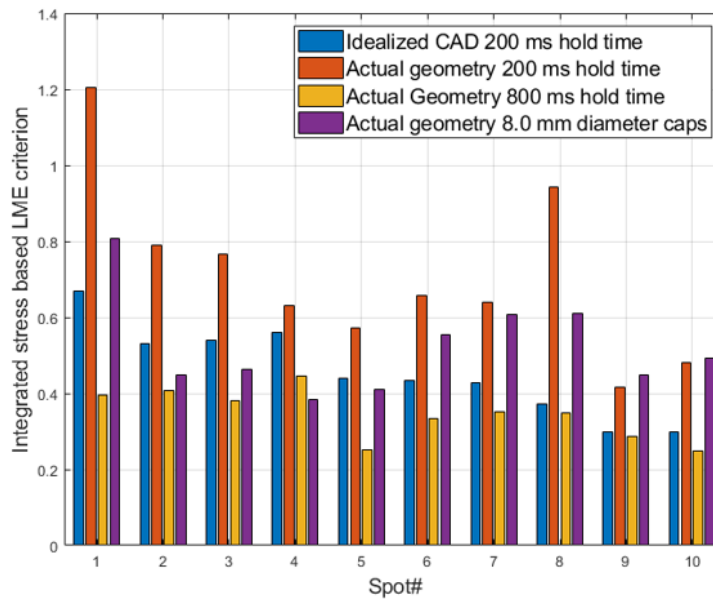
Figure 6-40:   Comparison of the integrated stress-based LME criterion for elongated hold time and larger diameter working plane mitigation strategies

6.3.4   Combination of Hold Time and Larger Electrode Cap

It is also possible to combine an increased hold time with a larger electrode working plane. This theoretically results in the lowest LME susceptibility. With the comparison of the criterion response in Figure 6-41 for spots 4 to 6, it is visible that the combination of mitigation strategies does not reduce the LME susceptibility further. For the investigated material thickness combination and parameter set, it is therefore not necessary to combine mitigation strategies; Increasing the hold time is sufficient to reach a significantly lowered LME risk. It needs to be noted here that in order to create sufficient amounts of LME cracks for investigation, the welding time was doubled. Hence, a large amount of additional energy is introduced into the weld, making a mitigation strategy with additional energy reduction particularly effective. It is expected that the mitigation strategies show different effectiveness on standard parameter sets.
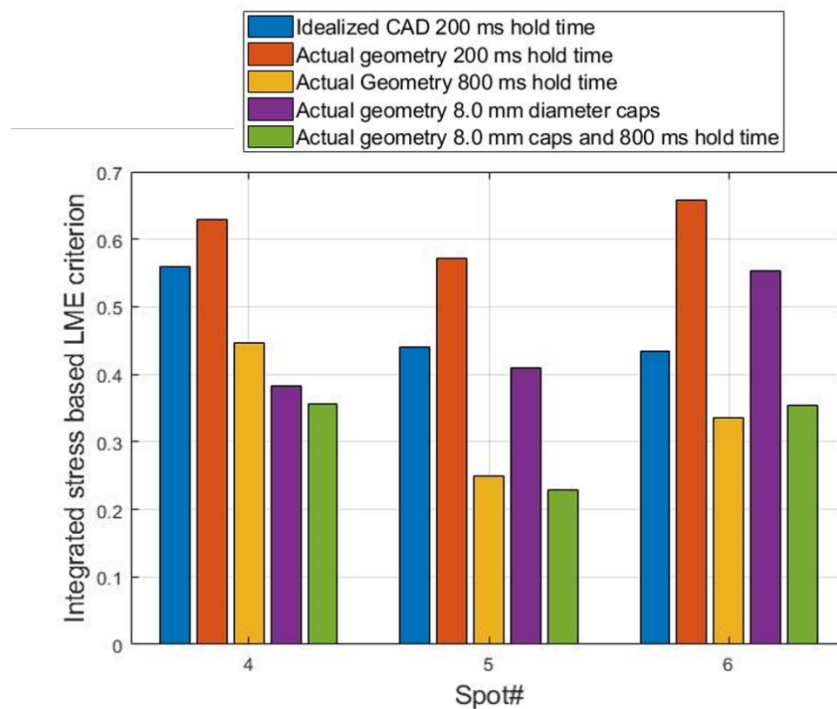
Figure 6-41: Criterion response for the combination of mitigation strategies

6.3.5   Mitigation Strategies for Different MTCs

Using the same integrated stress-based LME criterion, different material stack-ups can be compared. MTC2 and MTC6 are especially relevant for a comparison in the scope of this work because they both use the same top sheet AHSS but a different joining partner. For MTC2, the joining partner is the same 1180 MPA high ductility dual phase steel, for MTC6, the joining partner is a 2 mm deep drawing steel. MTC2 shows no LME susceptibility whereas MTC6 exhibits marked LME formation.

The results of the integrated stress-based LME criterion for MTC2 and MTC6 together with the mitigation measure of extended hold times are plotted in Figure 6-42. It is visible that MTC2 has an overall smaller LME susceptibility. The criterion value is, in fact, roughly the same as for MTC6 with extended hold time. With extended hold time in MTC2, the criterion value sinks further but as there are already no cracks for 200 ms hold time, a use of further mitigation strategies is not necessary.
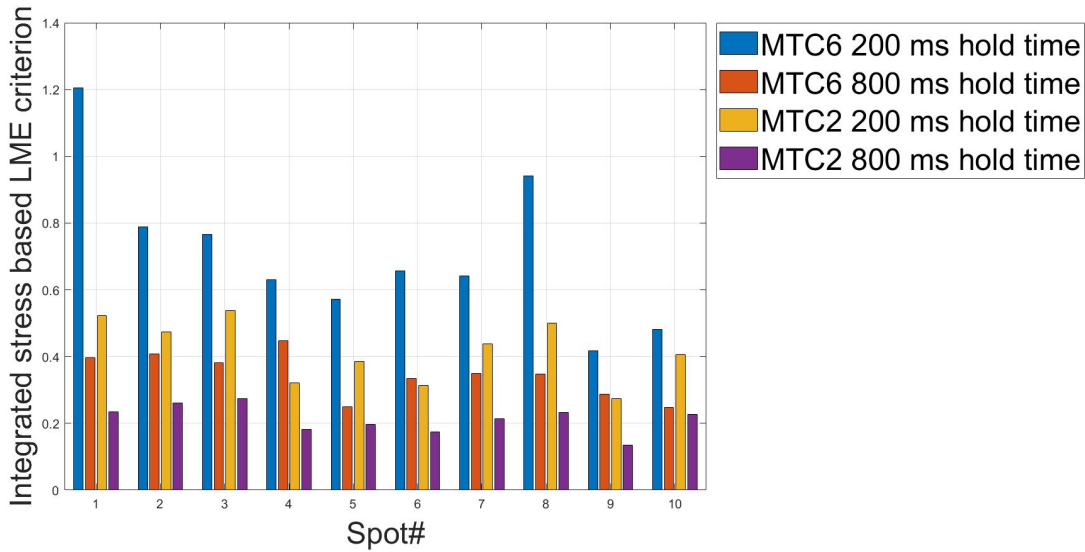
Figure 6-42: Comparison of different material stack ups with the stress-based LME criterion

6.4   Crash Testing

6.4.1   Crash Test Setup

Due to the complex and asymmetric geometry of S-Rail components, traditional impact testing methods, as shown in Figure 6-43, result in bending at the S-Rail curve. This prevents defined and repeatable loading of weld spots. To ensure the reliability of crash test results, this project developed a special crash test method tailored for S-Rail components.
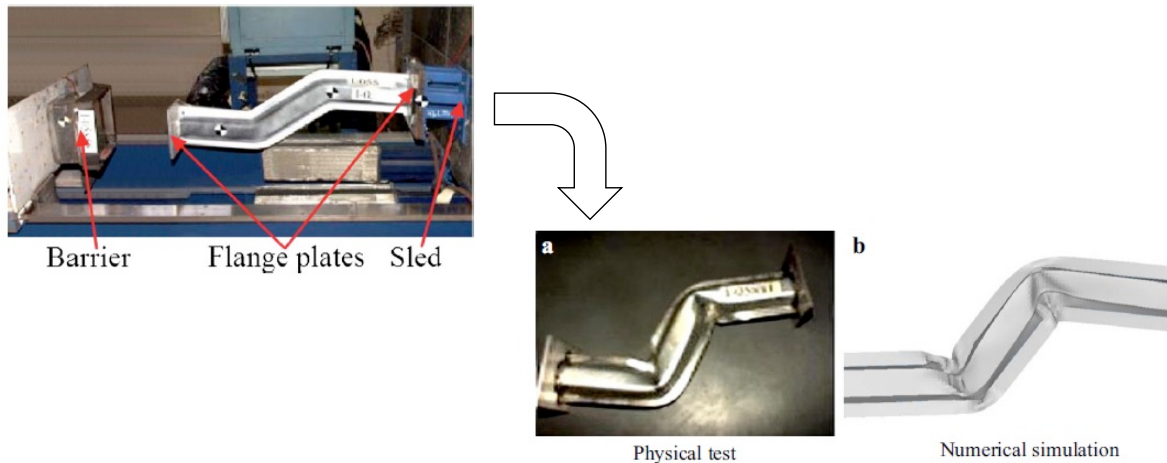
Figure 6-43: Initial condition analysis of the load-bearing capacity test of the S-Rail

As the basis for developing the new crash test, the critical load direction for LME cracks was first investigated. LWF-KS-II samples were tested for single-point load-bearing capacity under quasi-static and impact loads in different load directions. To generate sufficiently strong LME cracks, AHSS with a proven high LME sensitivity and strength of 1200MPa was used. Similar to MTC1 and MTC6, mild steel was used for the bottom sheet.

Figure 6-44 shows the results of load-bearing capacity tests under tensile-shear load (0° load direction). Even with significant C-type cracks on the AHSS side, the spot weld failure mode in three repeated experiments was still pull-out failure on the mild steel side. This indicates that, under tensile-shear stress, LME cracks in the AHSS are not sufficiently loaded, making it impossible to assess whether LME cracks affect joint load-bearing capacity. Thus, this load mode is not effective for studying the impact of LME on load capacity.
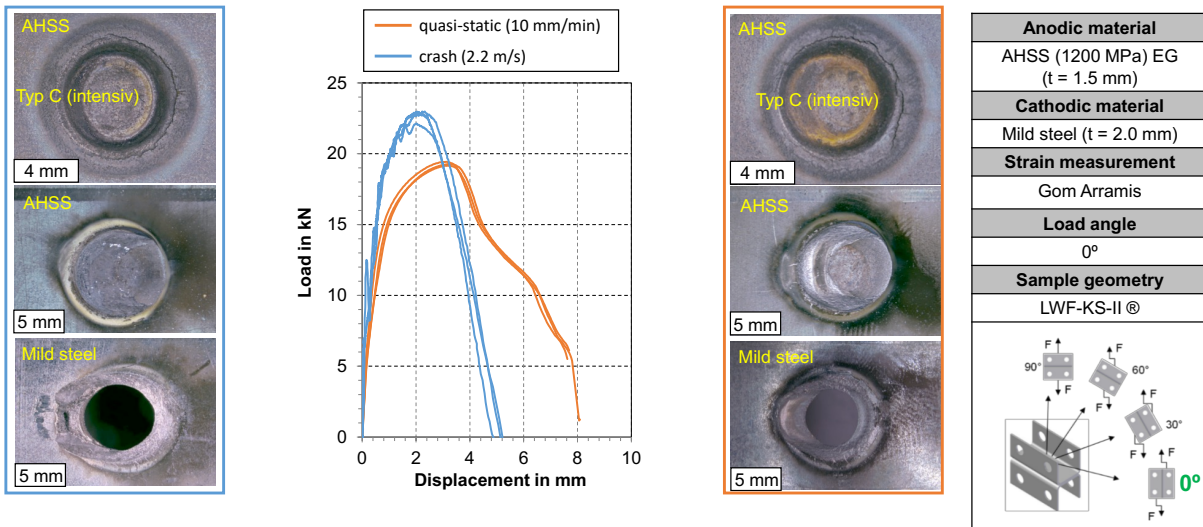
Figure 6-44:   Determination of the effective loading method for LME cracking (under tensile shear load)

In the subsequent tensile load tests (90° load direction), all samples failed along the LME cracks on the AHSS side (see Figure 6-45). The failure mode is pull-out failure. This result confirmed that cross-tensile loading is a more suitable method for evaluating the impact of LME.
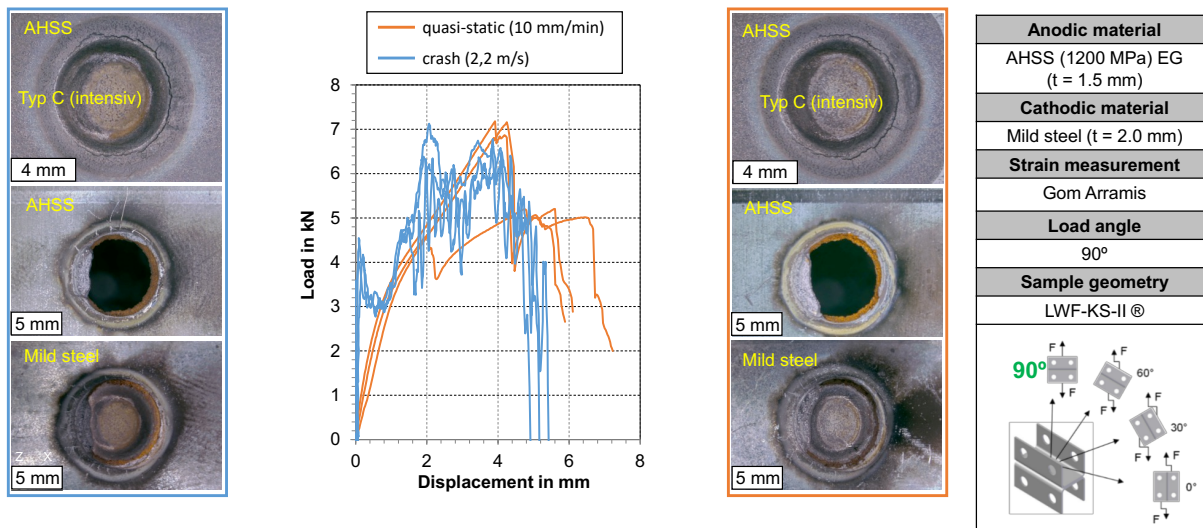

Figure 6-45:   Determination of the effective loading method for LME cracking (under tensile load)

Finally, peel load was investigated because it combines tensile-shear and cross-tensile loads, providing a load mode closer to actual crash conditions, as shown in Figure 6-46. Under peel stress, repeatable pull-out failure was observed along LME cracks on the

high-strength steel side under static load. Under impact load, two out of three repeated tests showed this effect, but the last test showed pull-out failure on the mild steel side. This discrepancy may be due to the corresponding LME crack strength. However, this also indicates that if LME were to significantly affect load capacity, joint failure would manifest as pull-out failure along LME cracks on the AHSS side.
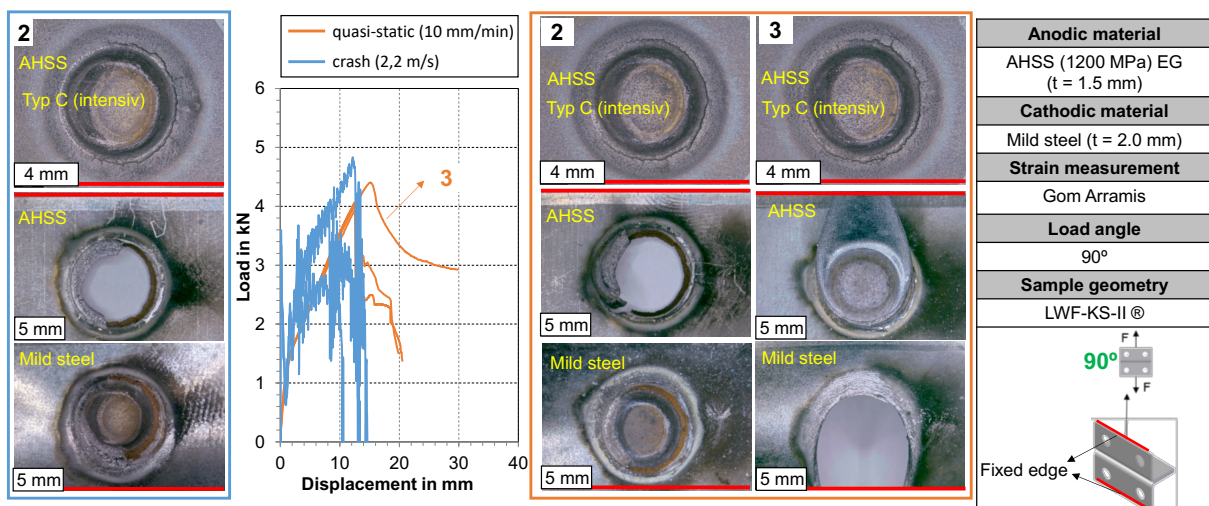

Figure 6-46: Determine the effective loading method for LME cracking (under peel load)

Based on these results, a test method was developed using hat profiles, as shown in Figure 6-47, built upon three-point bending tests. Before the welding experiments, a window was cut in the middle of the hat profile, which was then joined to the bottom sheet through flange weld spots. During the final test, a punch contacts the bottom sheet through this window, applying load to the bottom sheet. The connection between the bottom sheet and the hat profile causes plastic deformation along the load direction, applying a defined load to the flange weld spots. This method induces vertical downward pull-out stress and horizontal inward tensile-shear stress along the hat profile. These combined stresses have been proven in preliminary tests to be effective peel stress for LME cracks.
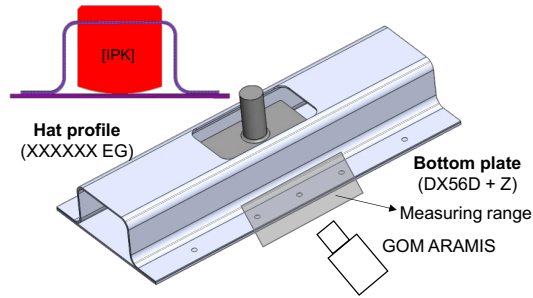
Figure 6-47: Schematic representation of the developed test method based on H-profile

To visualize the loading conditions on the weld spot surface, the optical 3D deformation analysis system GOM ARAMIS 4M (GOM GmbH) was used to record surface strain. This means that if the test method is effective, the weld spot surface should exhibit the highest strain. If the LME crack strength on the AHSS surface is significant enough to affect joint strength, pull-out failure on the AHSS side should be observed.
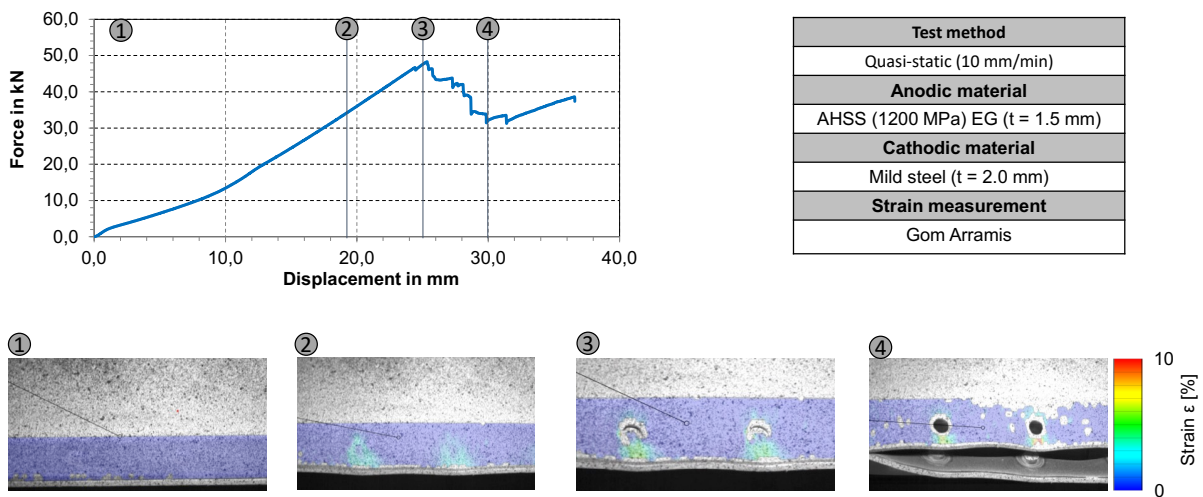

Test method
Quasi-static (10 mm/min)
Anodic material
AHSS (1200 MPa) EG (t = 1.5 mm)
Cathodic material
Mild steel (t = 2.0 mm)
Strain measurement
Gom Arramis

Figure 6-48: Force-displacement curve and local stress measurement using GOM ARAMIS from the validation test

This test method was then experimentally validated under quasi-static load (10mm/min), as shown in Figure 6-48. In stages 1 to 3, the load increased with punch displacement but at a relatively slow rate, corresponding to the plastic deformation behavior of the bottom sheet. After 10 mm, the load increased more rapidly, reflected by a steeper slope on the curve. Analyzing the strain on the weld spot surface in stage 2 concluded that significant strain appeared only around the weld spot. After stage 3, the curve showed intermittent sudden drops, corresponding to the failure of weld spots

on the flange of the hat profile, confirmed by GOM ARAMIS records. By stage 4, all weld spots on the flange of the hat profile had failed. This validates the previous analysis and demonstrates that this test method can effectively and definitively load the flange weld spots. This method will be applied to the subsequent load capacity testing of S-Rail components, as shown in Figure 6-49. Further analysis of the optimal clamping method and punch size will be conducted in section 6.4.2.
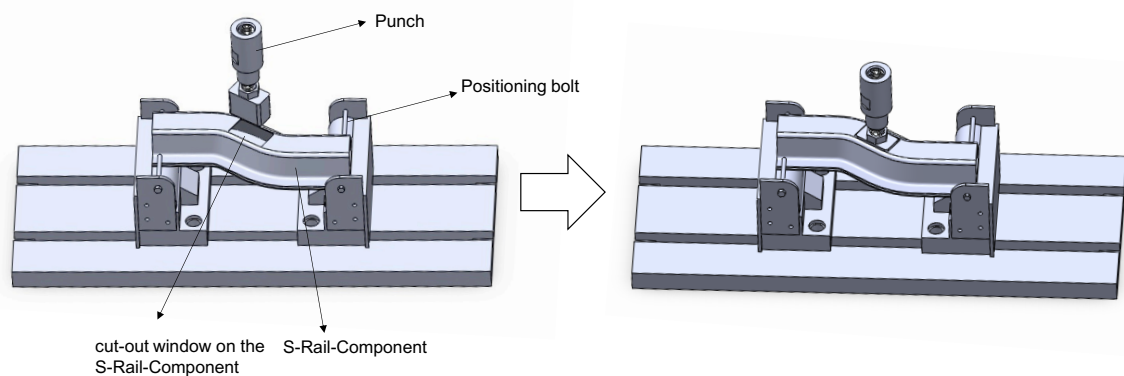

Figure 6-49: Test rig setup for S-Rail-component

6.4.2 Crash Test Design by Simulation

In order to dimension the crash test setups, accompanying simulations were conducted. In the first simulation, two different indenter shapes were compared (Figure 6-50) with quasi-static indentation velocities.
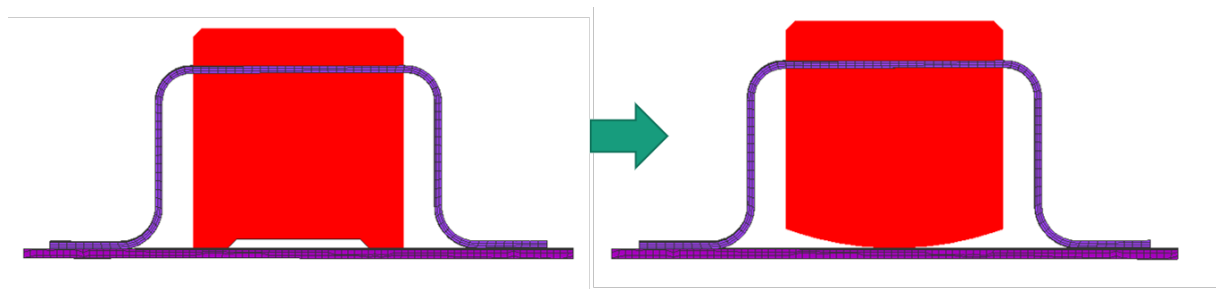

Figure 6-50: The two different indenter shapes compared in the simulation

Figure 6-51shows a result for the rounded indenter. This shape was determined to be beneficial because it loads the bottom sheet equally and transfers the forces directly onto the resistance spot weld. The forked indenter creates local stress concentrations at the contact locations between the indenter and the bottom sheet, increasing the risk

of punching through the bottom sheet, which reduces the impact energy transferring to the resistance spot welds.
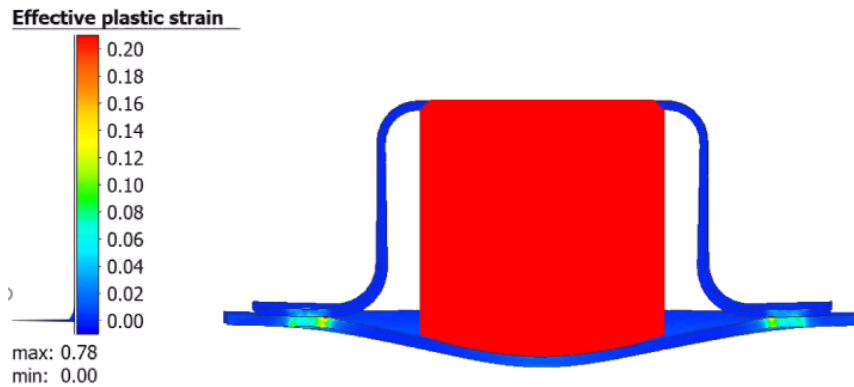

Figure 6-51: Simulation results for the rounded indenter

The second simulation was used to test the clamping location for the S-Rail. Option 1 comprises clamping at the top section of the S-Rail, option 2 consists of a bearing-type fixture underneath the bottom sheet. Both options are shown in Figure 6-52.
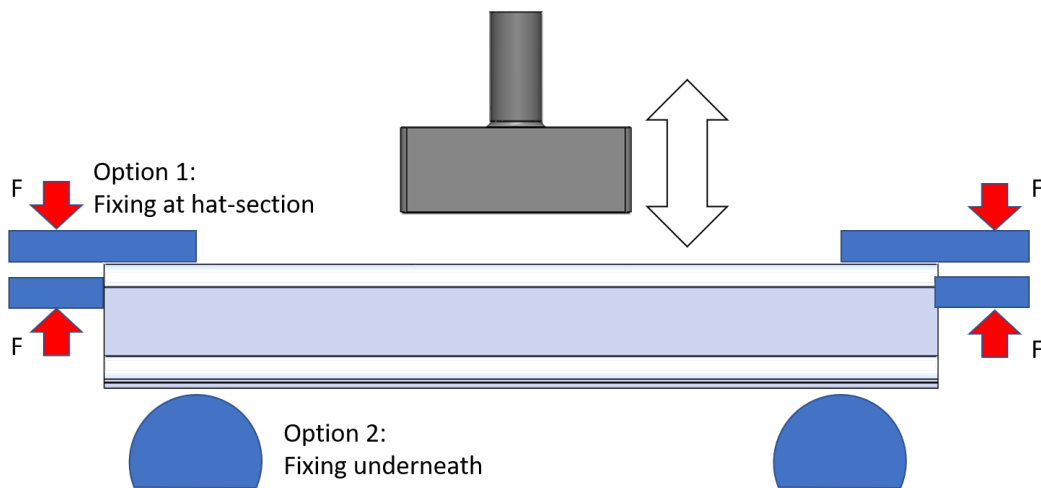

Figure 6-52: Two different clamping options for the crash test

Both cases were simulated using the crash-velocities from the experimental setup. The z-normal stress in the joining zone of the three center-lying weld nuggets was extracted and compared. The results are shown in Figure 6-53. The upper clamping (option 1)

leads to a slightly quicker rise in forces in the resistance spot weld. Option 2 ultimately causes the higher loading of the weld and is recommended for the experimental setup.
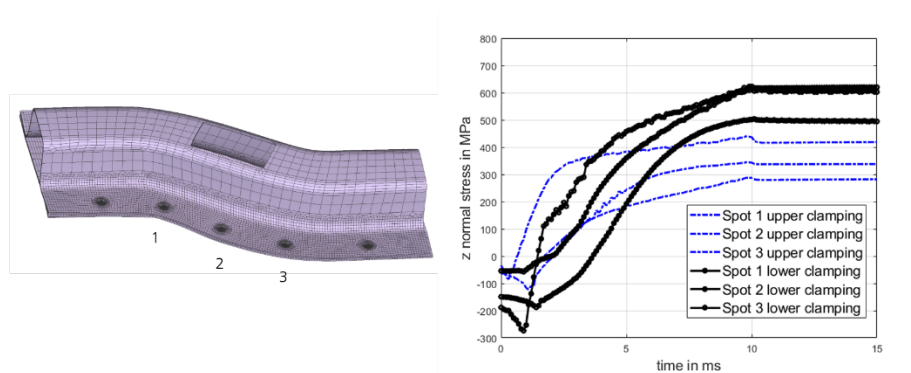

Figure 6-53: Loading of the three center-most spot welds with two different clamping conditions

6.4.3 Crash Test Results

The experimental setup was established as shown in Figure 6-54. The punch was accelerated pneumatically, with different test speeds achieved by adjusting the valve opening. A punch slightly smaller than the window cut into the S-Rail component was used at the front. The S-Rail component was securely fixed using clamping equipment. During the tests, a high-speed camera recorded the weld spots from above.

1. High-speed camera
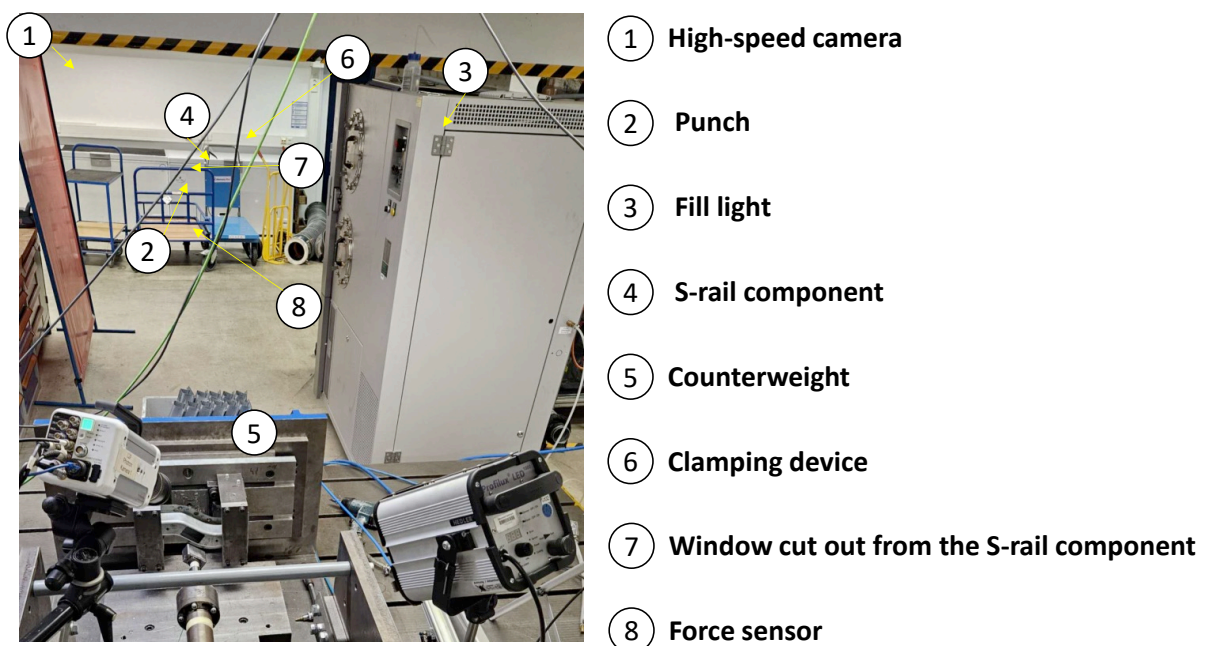2. Punch
3. Fill light
4. S-rail component
5. Counterweight
6. Clamping device
7. Window cut out from the S-rail component
8. Force sensor

Figure 6-54: Experimental setup for the crash test

© Copyright 2024 – WorldAutoSteel, LWF, Fraunhofer IPK

Before starting the crash test, the newly developed test method was validated. Figure 6-55 (a) shows the validation results for MTC1, where it was observed that the fixation effect of the weld spots on the concave and convex sides (F2, F4, F7, and F9) caused the load to be overly concentrated near the cut window. This resulted in significant bending along the X-axis due to the non-collinearity of the S-Rail component's sample size, with the cut window deforming severely, almost into a diamond shape. This deformation absorbed most of the kinetic energy, hindering further loading of the weld spots, and even at progressively higher test speeds, no weld spot failure was observed. Additionally, bending of the S-Rail component along the Z-axis further absorbed energy. Consequently, no weld spot failures were observed as the test speed increased from 2.1 m/s to 3.6 m/s.
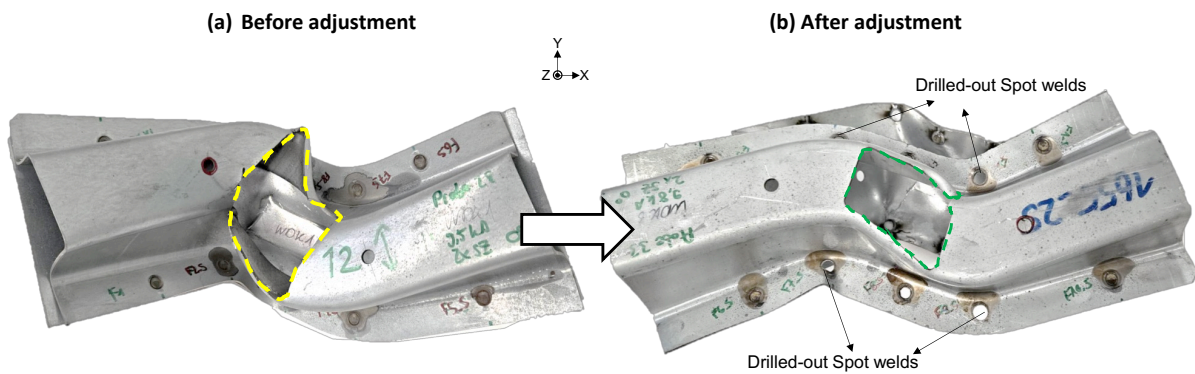

Figure 6-55:   Comparison of the failure modes of S-Rail components before (a) and after (b) adjustment.

To mitigate the impact of the S-Rail component's unique dimensions on the crash test, the following adjustments were made: for the welded S-Rail components, the weld spots at F2, F4, F7, and F9 were drilled out in each sample. Only the weld spots in the central flange area of the S-Rail component were retained to prevent excessive deformation. After this adjustment, as shown in Figure 6-55 (b), this ensures that there is no longer weld spot failure in the non-collinear bending areas of the S-Rail component. Consequently, it eliminates additional deformation in these regions, ultimately reducing the overall deformation of the S-Rail component during the crash test. The set kinetic energy was maximally utilized for loading the weld spots, effectively leading to weld spot failure. Therefore, subsequent experiments will continue using this adjusted test method.

Following the adjustments to the testing method, crash tests were conducted on all samples, with MTC1 tested at a speed of 3.1 m/s and MTC6 at 3.6 m/s. The force-displacement graphs for all crash tests are summarized in Figure 6-56. The welding parameters used here are the same as those in section 6.2.1. Taking the standard component of MTC1 as an example, contact between the punch and the bottom sheet, followed by subsequent plastic deformation, caused the displacement to increase gradually up to about 37 mm. The curve then descended, indicating the onset of spot weld failure. As the curve continued to drop, two subsequent segments of sharp fluctuations represented the complete failure of the two weld spots retained in the central area of the S-Rail component.
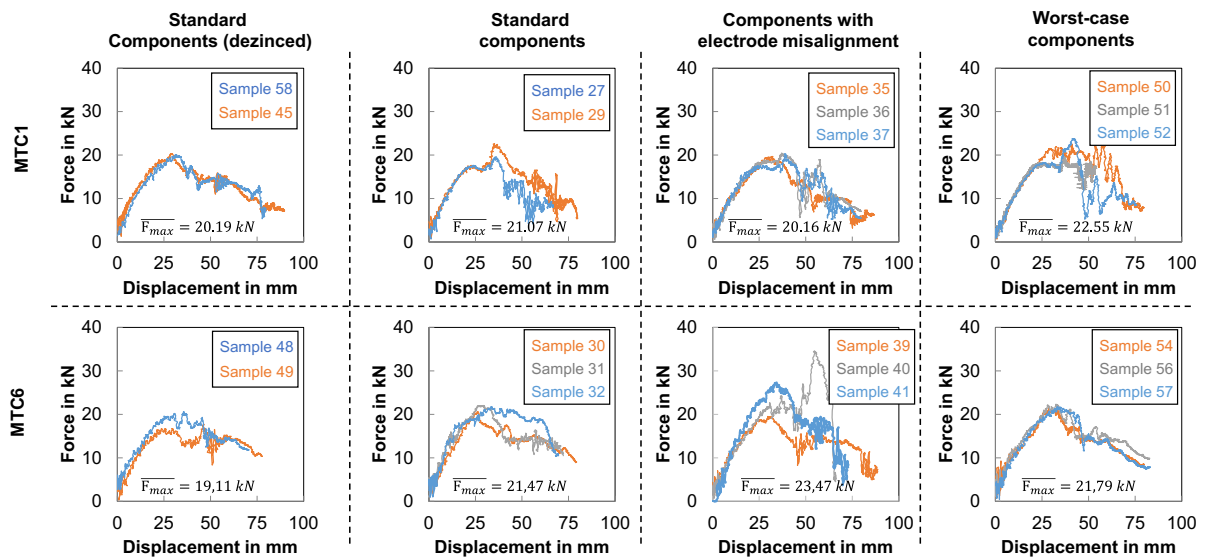

Figure 6-56: Overview of the force-displacement curves of the tested series

Comparing the force-displacement curves of different welding boundary conditions within the same MTC reveals that the presence of LME cracks did not significantly affect the average F_{max} value (where F_{max} refers to the maximum load sustained before weld spot failure begins). Therefore, to further analyze the impact of LME cracks on joint load capacity, the failure modes of weld spots in each sample will be examined with the help of a high-speed camera. The criterion for assessing whether LME affects the joint's load capacity is whether LME cracks participated in and facilitated the weld spot failure process. The specific criteria are as follows:

- Case 1: If LME cracks are present on the AHSS surface, but the joint fails on the mild steel side, it indicates that LME does not affect the joint's load capacity in this scenario.

- Case 2: If LME cracks are present on the AHSS surface and the joint fails on the AHSS side, but the failure does not follow the existing LME cracks, it indicates that LME cracks did not affect the joint.

- Case 3: If the conditions are the same as in Case 2, but the weld spot failure follows the LME cracks, it indicates that the presence of LME cracks facilitated the weld spot failure (since part of the material surface had already failed due to the cracks). This suggests that LME cracks negatively affect the joint's load capacity.

Standard Component

After completing the crash test, the MTC1 samples were observed and compared with the micrographs taken before the crash test. It was found that the two central weld spots of sample 27 had light A-type LME cracks on the AHSS side (see Figure 6-57). However, after the crash test, the failure mode of these two weld spots was pull-out failure on the mild steel side. Analysis of high-speed camera footage for weld spot F8 also showed significant deformation of the bottom sheet under the punch impact, which pulled the flange weld spot in the load direction but ultimately failed on the mild steel side. Based on the aforementioned criteria, it can be concluded that the light A-type cracks did not affect the joint's load-bearing capacity.
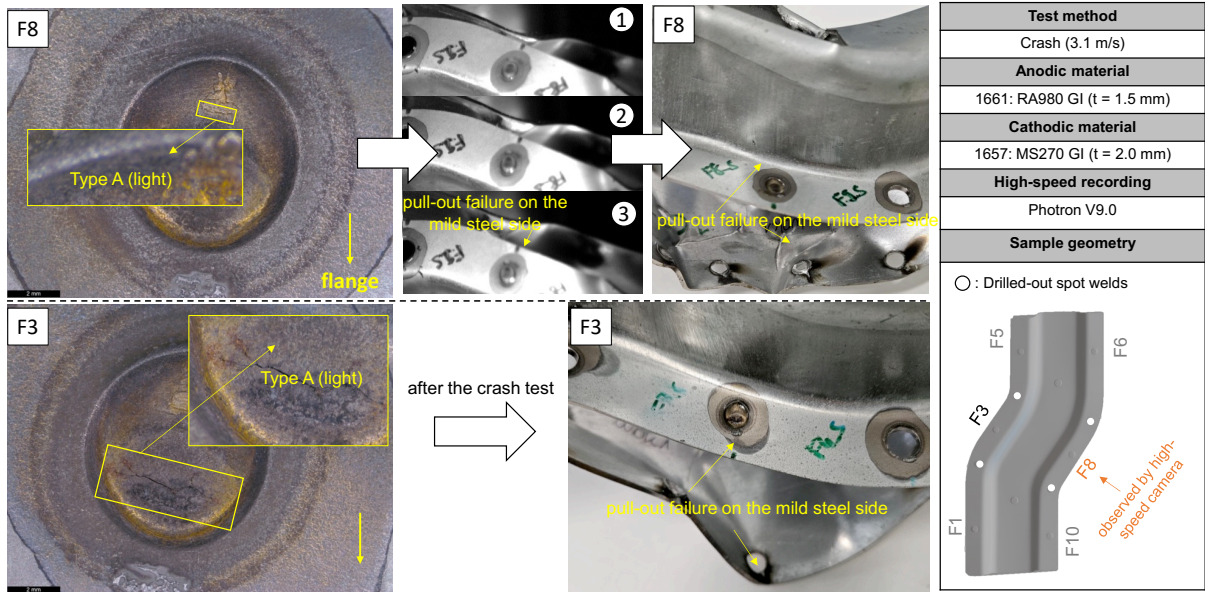
Figure 6-57: Spot weld failure in sample 29 (MTC1)

Similarly, in MTC1, the two central spot welds of sample 29 also exhibited light A-type LME cracks, as shown in Figure 6-58. However, unlike sample 27, weld spot F3 displayed a different failure mode: pull-out failure on the AHSS side. The failure process recorded by the high-speed camera revealed that the weld spot failure was entirely centered around the weld spot. Thus, it can be concluded that the failure on the AHSS side was not caused by the light A-type LME cracks at the center of the spot weld surface.
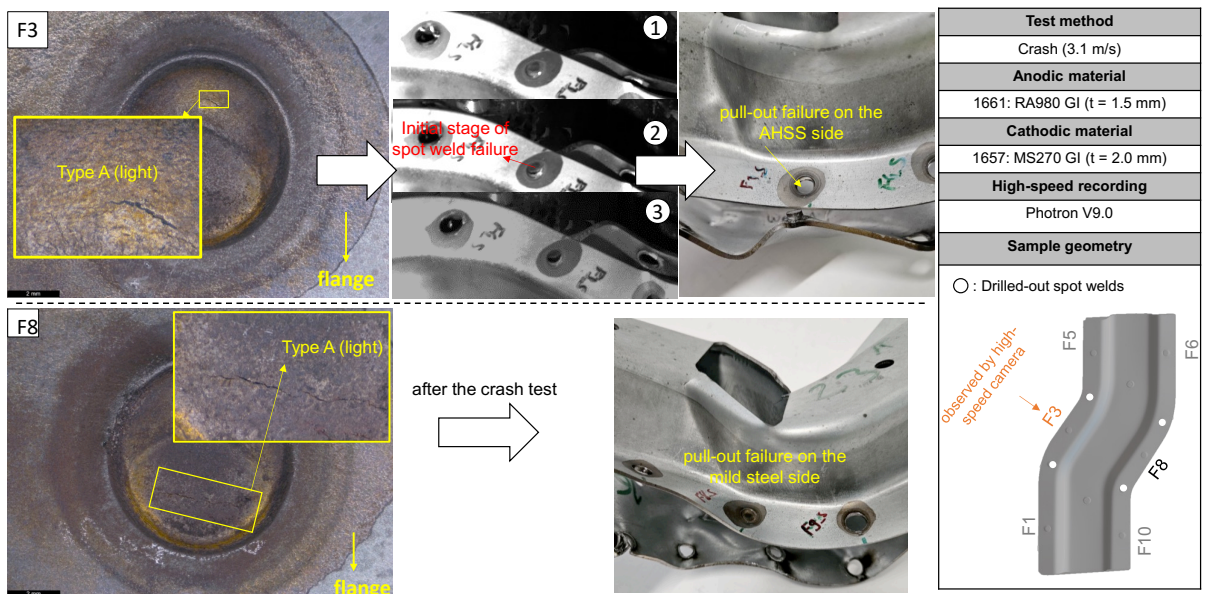

Figure 6-58: Spot weld failure in sample 29 (MTC1)

Compared to MTC1, MTC6 did not exhibit LME cracks under standard welding conditions. The failure modes were partial pull-out failure on the mild steel side for samples 30 and 32, and pull-out failure on the AHSS side for sample 31. Taking sample 31 as an example, see Figure 6-59.
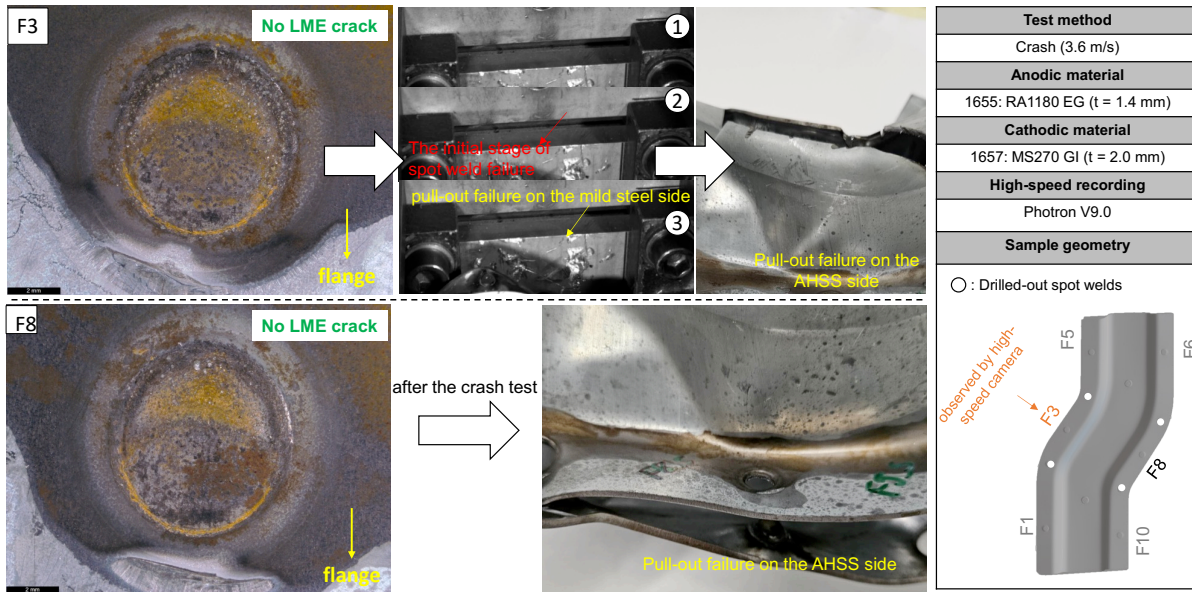

Figure 6-59: Spot weld failure in sample 31 (MTC6)

Electrode misalignment

Under the disturbance of electrode misalignment, the failure modes of the spot welds in MTC1 were further investigated. As shown in Figure 6-60 although spot weld F8 of sample 35 exhibited light B-type LME cracks and partial pull-out failure on the AHSS side, there was no failure in the lower-left area where the crack appeared. Similarly, spot welds in samples 36 and 37 (with sample 37 as an example) also exhibited light B-type LME cracks, but their failure modes were consistent, showing pull-out failure on the mild steel side. Based on these results and the analysis of the force and displacement curves shown in the figure, it can be concluded that light B-type cracks do not affect the joint's load-bearing capacity.
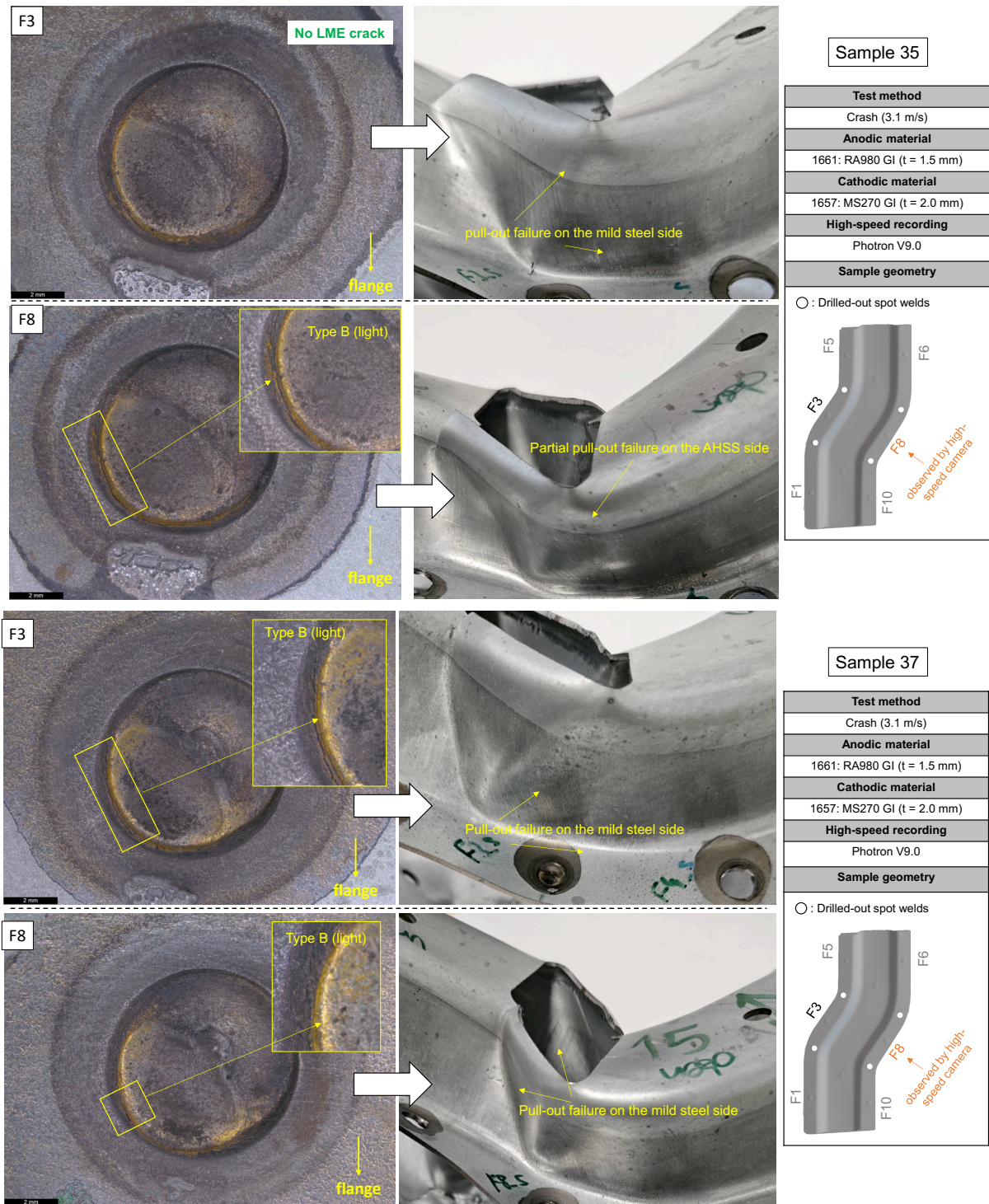
Figure 6-60: Spot weld failure in sample 35 and 37 (MTC1)

Subsequently, the failure modes of the spot welds in MTC6 were further investigated, as shown in Figure 6-61. In sample 39, spot weld F3 exhibited light A-type LME cracks and pull-out failure on the AHSS side. High-speed camera footage showed that the failure occurred entirely around the spot weld, indicating that the light A-type cracks did not participate in the failure process. Additionally, in the same sample, spot weld

F8 showed light A-type and C-type cracks. However, the failure mode observed in the photographs was partial pull-out failure on the mild steel side. Thus, it can be concluded that light A-type and even light C-type cracks do not affect the joint's load-bearing capacity.
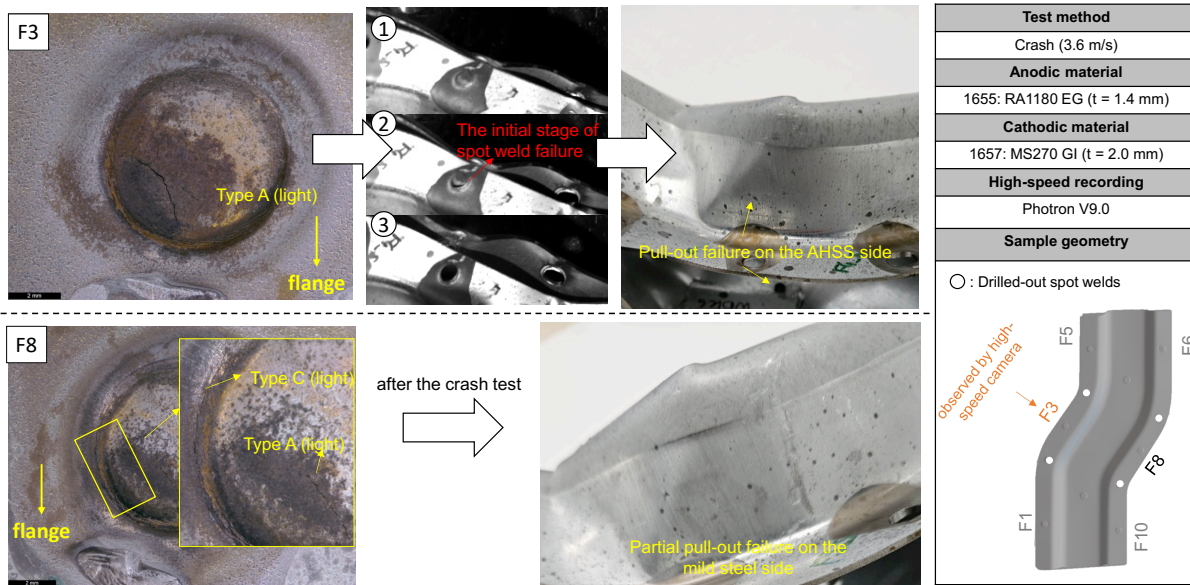

Figure 6-61: Spot weld failure in sample 39 (MTC6)

This conclusion was further confirmed in samples 40 and 41. As shown in Figure 6-62 (with sample 41 as an example), spot weld F3 (with light A-type LME cracks) still exhibited failure on the mild steel side despite the presence of LME cracks.
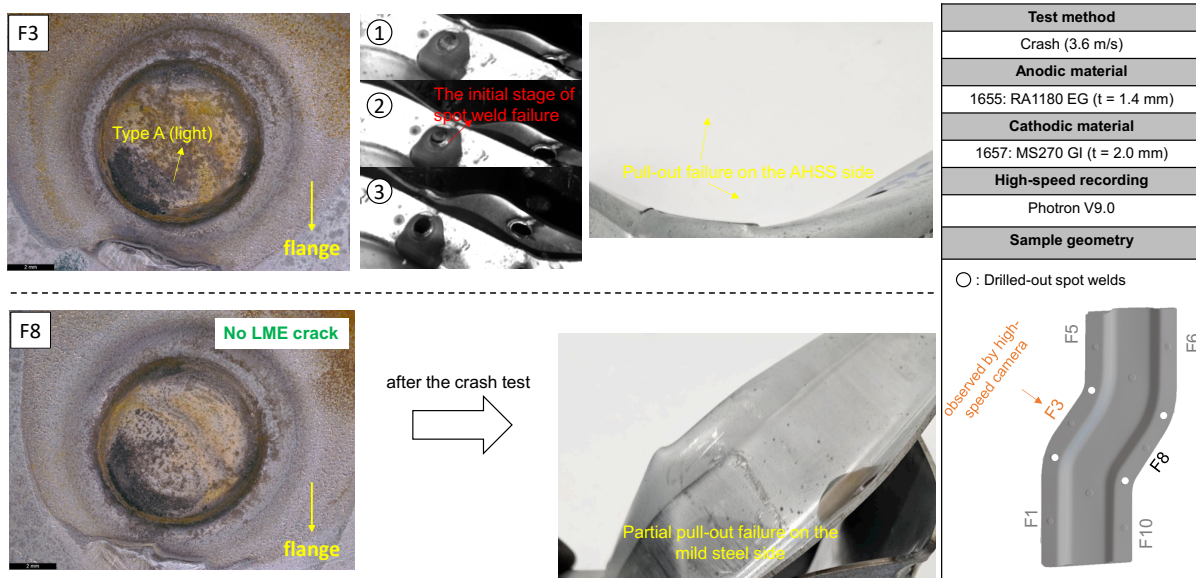
Test method		
Crash (3.6 m/s)		
Anodic material		
1655: RA1180 EG (t = 1.4 mm)		
Cathodic material		
1657: MS270 GI (t = 2.0 mm)		
High-speed recording		
Photron V9.0		
Sample geometry		

Figure 6-62 Spot weld failure in sample 41 (MTC6)

Worst-case components

Finally, under the worst-case conditions of four times the welding duration and a 5° electrode misalignment, crash tests were conducted on MTC1. As shown in Figure 6-63, only light A-type LME cracks were observed in all samples (50 to 52, with samples 51 and 52 as examples). Analyzing the failure modes of the spot welds revealed that all observed spot welds, except for F3 in sample 51, exhibited pull-out failure on the mild steel side, consistent with previous observations. In spot weld F3 of sample 51, pull-out failure was observed on the AHSS side. However, high-speed camera footage analysis indicated that the existing A-type cracks did not participate in the spot weld failure, thus not affecting the joint's load-bearing capacity.
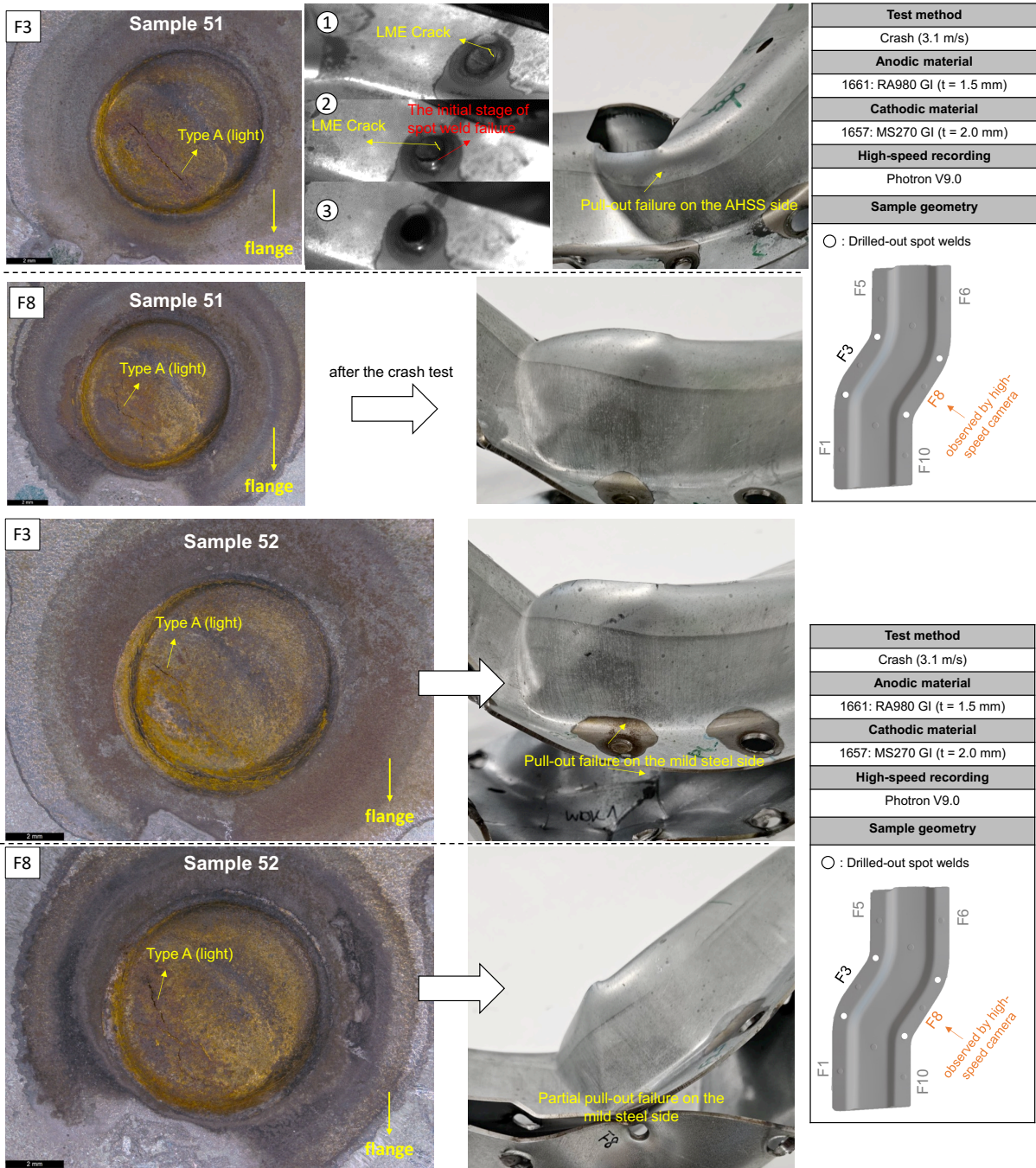
Figure 6-63: Spot weld failure in sample 51 and 52 (MTC1)

The subsequent crash test results for MTC6 support this conclusion. As shown in Figure 6-64(with sample 56 as an example), the samples exhibited light A-type and B-type cracks, but no pull-out failures on the AHSS side were observed.
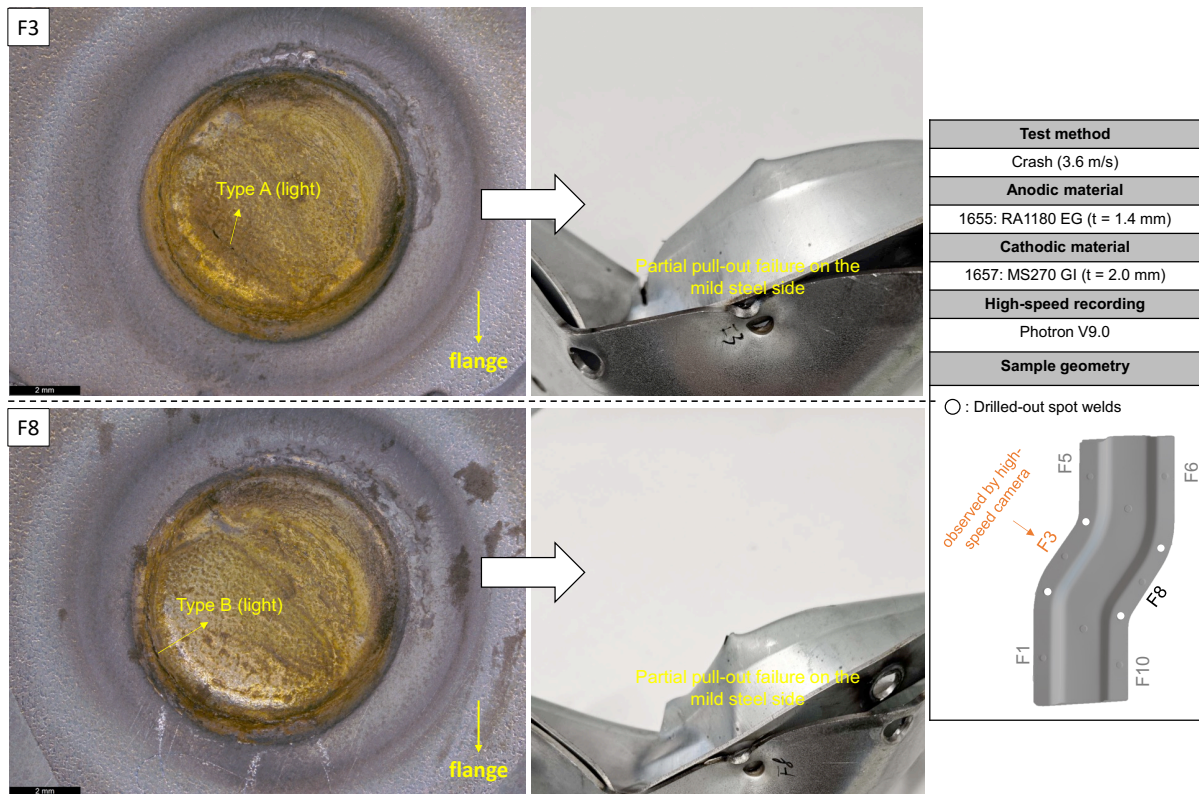
Figure 6-64: Spot weld failure in sample 56 (MTC1)

Summarizing the crash test results, we can conclude that the latest third-generation high-strength steels exhibit generally low sensitivity to LME. Even under conditions that promote the occurrence of LME cracks, the cracks primarily manifest as light cracks, mainly A-type and B-type, with very rare C-type cracks. The tests conducted in this project demonstrate that crack severity does not affect the load-bearing capacity of the joints. Additional samples were made to observe the crack depths corresponding to these levels of severity, as shown in Figure 6-65.
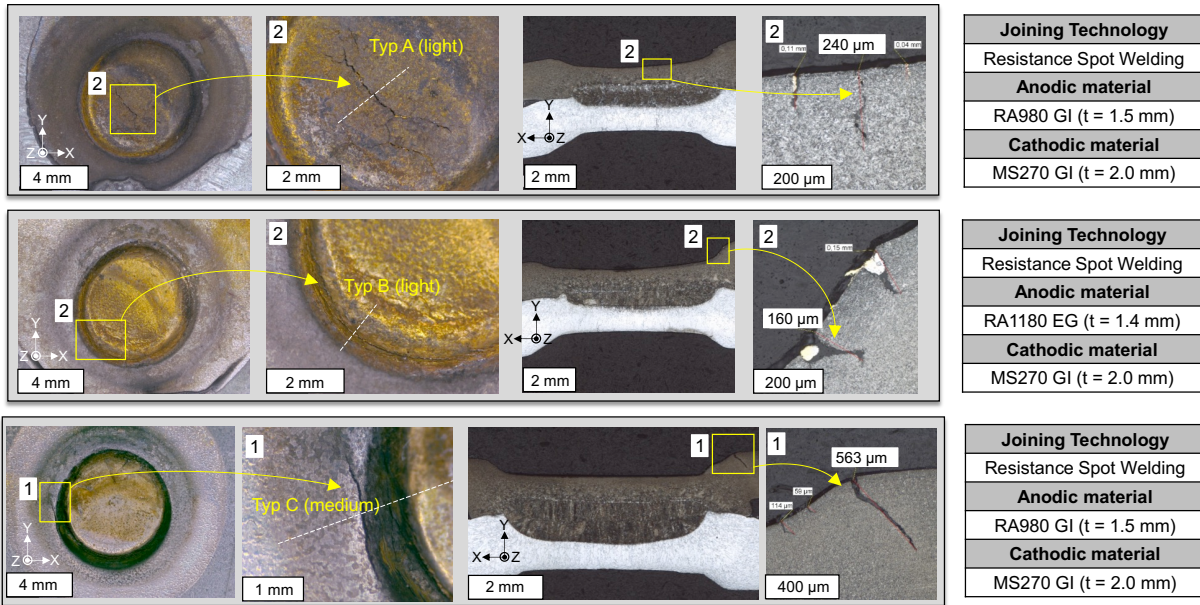
				Joining Technology
				Resistance Spot Welding
				Anodic material
				RA980 GI (t = 1.5 mm)
				Cathodic material
				MS270 GI (t = 2.0 mm)

Figure 6-65: Measurement of crack depth at similar crack severity in crash test samples (A, B, and C-type cracks from top to bottom)

It was found that at this level of crack severity, the depth was 37.5% of the total sheet thickness. This conclusion aligns with current technological understanding [7-14], which states that when the crack severity is light, with crack depths not exceeding 30% of the sheet thickness, the impact of LME cracks on the load-bearing capacity of the joint can be considered negligible.

7   Literature References

[1] J. Frei, M. Biegler, M. Rethmeier, C. Böhne, and G. Meschut, "Investigation of liquid metal embrittlement of dual phase steel joints by electro-thermomechanical spot-welding simulation," *Science and Technology of Welding and Joining*, vol. 24, no. 7, pp. 624–633, 2019, doi: 10.1080/13621718.2019.1582203.

[2] K. Prabitz *et al.,* "Validated Multi-Physical Finite Element Modelling of the Spot Welding Process of the Advanced High Strength Steel DP1200HD," *Materials (Basel, Switzerland)*, vol. 14, no. 18, 2021, doi: 10.3390/ma14185411.

[3] C. Böhne, G. Meschut, M. A. BIEGLER, and M. Rethmeier, "The Influence of Electrode Indentation Rate on LME Formation during RSW," *WJ*, vol. 101, no. 7, pp. 197–207, 2022, doi: 10.29391/2022.101.015.

[4] F. Okigami, N. Avedissian, H. Ghassemi-Armaki, X. Gao, and W. Zhang, "Numerical modeling of liquid metal embrittlement initiation during resistance spot welding of third generation advanced high strength steel – Effect of welding schedule and electrode alignment," *Journal of Manufacturing Processes*, vol. 110, pp. 173–191, 2024, doi: 10.1016/j.jmapro.2023.12.065.

[5] Testing and documentation guideline for the joinability of thin sheet of steel: Part 2: resistance spot welding., SEP1220-2, Düsseldorf.

[6] C. Böhne, G. Meschut, M. Biegler, and M. Rethmeier, "Avoidance of liquid metal embrittlement during resistance spot welding by heat input dependent hold time adaption," *Science and Technology of Welding and Joining*, vol. 25, no. 7, pp. 617–624, 2020, doi: 10.1080/13621718.2020.1795585.

[7] Brauser, S.; Rethmeier, M.; Noack, T.; Jüttner, S.: Einfluss von Oberflächenrissen auf die dynamische Festigkeit von Widerstandspunktschweißverbindungen aus hochfestem austenitischen Stahl. In Schweißen und Schneiden, 2013, 65.

[8] Benlatreche, Y.; Duchet, M.; Dupuy, T.; Cornette, D.; Carollo, G.: No effect of Liquid Metal Embrittlement cracks on the mechanical performances of spot welds. In 5th International Conference on Steels in Cars and Trucks, Amsterdam (NL), 18.-22. Juni, 2017.

[9] Dechalotte, F.; Auge, L.; Thillou, A.; Lens, A.; Dupuy, T.; Benlatreche, Y.; Aidan, D.: Experimental and numerical study of the influence of LME cracking on the behavior of spot welds. In Sheet Metal Welding Conference XVIII, Livonia (USA), 17.-18. Oktober, 2018.

[10] Choi, D.; Uhm, S.; Enloe, C.; Lee, H.; Kim, G.: Liquid Metal Embrittlement of Resistance Spot Welded 1180TRIP Steel - Effects of Crack Geometry on Weld Mechanical Performance, in Contributed Papers from Materials Science and Technology 2017 (MS&T17), Pittsburgh (USA), 2017.

[11] DiGiovanni, C.; Biro, E.; Zhou, N. Y.: Impact of liquid metal embrittlement cracks on resistance spot weld static strength. In Science and Technology of Welding and Joining, 2019, 24; S. 218-224

[12] DiGiovanni, C.; Biro, E.; Zhou, Y.: Effect of liquid metal embrittlement cracks on resistance spot weld fracture path. In Sheet Metal Welding Conference XVIII, Livonia (USA), 17.-18. Oktober, 2018.

[13] DiGiovanni, C.; Han, X.; Powell, A.; Biro, E.; Zhou, N. Y.: Experimental and Numerical Analysis of Liquid Metal Embrittlement Crack Location. In Journal of Materials Engineering and Performance, 2019, 28; S. 2045-2052.

[14] Lee, M.; Lee, D.; Choi, D.-Y.; Uhm, S.-H.: Effect of surface crack on the fatigue life for the resistance spot welding of galvanized trip180 steel sheets. In Sheet Metal Welding Conference XVIII, Livonia (USA), 17.-18. Oktober, 2018.

[15] Hahn, O.: Verfahren zur Herstellung von Proben und Probenspannvorrichtung; Patent DE 195 22 247 A1, 1995